# Studies on improvement of neutron lifetime measurement

富田, 龍彦



出版情報：Kyushu University, 2018, 博士（理学）, 課程博士
バージョン：
権利関係：

# Studies on improvement of neutron lifetime measurement

– 中性子寿命測定の高精度化に関する研究 –

九州大学大学院 理学府 物理学専攻
粒子物理学分野 素粒子実験研究室

富田 龍彦

指導教員 川越 清以

September 2, 2018

九州大学
KYUSHU UNIVERSITY

# Abstract

The neutron lifetime ($\tau_n$) is one of the most important parameters in Big-Bang Nucleosynthesis (BBN) and the Cabibbo–Kobayashi–Maskawa (CKM) matrix. Currently, $\tau_n = 880.2 \pm 1.0$ sec is determined with two major methods. One of them is called the proton counting method. In this method, $\tau_n$ is determined by the neutron flux and the number of protons from $\beta$ decay. Its precision is limited by uncertainty in the efficiency correction because these two values are determined in different detectors. The other method is the storage method using Ultra Cold Neutrons (UCNs). This method uses a material bottle to trap UCNs. $\tau_n$ can be calculated with the ratio of the introduced neutrons to surviving neutrons. However, the interaction between the neutrons and the wall of the bottle introduces considerable uncertainties. While these two methods can both determine $\tau_n$ (proton counting: $888.0 \pm 2.0$ sec, UCN storage: $878.6 \pm 0.6$ sec), there is a 3.9 $\sigma$ ($8.4 \pm 2.2$ sec) discrepancy. In order to verify this discrepancy, we are developing a third method at the Japan Proton Accelerator Research Complex (J-PARC). This method is based on the electron counting method which was originally established by Kossakowski et al. in 1989. In this method, we count electrons generated by neutron $\beta$ decay using a Time Projection Chamber (TPC) at 100 kPa. We can count not only electrons, but also the neutron flux simultaneously with the same detector. As a result, it is possible to eliminate the uncertainties that have been problematic with the existing two methods. The final goal of our experiment is 0.1% accuracy. From data acquired until 2016, we obtained a first physical result of $\tau_n = 896 \pm 10(\text{stat.}) \, ^{+14}_{-10}(\text{sys.})$ sec. Through this analysis, it was found that the background caused by neutron which is scattered by operating gasses is a considerable uncertainty factor.

In this thesis, we describe an attempt to reduce the background events caused by scattered neutrons by reducing the operating gas pressure. The purpose of this attempt is to suppress the scattered neutrons by reducing the the number of operating gas nuclei. We also aim to confirm the robustness of our experiment under low operating gas pressures. We tested our TPC with a pressure of lower than 50 kPa in 2016. From this test, it was found that the heat generation in the amplifier and decrease in detection efficiency due to the decrease in wire gain are important problems to solve. Therefore, we developed a low heat generation amplifier by using an Application Specific Integrated Circuit (ASIC) and its read out system, and we evaluated the basic characteristics of this amplifier. As a result of this evaluation, we confirmed that the new amplifier can reduce the heat generation by a factor of 50 compared to the amplifier that we currently use. Through this development, we expect feasible low gas pressure operation from the viewpoint of hardware requirements. Therefore, in November 2017, we carried out a physics run with a gas pressure of 50 kPa. Data collection was carried out over a week, and we obtained data with 1.8% statistical accuracy. For the analysis of this data, we constructed a Monte Carlo simulation at 50 kPa, optimized the method of event selection, and estimated the various uncertainties. Finally, we obtained the result of $\tau_n = 917 \pm 16(\text{stat.}) \pm 19(\text{sys.})$ sec. This result is consistent with the measurement at 100 kPa within the uncertainties.

From the results of this study, we can solve the issue of heat generation by using the newly developed amplifier. Thus, we can carry out the experiment with much lower gas pressures to reduce the number of background events caused by scattered neutrons. We also obtained a result that is consistent with 100 kPa even at 50 kPa. This shows that our experimental apparatus and analysis method are robust to changes in the gas pressure, and we can expect to improve our experimental accuracy with the lower gas pressures operation in the future.

# Contents


**1 Introduction** **11**
- 1.1 Overview of this thesis . . . 11
- 1.2 Neutron . . . 12
- 1.3 Physics of neutron lifetime . . . 13
  - 1.3.1 Big-Bang Nucleosynthesis . . . 13
  - 1.3.2 Cabibbo–Kobayashi–Maskawa matrix . . . 14
- 1.4 History of neutron lifetime measurement . . . 15
  - 1.4.1 Proton counting method . . . 17
  - 1.4.2 UCN storage method . . . 18
  - 1.4.3 Electron counting method . . . 21

**2 Neutron lifetime measurement at J-PARC** **23**
- 2.1 Experimental principle . . . 23
- 2.2 Determination of $^3$He density . . . 23
- 2.3 Facility and beamline . . . 24
  - 2.3.1 Japan Proton Accelerator Research Complex . . . 24
  - 2.3.2 Materials and Life science experimental Facility . . . 26
  - 2.3.3 BL05 (NOP) . . . 29
- 2.4 Experimental apparatus . . . 30
  - 2.4.1 Setup . . . 30
  - 2.4.2 Spin Flip Chopper . . . 31
  - 2.4.3 Beam monitor . . . 32
  - 2.4.4 $^6$LiF shutter . . . 32
  - 2.4.5 Time Projection Chamber . . . 34
  - 2.4.6 Calibration system . . . 36
  - 2.4.7 Cosmic veto system . . . 36
- 2.5 Data acquisition system . . . 37
- 2.6 Simulation . . . 38
  - 2.6.1 Simulation of particle interaction . . . 38
  - 2.6.2 Simulation of the detector response . . . 40
- 2.7 Result of 100 kPa operations . . . 40

**3 Studies for low gas pressure operation** **43**
- 3.1 Motivation for low pressure operation . . . 43
- 3.2 Test operation at J-PARC . . . 44
  - 3.2.1 Setup . . . 44

3.2.2 Gain evaluation . . . 45
3.2.3 Heat generation . . . 48
3.2.4 Summary of test operation . . . 49
3.3 Development of new amplifier . . . 49
3.3.1 GTARN amplifier . . . 49
3.3.2 Additional amplifier . . . 51
3.3.3 Read out system for new amplifier . . . 51
3.4 Evaluation of newly developed amplifier . . . 53
3.4.1 Power consumption . . . 53
3.4.2 Gain linearity . . . 53
3.4.3 Summary of new amplifier . . . 55

**4 Neutron lifetime measurement at** 50 kPa **57**
4.1 Collected data . . . 57
4.2 Scattered neutrons at low gas pressure . . . 58
4.3 Estimation of the number of signal candidates . . . 59
4.3.1 Background study for Category A . . . 60
4.3.2 Background study for Category B . . . 65
4.3.3 Background study for Category C . . . 71
4.3.4 Signal estimation . . . 72
4.4 Efficiency . . . 75
4.4.1 Efficiency for neutron $\beta$ decay . . . 75
4.4.2 Efficiency for the neutron absorption by $^3$He . . . 75
4.5 Determination of the number density of $^3$He . . . 75
4.6 Uncertainty . . . 76
4.6.1 Statistical uncertainty . . . 76
4.6.2 Systematic uncertainty . . . 77
4.7 Calculation of neutron lifetime . . . 83

**5 Conclusion and future prospects 85**

**A Developed amplifier 87**
A.1 Circuit of GTARN amplifier . . . 87
A.2 Circuit of additional amplifier . . . 90
A.3 Circuit of read out module . . . 92

# List of Figures


1.1 Feynman diagram of neutron beta decay. . . . 12
1.2 Relationship among neutron wavelength, velocity, and energy. . . . 13
1.3 Relationship among CKM unitarity, $V_{ud}$ and $\lambda$. . . . 15
1.4 History of neutron lifetime measurements. . . . 16
1.5 Neutron lifetime measured by the proton counting method and UCN storage method. . . . 16
1.6 Schematic view of the proton counting method at the NIST. . . . 17
1.7 Schematic view of the experimental apparatus at the ILL in 2005. . . . 19
1.8 Schematic view of the experiment at Los Alamos. . . . 20
1.9 Arrangement of the Halbach array. . . . 20
1.10 Schematic view of Kossakowski's experiment. . . . 21

2.1 Conceptual diagram of the gas introduction. . . . 24
2.2 Aerial photograph of J-PARC. . . . 25
2.3 Schematic top-view of the MLF . . . . 27
2.4 Neutron source at the MLF . . . . 28
2.5 Schematic view of BL05 . . . . 29
2.6 Setup for neutron lifetime measurement at J-PARC. . . . 30
2.7 Schematic top-view (top) and the photograph (bottom) of the SFC . . . . 31
2.8 Time structure of the MLF beam and bunch structure of BL05. . . . 32
2.9 Picture of the beam monitor. . . . 33
2.10 Picture of the $^6$LiF shutter. . . . 33
2.11 Photograph of the TPC . . . . 34
2.12 Inside photograph of the TPC. . . . 35
2.13 Alignment of each wire of the MWPC. . . . 36
2.14 Block diagram of the data acquisition system. . . . 37
2.15 Snapshot of the simulated apparatus in the simulation. . . . 39
2.16 Summary of neutron lifetimes for all three methods. . . . 40

3.1 Illustration of a background event caused by a scattered neutron. . . . 44
3.2 Gain at 100 kPa. . . . 46
3.3 Gain at 25 kPa. . . . 47
3.4 Temperature during low gas pressure operation. . . . 48
3.5 Simplified block diagram of the GTARN amplifier. . . . 50
3.6 Photograph of the GTARN amplifier. . . . 50
3.7 Photograph of the additional amplifier. . . . 51
3.8 Photograph of the module for the developed amplifier. . . . 52

3.9 Schematic diagram of the measurement for gain evaluation. . . . . 53
3.10 Gain linearity of the GTARN amplifier. . . . . 54

4.1 Distribution of the FCE. . . . . 59
4.2 Schematic view of "beam on" and "beam off" setups. . . . . 61
4.3 Distribution of the TOF. . . . . 62
4.4 Conceptual view for determining the fiducial region. . . . . 63
4.5 Two-dimensional distribution of the TOF and cathode hit information. . . . . 64
4.6 TOF distribution with superimposed the fiducial and sideband regions. . . . . 65
4.7 Example of drift lengths of the cosmic ray background and a $\beta$ decay signal. . . 66
4.8 Distribution of the drift length. . . . . 67
4.9 Conceptual picture of the DC. . . . . 68
4.10 Distribution of the DC. . . . . 69
4.11 Distribution of the deposit energy in the TPC. . . . . 70
4.12 Conceptual picture of the $x$-value. . . . . 71
4.13 Distribution of $x$-values. . . . . 72
4.14 Distribution of the deposit energy onto the field wire. . . . . 74
4.15 Photograph of the mass spectrometer. . . . . 76
4.16 Distribution of the deposit energy in the low voltage operation. . . . . 80
4.17 Summary of neutron lifetimes from all three methods. . . . . 84

A.1 Circuit of GTARN amplifier. . . . . 88
A.2 Board layout with three GTARN amplifiers. . . . . 89
A.3 Board layout of additional amplifier. . . . . 90
A.4 Circuit of additional amplifier. . . . . 91
A.5 Board layout of read out module. . . . . 92
A.6 Circuit of read out module. . . . . 93

# List of Tables


1.1 Basic properties of the neutron. . . . 12

2.1 Basic specifications of J-PARC. . . . 25
2.2 Specifications of BL05 . . . . 29
2.3 Specifications of the TPC . . . . 35
2.4 List of Monte Carlo samples. . . . 38

3.1 Scattering and absorption cross sections of various nuclei for 2200 m/s neutrons. 43
3.2 Voltage applied to the anode wire for each gas pressure. . . . 45
3.3 Specifications of the newly developed amplifier. . . . 55

4.1 Data acquisition sequence. . . . 57
4.2 DAQ cycle in low voltage operation. . . . 58
4.3 Number of background events estimated by Monte Carlo simulations. . . . 73
4.4 Numbers of signal candidates. . . . 73
4.5 Efficiencies for neutron $\beta$ decay for each cut. . . . 75
4.6 Efficiencies for neutron absorption by $^3$He. . . . 75
4.7 Contamination of $^{14}$N and $^{17}$O. . . . 79
4.8 Uncertainties in the cut efficiencies for neutron $\beta$ decay candidates. . . . 80
4.9 Uncertainty in the cut efficiency for neutron absorption by $^3$He candidates. . . . 81
4.10 Summary of uncertainties. . . . 81
4.11 Corrections and uncertainties for each analysis procedure for $\beta$ decay events. . . . 82
4.12 Corrections and uncertainties for each analysis procedure for $^3$He events. . . . 82
4.13 Summary of the analysis. . . . 83

# Chapter 1

# Introduction

## 1.1 Overview of this thesis

This thesis describes studies for improving neutron lifetime measurements at the Japan Proton Accelerator Research Complex (J-PARC). The neutron lifetime is an important input parameter in the Standard Model of particle physics; however, there is a large discrepancy between the two major measurement methods. A new type of the neutron lifetime measurement has been performed at J-PARC since 2009, and the first physical results were released in 2017. In the analysis for the first result, a background was identified that hindered experimental accuracy. In this thesis, a number of studies, the test for low gas pressure operation of the Time Projection Chamber (TPC), the development of a number of modules and their evaluation, and the data analysis for low gas pressure operation of the TPC to overcome the background are described. This thesis is organized as follows. In Chapter 1, an introduction to the neutron and the history of neutron lifetime measurement are described. The roles of the neutron lifetime in two theories are also described. Methods of neutron lifetime measurement are summarized and reviewed by comparing them with our method. Chapter 2 is an explanation of our experimental apparatus. Since there are some unique devices to improve the measurement accuracy, their characteristics and advantages are described here. In the first part of Chapter 3, the results from test operations at low gas pressures and issues to be solved are described. The rest of Chapter 3 explains developments to solve these issues. The results from the evaluation of the developed devices are also described here. In Chapter 4, neutron lifetime measurement at low gas pressures is described from the points of view of data acquisition and analysis. Finally, the thesis is concluded in Chapter 5.

## 1.2 Neutron

The existence of the neutron was predicted by Rutherford in 1920 [1]. After this prediction, Bothe and Becker discovered the unknown radiation by irradiating beryllium with alpha rays from polonium [2]. This radiation has high penetrating power and was called a "beryllium ray". Curie carried out a similar experiment to identify this radiation, and she hypothesized that the beryllium ray was a high energy gamma ray [3]. Soon after this report, Chadwick carried out an experiment with the same way as Curie did; however he irradiated various kinds of targets with beryllium rays. Eventually, Chadwick discovered the neutron through this experiment in 1932 [4]. The basic properties of neutrons are shown in Table 1.1.

| | |
|---|---|
| Mass | 939.57 MeV/$c^2$ |
| Spin | 1/2 |
| Charge | $(-0.2 \pm 0.8) \times 10^{-21}$e |
| Mean lifetime | $880.2 \pm 1.0$ sec |

Table 1.1: Basic properties of the neutron [5].

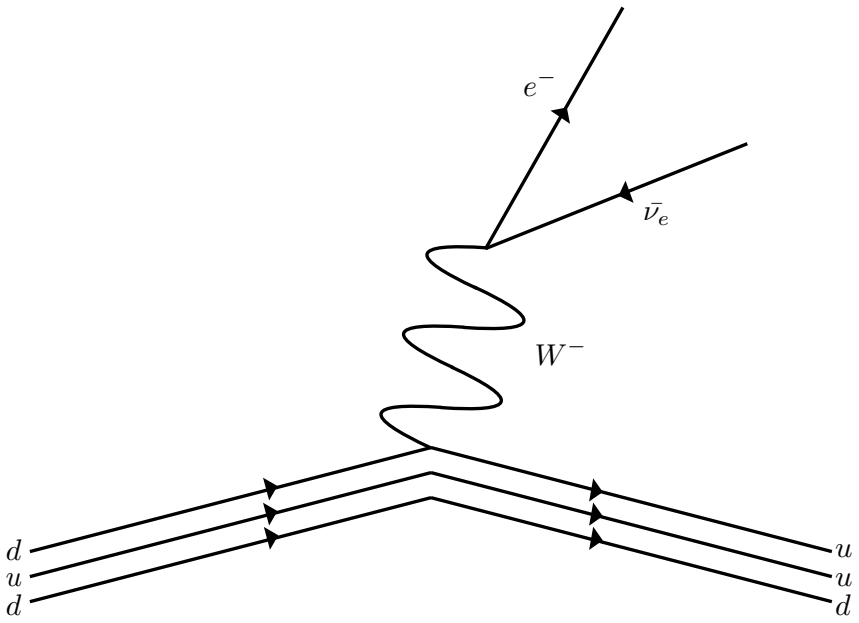


Figure 1.1: Feynman diagram of neutron beta decay.

Neutrons in nucleons are stable except for neutron-rich nuclei; however, free neutrons decay into protons, electrons and electron antineutrinos through the weak interaction [6]. This is called "$\beta$ decay" and the Feynman diagram of this process is shown in Figure 1.1. The neutron's mean lifetime is $880.2 \pm 1.0$ sec, from the summary in Particle Data Group's 2017 Review [5]. Neutrons can be categorized into fast neutrons, thermal neutrons, cold neutrons and ultra cold neutrons (UCNs) according to their energy. Cold neutrons and UCNs are especially used for various physics experiments because they are easy to handle. A summary of wavelengths, velocities and energies of the neutron is shown in Figure 1.2.

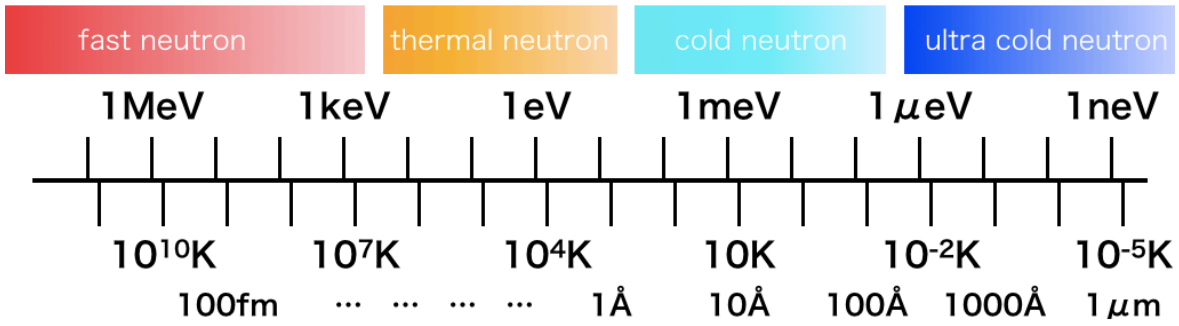


Figure 1.2: Relationship among neutron wavelength, velocity, and energy.

## 1.3 Physics of neutron lifetime

As mentioned in Section 1.2, a neutron decays into a proton, an electron, and an electron antineutrino with a mean lifetime of $880.2 \pm 1.0$ sec through the weak interaction. Since this process is a simple semi-leptonic decay not involving nuclear interactions, it is important for the verification of the Standard Model of particle physics (hereafter SM) [7]. The neutron lifetime is also used to calculate some physical parameters. In the following subsections, we will discuss Big-Bang Nucleosynthesis (BBN) and the Cabibbo–Kobayashi–Maskawa (CKM) matrix, in which the neutron lifetime plays important roles.

### 1.3.1 Big-Bang Nucleosynthesis

BBN explains the synthesis of light elements such as hydrogen, deuterium, tritium, helium, lithium, and beryllium in the early universe [8]. It is thought that the universe immediately after the Big-Bang was in a high density and high temperature state; therefore, the quarks and gluons existed in the plasma state. At $10^{-4}$ sec after the Big-Bang, the temperature dropped, and protons and neutrons formed from the quarks and gluons. At this stage, the protons and neutrons are maintained in equilibrium through the process

$$n + e^+ \leftrightarrow p + \bar{\nu}_e \tag{1.1}$$

$$p + e^- \leftrightarrow n + \nu_e \ . \tag{1.2}$$

Here, the ratio of the number of neutron to that of proton ($n/p$) can be written as

$$n/p = \exp(-\Delta m/T), \tag{1.3}$$

where $\Delta m$ represents the mass difference between the neutron and the proton, $\Delta m \sim 1.293\,\mathrm{MeV}/c^2$, and $T$ is the temperature of the universe. At 1 sec after the Big-Bang, the temperature of the universe dropped to 1 MeV or less; the equilibrium state therefore collapsed, and the neutrons can decay into protons by $\beta$ decay. Thereafter, about 200 sec passed from the Big-Bang, the ratio of neutron to proton decreased to about $n/p \sim 1/7$. Since the proportion of light elements to be synthesized depends on the number of neutrons, the neutron lifetime is an important parameter in BBN.

### 1.3.2 Cabibbo–Kobayashi–Maskawa matrix

The CKM matrix is a $3 \times 3$ unitary matrix, and it explains the mixing of quarks in the SM [9]. The CKM matrix is expressed as

$$\begin{aligned} V_{\mathrm{CKM}} &= \begin{pmatrix} V_{ud} & V_{us} & V_{ub} \\ V_{cd} & V_{cs} & V_{cb} \\ V_{tb} & V_{ts} & V_{tb} \end{pmatrix} \\ &= \begin{pmatrix} 0.97434^{+0.00011}_{-0.00012} & 0.22506 \pm 0.00050 & 0.00357 \pm 0.00015 \\ 0.22492 \pm 0.00050 & 0.97351 \pm 0.00013 & 0.0411 \pm 0.0013 \\ 0.00875^{+0.00032}_{-0.00033} & 0.0403 \pm 0.0013 & 0.99915 \pm 0.00005 \end{pmatrix}. \end{aligned} \tag{1.4}$$

The unitarity of the CKM matrix can be tested using these CKM elements. For the first row and first column of this matrix, the obtained experimental results for the unitarity conditions are as follows:

$$\mid V_{ud} \mid^2 + \mid V_{us} \mid^2 + \mid V_{ub} \mid^2 = 0.9996 \pm 0.0005 \tag{1.5}$$

$$\mid V_{ud} \mid^2 + \mid V_{cd} \mid^2 + \mid V_{td} \mid^2 = 0.9975 \pm 0.0022. \tag{1.6}$$

If this unitarity is broken, it implies the existence of another generation of quarks. Since the $V_{ud}$ term is the largest parameter among these CKM elements, it is important to determine $V_{ud}$ with a high accuracy to test CKM unitarity. Currently, $V_{ud}$ is determined by the study of superallowed nuclear $\beta$ decays with less than 0.1% accuracy. However, there is a large model-dependence of measurement by superallowed nuclear $\beta$ decay; it is thus valuable to determine $V_{ud}$ using other methods. Neutron lifetime is one of a good probe to test $V_{ud}$. We can calculate $V_{ud}$ with the neutron lifetime $\tau_n$ and $\lambda$, which is the ratio of the axial-vector coupling to vector coupling, as follows:

$$\mid V_{ud} \mid^2 = \frac{4908.7 \pm 1.9}{\tau_n(1 + 3\lambda^2)}. \tag{1.7}$$

Since neutron $\beta$ decay does not contain nuclear interactions, we can test the CKM unitarity in a model-independent way. The relationship among CKM unitarity, $V_{ud}$, and $\lambda$ is shown in Figure 1.3.

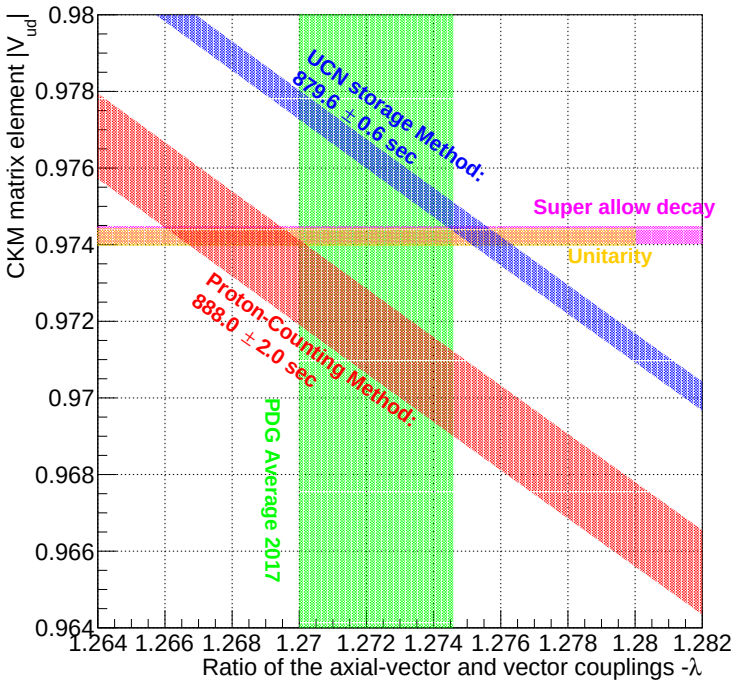


Figure 1.3: Relationship among CKM unitarity, $V_{ud}$ and $\lambda$.

In Figure 1.3, the yellow band satisfies the unitarity condition, and the green band shows the experimental results of $\lambda$ [5]. The purple band shows the results from superallowed nuclear $\beta$ decay. Results from neutron lifetime measurements are shown with the red and blue bands, and we will discuss this in the following section.

## 1.4 History of neutron lifetime measurement

After the discovery of the neutron, a number of experiments have been carried out to determine the neutron lifetime. The history of neutron lifetime measurement since its discovery is shown in Figure 1.4.

As shown in Figure 1.4, the neutron lifetime has changed by over 100 sec in this 50 years. Recently, there have been two major methods that determined neutron lifetime with a high accuracy. One of them is called the "proton counting" method, and the other one is the "UCN storage" method. The results of these two methods are shown in Figure 1.5. Both methods determined the neutron lifetime with high accuracy; in particular, the UCN storage method has a 0.1% accuracy. However, there is an 8.4 sec discrepancy between these two results. This discrepancy affects physics parameters calculated using neutron lifetime, as shown in Figure 1.3. In the following subsections, these two methods will be explained in more detail.

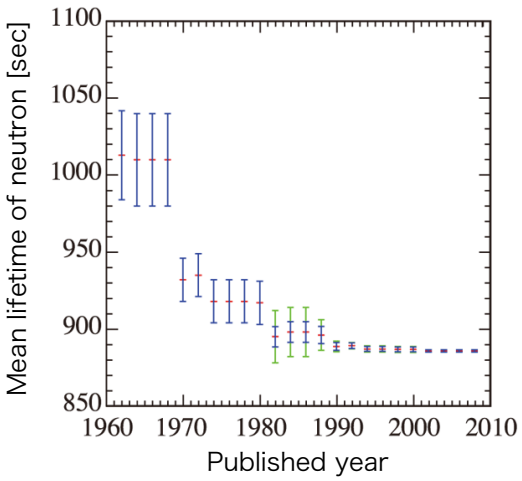


Figure 1.4: History of neutron lifetime measurements. The central value of the neutron lifetime has changed significantly over the past 50 years.

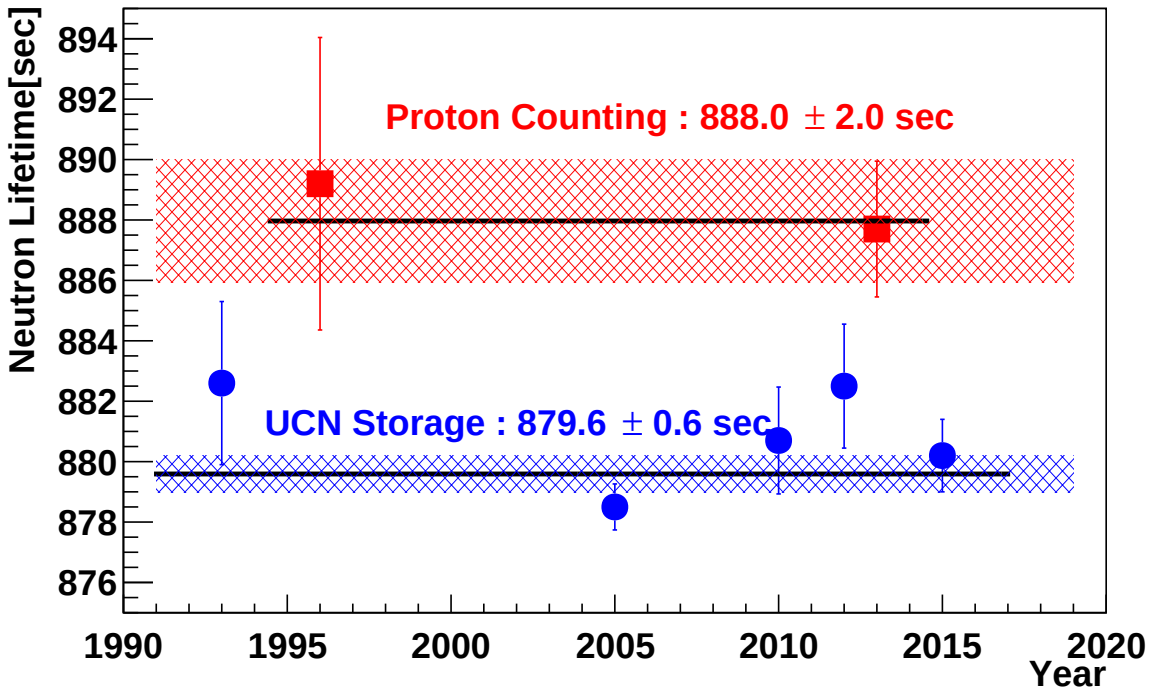


Figure 1.5: Neutron lifetime measured by the proton counting method and UCN storage method. Proton counting method is shown with squares and UCN storage method is shown with circles [10-16].

### 1.4.1 Proton counting method

The first results using the proton counting method were obtained by Christensen et al. in 1972 [17]. In this method, neutrons generated by a nuclear reactor are used. These neutrons decay into protons, electrons and electron antineutrinos, and these protons will be trapped with electric and magnetic fields. After a certain amount of time, the protons are extracted from the trap region and counted using a silicon detector. The neutron flux is determined using another detector, and the neutron lifetime is determined by the numbers of protons and neutrons. At present, the most accurate experiment using the proton counting method is an experiment carried out at the National Institute of Standards and Technology (NIST) in 2000 [18, 19]. A schematic view of this experiment is shown in Figure 1.6. The upper figure in Figure 1.6 shows the state when the protons are trapped and the bottom figure shows the state when the protons are extracted. The neutron flux is counted by counting alpha and trittium emissions by the $^6\mathrm{Li}(n,t)\alpha$ reaction. The extracted protons are counted by a silicon-based proton detector.

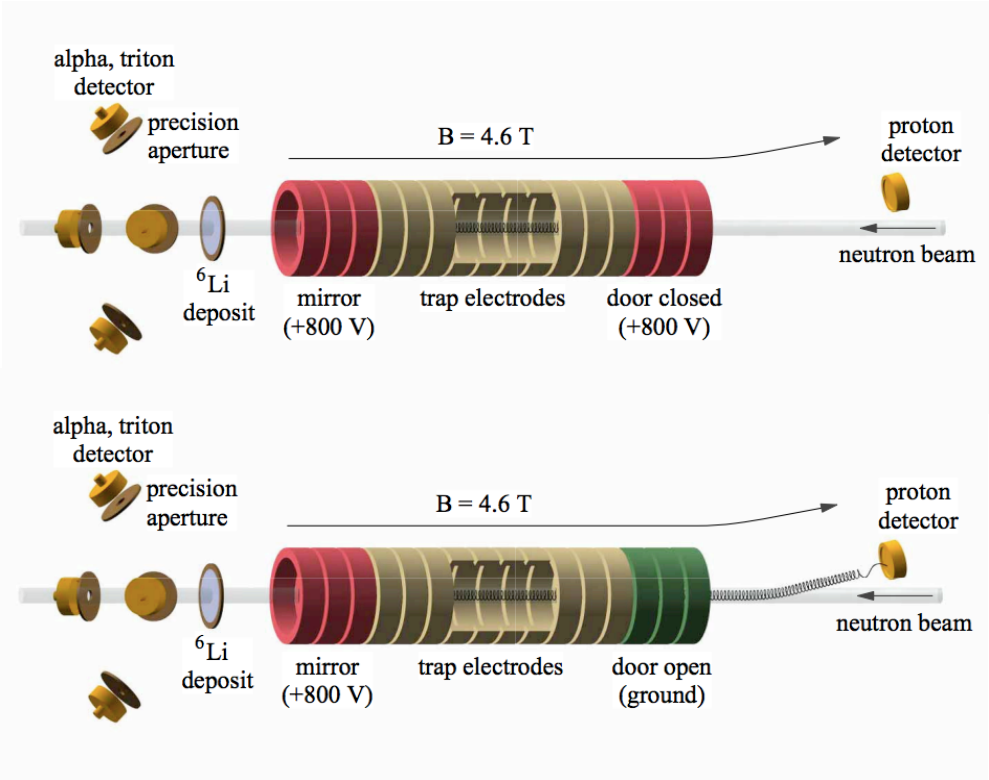


Figure 1.6: Schematic view of the proton counting method at the NIST. Protons from neutron $\beta$ decay are trapped in the central trap electrodes with an electric and magnetic fields. The neutron flux is counted by counting alpha and tritium emissions by the $^6\mathrm{Li}(n,t)\alpha$ reaction. Trapped protons are extracted by eliminating the electric field at a certain side, and counted with a silicon-based proton detector. The upper figure shows the state when the protons are trapped and the bottom figure shows the state when the protons are extracted.

In the NIST experiment, a neutron generated by the nuclear reactor is decelerated to the energy region of cold neutrons. This neutron is introduced in the region where both an electric field formed using multiple electrodes and a magnetic field formed in parallel with the beam

axis are applied. The protons emitted from neutron $\beta$ decay in the trap region are held by these electric and magnetic fields. In this method, the neutron lifetime can be calculated as the ratio of the counted numbers of protons and neutrons. The count rate of the neutron flux ($S_n$) and the protons from neutron $\beta$ decay ($S_p$) are given by

$$S_n = \epsilon_n N \rho \sigma L_n \tag{1.8}$$
$$S_p = \epsilon_p N L_p / \tau_n v, \tag{1.9}$$

where $\epsilon_n$ and $\epsilon_p$ are the detection efficiency for neutrons and protons, respectively, $N$ is the total number of introduced neutrons, $\rho$ is the density of the $^6$Li deposit, $\sigma$ is the neutron absorption cross section of $^6$Li, $L_n$ and $L_p$ are the depths of the neutron and proton detectors, respectively, $\tau_n$ is the neutron lifetime, and $v$ is the velocity of the neutron. From equations 1.8 and 1.9, the neutron lifetime $\tau_n$ can be expressed as

$$\tau_n = \frac{1}{\rho \sigma v} \left( \frac{S_n/\epsilon_n}{S_p/\epsilon_p} \right) \frac{L_p}{L_n}. \tag{1.10}$$

The NIST experiment determined the neutron lifetime with the following formula:

$$\tau_n = 887.7 \pm 1.2 \text{ (stat.)} \pm 1.9 \text{ (sys.)}. \tag{1.11}$$

In their final result, the dominant systematic uncertainty is due to the use of different detectors for the neutrons and protons.

### 1.4.2 UCN storage method

#### UCN storage using material bottle

Since the kinetic energy of a UCN is only 100 neV, it can be totally reflected by the Fermi potential of a nucleus, which is typically a few hundred neV. According to this feature, UCNs can be stored in a material bottle. In this UCN storage method, the number of stored neutrons and the number of neutrons after a certain amount of time are counted. The most precise measurement was done by Serebrov et al., at the Institut Laue–Langevin (ILL) in 2005 [20]. A schematic view of this experiment is shown in Figure 1.7.

This method has no uncertainty on the detection efficiency that arises in the proton counting method. However, since the interaction between neutron and the material wall strongly depends on the density uniformity and the temperature of the wall, there is a considerable systematic uncertainty in the wall loss effect.

In the experiment at the ILL, a neutron generated by the nuclear reactor and decelerated to the energy region of UCNs is used. This neutron will be stored in the trap bottle (8 in Figure 1.7), and stored for a certain period $t_1$ or $t_2$. After $t_1$ or $t_2$ has passed, surviving neutrons are extracted and counted. Expressing the number of counted neutrons as $S_1$ or $S_2$, and defining the time difference $\delta t$ as $\delta t = t_2 - t_1$, the neutron lifetime can be calculated:

$$\frac{\ln(S_1/S_2)}{\delta t} = \frac{1}{\tau_n} + \frac{1}{\tau_{\text{loss}}} \tag{1.12}$$

where $\tau_{\text{loss}}$ is the effect of wall loss. As a result of this experiment, they obtained

$$\tau_n = 878.5 \pm 0.7 \text{ (stat.)} \pm 0.3 \text{ (sys.)}. \tag{1.13}$$

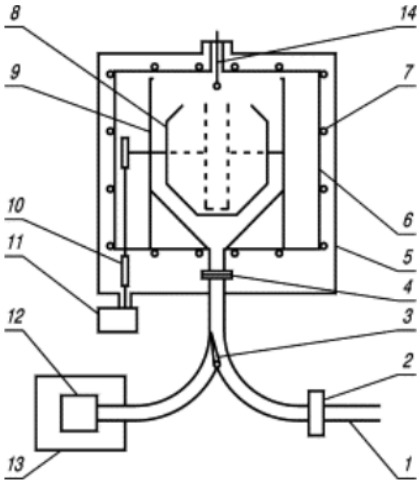


Figure 1.7: Schematic view of the experimental apparatus at the ILL in 2005. 1: neutron guide for UCNs, 2 : UCN inlet valve, 3 : neutron selector valve, 4 : connecting unit, 5 : vacuum chamber, 6 : separate vacuum volume of the cryostat, 7 : cooling coils for the thermal shields, 8 : UCN storage trap with the dashed lines depicting a narrow cylindrical trap, 9 : cryostat, 10 : trap rotation mechanics, 11 : stepping motor, 12 : UCN detector, 13 : detector shielding, and 14 : evaporator.

### UCN storage using magnetic field

As mentioned in Section 1.4.2, the uncertainty due to the wall loss effect is a considerable uncertainty in the UCN storage method. In 2017, a Los Alamos group reported an approach that can potentially remove the wall loss effect issue [21]. In this method, they used a magnetic field to store the UCN. A schematic view of the experiment is shown in Figure 1.8. In this experiment, they used a Halbach array to generate a magnetic field. The Halbach array has a unique arrangement: it makes a strong magnetic field only on one side and nearly zero magnetic field on the other side. The arrangement of the Halbach array is shown in Figure 1.9. In the case of Figure 1.9, there is a strong magnetic field on the bottom side through the superposition of each magnet, and there is a weak magnetic field on the top side by cancellation of each magnet.

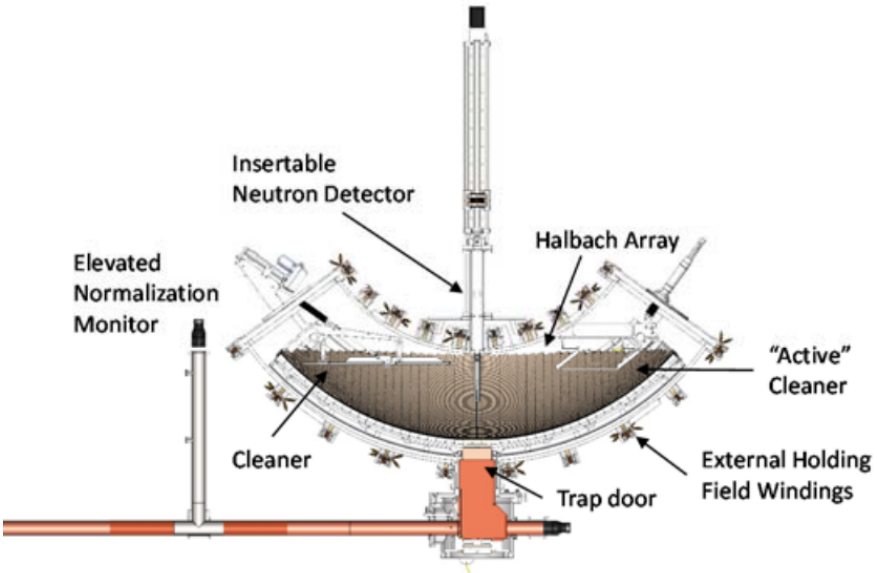


Figure 1.8: Schematic view of the experiment at Los Alamos. The UCNs are guided to the magnetic field formed by the Halbach array and stored. The insertable neutron detector and cleaner are made by with a ZnS:Ag scintillator and $^{10}$B. The active cleaner and insertable neutron detector can move down to the bottom of the storage bottle, and they can therefore select the neutron energy.

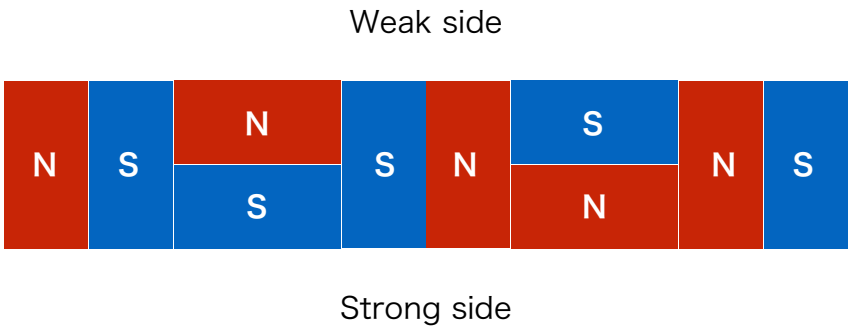


Figure 1.9: Arrangement of the Halbach array. The top side of this figure has nearly zero magnetic field with cancellation of each magnet.

The neutrons of the Los Alamos experiment are also generated by a nuclear reactor, and decelerated to the energy region of UCNs. The UCNs are guided to the storage region through the trap door in Figure 1.8, where the magnetic field was applied, and the neutrons that have large energies are absorbed by the cleaner. After a certain storage time, the insertable neutron detector is inserted, and the number of surviving neutrons are counted. During storage, neutron does not interact directly with the wall of the storage bottle, hence the effect of the wall loss can be ignored. As a result of this experiment, they obtained

$$\tau_n = 877.7 \pm 0.7 \text{ (stat.)} \, {}^{+0.4}_{-0.2} \text{ (sys.)}. \tag{1.14}$$

### 1.4.3 Electron counting method

Yet another approach to remove possible systematic uncertainties is called the electron counting method. This method was first reported by Kossakowski et al. in 1989 [22], and is a method to determine the neutron lifetime by counting the electrons from neutron $\beta$ decay. A schematic view of this experiment is shown in Figure 1.10.

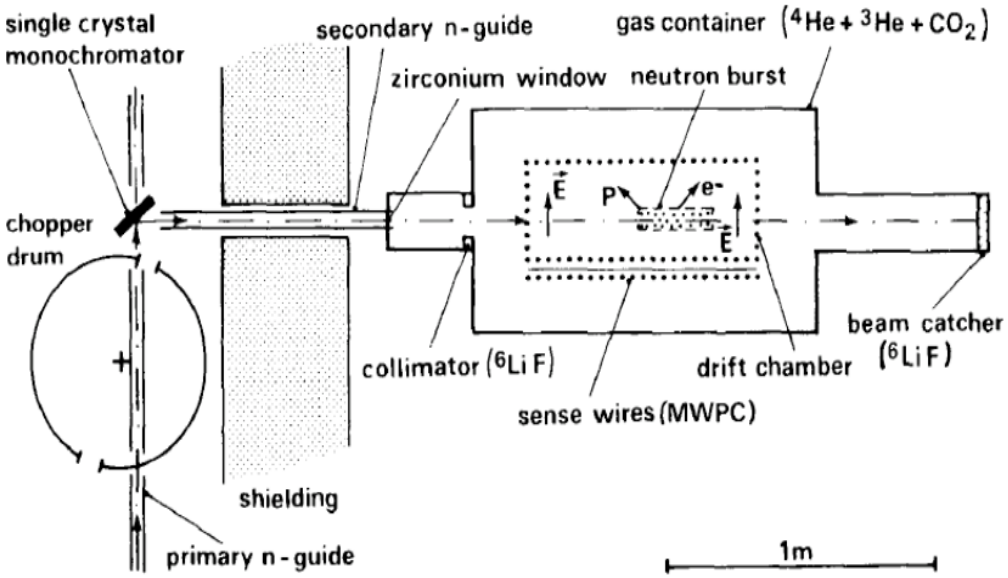


Figure 1.10: Schematic view of Kossakowski's experiment. The neutrons generated by a nuclear reactor are transported to the TPC after passing through the rotating chopper drum and single crystal monochromator to form a continuous neutron beam into the monochromatic short bunches.

In this experiment, the electrons from neutron $\beta$ decay are detected in the TPC, and neutron flux is also measured using the reaction of $^3\text{He}(n,p)t$ in the TPC. Neutrons do not interact naturally with the TPC wall, and there is also no uncertainty due to the use of different

detectors because neutron flux and decay products are measured by the same detector. In their method, the existing uncertainties in the proton counting method and UCN storage method are hence removed. In Kossakowski's experiment, the monochromator and rotation chopper greatly reduced the number of neutrons, so their final result was statistically limitted as follows

$$\tau_n = 878 \pm 27 \text{ (stat.)} \pm 14 \text{ (sys.)}. \tag{1.15}$$

Our measurement described in this thesis is an improved version of this electron counting method.

# Chapter 2

# Neutron lifetime measurement at J-PARC

## 2.1 Experimental principle

Our final goal is to measure the neutron lifetime $\tau_n$ with 0.1% accuracy. In this section, the principle of this experiment and how to realize the measurement are described. In our experiment, neutron lifetime is calculated with the number of neutrons that pass through the TPC and the number of electrons that come from neutron $\beta$ decay. In our method, the numbers of neutrons and electrons are counted in the TPC simultaneously. We introduced a tiny amount of $^3$He gas to count the numbers of neutrons using the $^3\mathrm{He}(n,p)t$ reaction. The detection efficiency for the numbers of both neutrons and electrons is determined by using a Monte Carlo simulation based on Geant4 [24]. By denoting the numbers of neutrons and electrons as $N_{^3\mathrm{He}}$ and $N_\beta$, respectively, the neutron lifetime $\tau_n$ can be expressed as

$$\tau_n = \frac{1}{\rho\sigma_0 v_0}\frac{N_{^3\mathrm{He}}/\epsilon_{^3\mathrm{He}}}{N_\beta/\epsilon_\beta}, \tag{2.1}$$

where $\epsilon_{^3\mathrm{He}}$ and $\epsilon_\beta$ are the detection efficiencies of the $^3\mathrm{He}(n,p)t$ reaction and neutron $\beta$ decay, respectively. The $\rho$ represents the number density of the $^3$He gas in the TPC. The cross section of neutron absorption with $^3$He is inversely proportional to the neutron velocity, thus we can treat the product of the cross section and the neutron velocity as a constant. We employed the values of $\sigma_0 = 5333 \pm 7$ barn [23] and $v_0 = 2200$ m/s in this experiment.

## 2.2 Determination of $^3$He density

As mentioned in the previous section, we introduced about 1 ppm of $^3$He into the TPC to measure the neutron flux. The number density of the introduced $^3$He is determined from the ratio of the gas handling volume ($V_1$) and the volume of the TPC ($V_2$). Figure 2.1 shows a conceptual diagram of the gas introduction. Using the initial pressure $P_1$ in $V_1$ at temperature $T_1$, we obtain the following relation on the basis of the ideal gas law,

$$P_1 V_1 = n_{gas} R T_1 \tag{2.2}$$

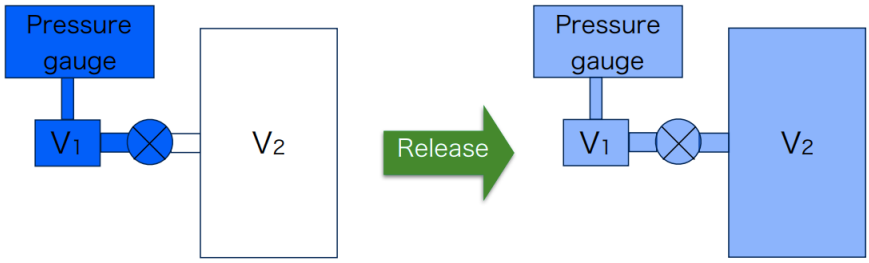


Figure 2.1: Conceptual diagram of the gas introduction. $V_1$ is the gas handling volume and $V_2$ is the volume of the TPC.

where $n_{gas}$ is the amount of $^3$He and $R$ is the gas constant. After releasing the filled gas in $V_1$ to $V_2$, the equation is re-written using $P_2$, $V_2$ and $T_2$,

$$P_2(V_1 + V_2) = n_{gas} R T_2. \tag{2.3}$$

Thus, the number density of $^3$He, $\rho$, can be calculated with Equations (2.2) and (2.3) as

$$\begin{aligned} \frac{P_1 V_1}{R T_1} &= \frac{P_2(V_1 + V_2)}{R T_2}, \quad \frac{n_{gas}}{V_1 + V_2} = \frac{P_2}{R T_2} = \rho \\ \rho &= \frac{P_1}{R T_1} \frac{V_1}{V_1 + V_2}. \end{aligned} \tag{2.4}$$

The temperatures $T_1$ and $T_2$ are measured simultaneously during the gas introduction. The volume ratio is measured before gas introduction. Using this method, we can extract the number density of $^3$He with around 0.5% precision.

## 2.3 Facility and beamline

In this section, the experimental facility and beamline will be explained.

### 2.3.1 Japan Proton Accelerator Research Complex

The Japan Proton Accelerator Research Complex (J-PARC) is located in Tokai Village, Ibaraki Prefecture, Japan [25]. J-PARC can provide the highest intensity proton beam in the world.

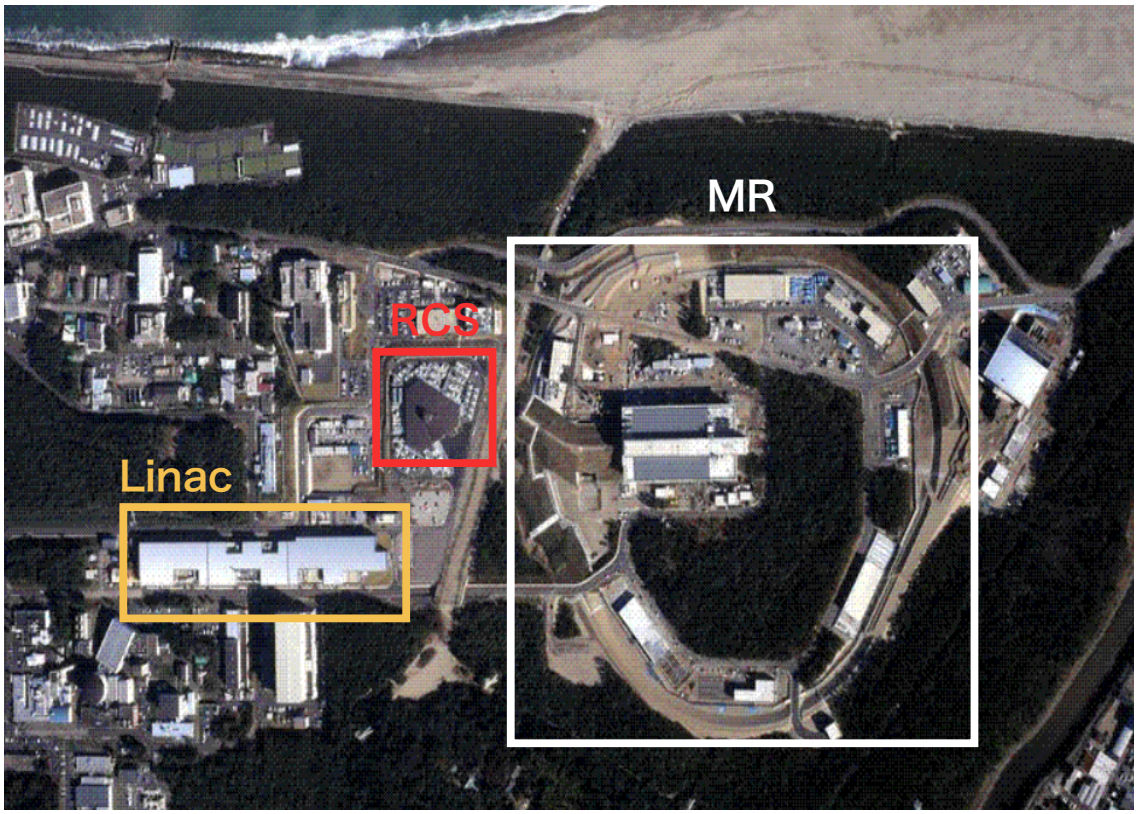


Figure 2.2: Aerial photograph of J-PARC. The LINAC can accelerate protons up to 400 MeV, the RCS accelerates protons up to 3 GeV, and the MR can accelerate protons up to 50 GeV.

J-PARC consists of series of accelerators such as a LINAC that accelerates protons up to 400 MeV, a Rapid-Cycling Synchrotron (RCS) that accelerates protons up to 3 GeV, and a Main Ring (MR) that accelerates protons up to 50 GeV. The accelerated protons are used for multiple purposes, for instance in the materials and life science experiments such as non-destructive inspection using neutron diffraction, physics experiments using muons or neutrons, and so on. The MR protons are used for neutrino experiments or hadron experiments. The basic specifications of J-PARC are summarized in Table 2.1, and a schematic view of J-PARC is shown in Figure 2.2.

| Accelerator | LINAC | RCS | MR |
|---|---|---|---|
| Beam power | 200 kW | 1 MW | 750 kW |
| Beam repetition | 25 Hz | 25 Hz | 0.3 Hz |
| Beam current | 50 mA | 333 $\mu$A | 25 $\mu$A |

Table 2.1: Basic specifications of J-PARC [25].

### 2.3.2 Materials and Life science experimental Facility

Materials and Life science experimental Facility (MLF) [26] is one of the multipurpose experimental facilities in J-PARC. In this facility, experiments on materials and life sciences, and fundamental physics using neutrons and muons are carried out. The MLF can provide the world's highest-intensity pulsed neutron and muon beams for users. A schematic top-view of the MLF is shown in Figure 2.3. There are four muon beamlines and 23 neutron beamlines including those under construction. About 10% of the provided protons are used to generate muons, and the remaining protons are used to generate neutrons. A carbon target and mercury target are used for the muon and neutron sources, respectively. The neutron source is shown in Figure 2.4. This neutron source has three types of moderators: named coupled, decoupled, and poisoned, to provide neutron beams of various energies and intensities. The coupled and the decoupled moderators are classified according to whether they have a neutron absorber between moderator and reflector. The decoupled moderator has a neutron absorber, and it can provide a narrower width and less intense neutron pulse than that of a coupled moderator. This moderator is suited for the analysis for material structures with a high resolution. On the other hand, the coupled moderator, which has a high intensity and wide pulse width, is suited for experiments that need high intensities. The poisoned moderator has an additional neutron absorber at a certain moderator depth. This moderator provides a neutron pulse that has a narrower width than that of the decoupled moderator provides. The mercury target is placed at the center of the neutron source, and it is surrounded by moderators. The mercury target and moderators are covered with a beryllium reflector, and they are placed within steel and concrete radiation shielding. Generated neutrons are sent into 23 beamlines, and are turned on or off by a shutter made of steel and polyethylene. Our experiment is being carried out at BL05, which uses a coupled moderator to obtain high-intensity neutrons.

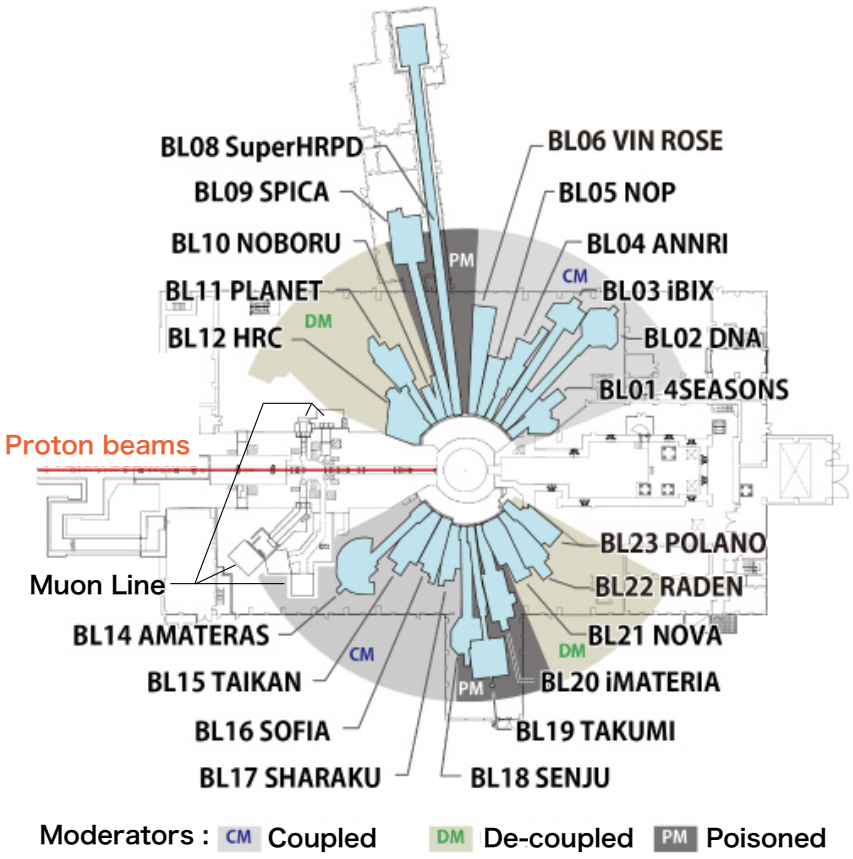


Figure 2.3: Schematic top-view of the MLF. There are four muon beamlines and 23 neutron beamlines, including those under construction. Neutron beams are classified into three groups depending on the type of moderator.

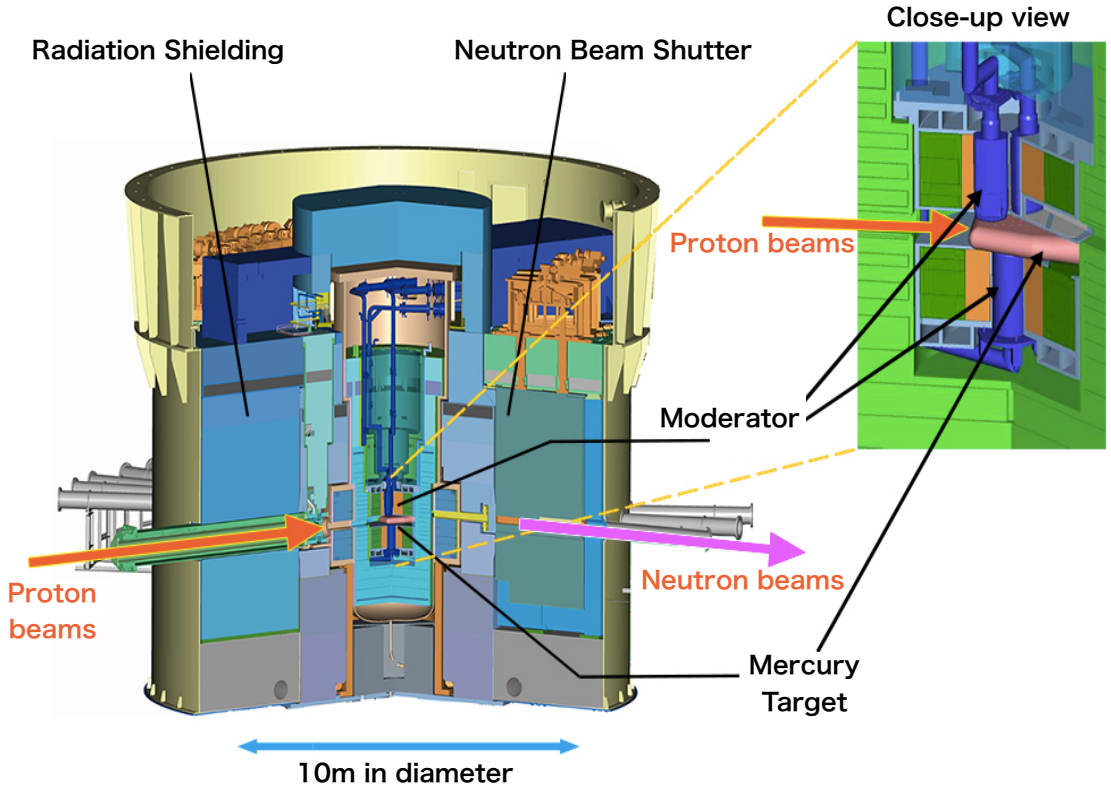


Figure 2.4: Neutron source at the MLF. The mercury target is placed closest to the neutron source, and it is surrounded by three kinds of moderators. The mercury target and moderators are covered with a beryllium reflector, and they are placed within steel and concrete radiation shielding. The beam shutter is made of steel and polyethylene.

### 2.3.3 BL05 (NOP)

BL05 (NOP) is a beamline constructed for neutron optics and fundamental physics [27]. A schematic view of BL05 is shown in Figure 2.5. In BL05, in order to cope with the various experiments, cold neutrons provided from the neutron source of the MLF are divided into three beam branches. One of them is a low divergence beam branch, which is used for experiments requiring neutrons with a low divergence such as small-angle neutron scattering. Another beam branch is an unpolarized beam branch, which can provide the highest intensity neutron beam from BL05. This beam branch is used for UCN generation because it has advantages in terms of the statistics. The other one is a polarized neutron beam branch, which can provide highly polarized neutrons (>95% polarization) [28]. The specifications of each beam branch are summarized in Table 2.2. Our experiment uses the polarized neutron beam branch to reduce background events. The approach to background reduction will be discussed in the following section.

| | Low divergence | Un-polarized | Polarized |
|---|---|---|---|
| Beam size [mm$^2$] | $80 \times 20$ | $55 \times 45$ | $80 \times 50$ |
| Beam divergence [$\mu$str] | $5.4 \times 10^{-2}$ | $1.0 \times 10^{2}$ | $1.9 \times 10^{2}$ |
| Beam intensity [n/sec/cm$^2$] | $5.4 \times 10^{4}$ | $9.4 \times 10^{7}$ | $3.9 \times 10^{7}$ |
| Polarization | – | – | >95% |

Table 2.2: Specifications of each beam branch of BL05. The calculated values assume 1 MW operation of J-PARC, and 16 m from the moderator of the neutron source [25, 27, 28].

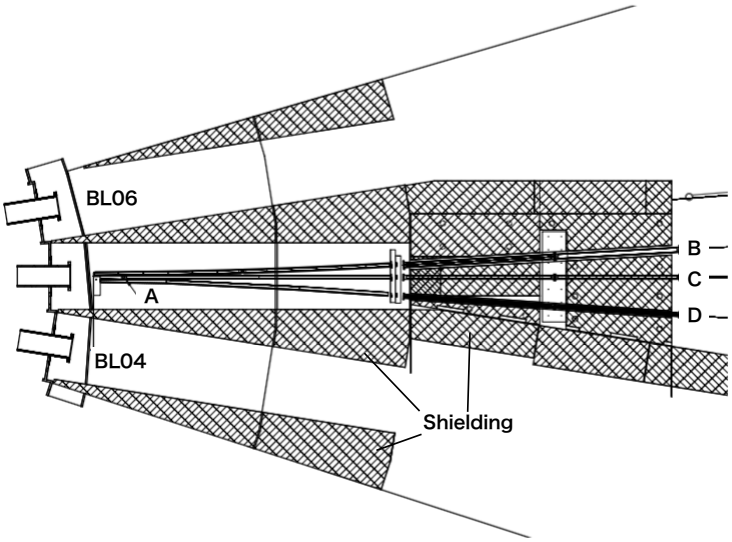


Figure 2.5: Schematic view of BL05. A : upstream beam bender, B : polarized beam branch, C : unpolarized beam branch, D : low divergence beam branch. The exit of each beam branch is located at 16 m from the moderator surface of the neutron source [27].

## 2.4 Experimental apparatus

In this section, our experimental apparatus will be explained. Our experiment has some unique features to obtain better statistics and less background events.

### 2.4.1 Setup

The setup for neutron lifetime measurement at J-PARC is shown in Figure 2.6. Neutron beams are formed as short bunches by using the Spin Flip Chopper (SFC). Then, these short bunches are transported into the TPC. The neutron flux is measured by the beam monitor, and neutron beam is turned on or off by the $^6$LiF shutter. The details of each device are described in the following sections.

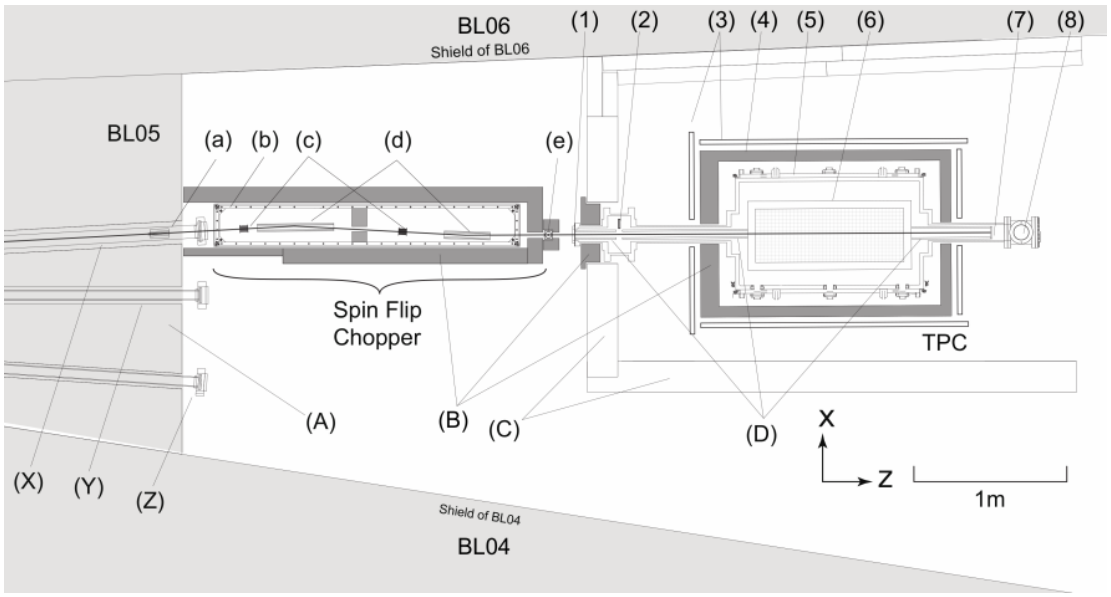


Figure 2.6: Setup for neutron lifetime measurement at J-PARC. (A): shielding, (B): lead shields, (C): iron shields, (D): $^6$LiF beam collimators, (X): polarized neutron branch, (Y): un-polarized neutron branch, (Z): low divergence neutron branch, (a): wavelength filter, (b): guide coil, (c): flipper coil, (d): magnetic super mirrors, (e): beam monitor, (1): Zr window, (2): $^6$LiF shutter, (3) veto counters, (4): lead shields, (5): vacuum chamber, (6): TPC, (7): $^6$LiF beam catcher, (8): turbo molecular pump.

### 2.4.2 Spin Flip Chopper

The SFC is the most unique device in our experiment [29]. This device can form the neutron pulse into short bunches by utilizing the neutron spin. A schematic top-view together with a photograph are shown in Figure 2.7. The SFC consists of two spin flipper coils, three magnetic super mirrors and a guide coil to hold the neutron polarization.

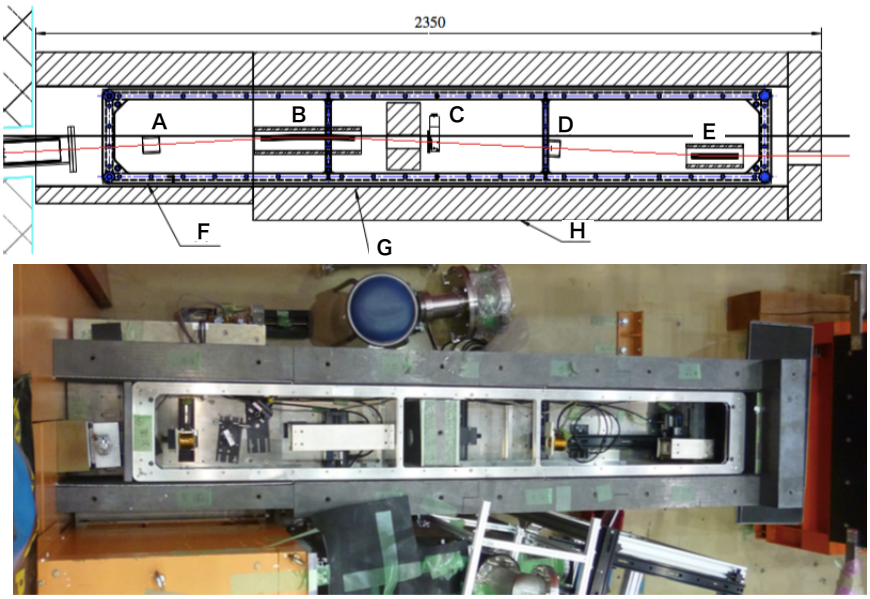


Figure 2.7: Schematic top-view (top) and the photograph (bottom) of the SFC. There are two spin flipper coils, three magnetic super mirrors, and a guide coil. A : first spin flipper coil, B : first and second magnetic super mirrors, C : $^{6}$LiF collimator, D : second spin flipper coil, E : third magnetic super mirror, F : guide coil, G : $^{10}$B absorber, H : lead shielding.

The spin flipper is a device for flipping the neutron spin using Larmor precession due to an oscillating magnetic field. The magnetic super mirror consists of thin alternating layers of ferromagnetic and non-magnetic materials, and it can reflect only neutrons that have the same spin direction as the direction of the magnetic field when placed in the magnetic field. The guide coil creates a static magnetic field in the SFC and prevents from depolarization of the neutron spin. By combining this equipment, the neutron pulse can be formed into neutron bunches. The time structure of the MLF beam and bunch structure of BL05 are shown in Figure 2.8. By using the SFC and the formed neutron bunches, it is possible to reduce the number of gamma ray background events caused by the neutrons while the neutron bunches pass through the detector.

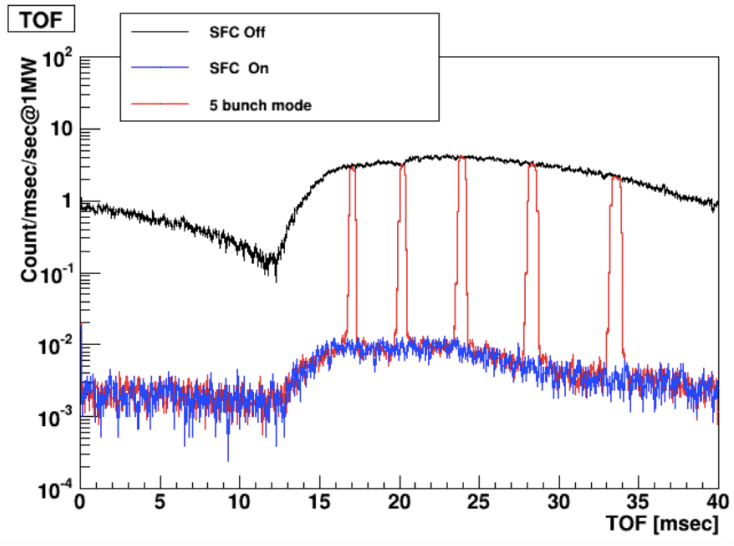


Figure 2.8: Time structure of the MLF beam and bunch structure of BL05. The SFC forms the pulsed neutron beam into five bunches to minimize the number of background events caused by neutron hits on the TPC or other materials.

### 2.4.3 Beam monitor

A beam monitor is placed downstream of the SFC. In order to reduce the number of gamma ray background events, we use a $^{6}$LiF shutter, which will be described in the next section, to take data with and without neutrons introduced into the TPC. The beam monitor is used to normalize the neutron flux. We employ a detector manufactured by CANBERRA in which $^{3}$He gas is filled. A picture of the beam monitor is shown in Figure 2.9.

### 2.4.4 $^{6}$LiF shutter

As mentioned in the previous subsection, by using the LiF shutter, it is possible to acquire both of data with neutrons and without neutrons. $^{6}$Li has a large neutron absorption cross section ($940 \pm 4$ barn [23]), and since the gamma ray emission probability due to neutron absorption is as small as 0.083%, neutrons can be dumped without increasing the number of gamma ray background events. We made a shutter using a 5 mm thick $^{6}$LiF plate ($^{6}$Li is enriched up to 95% of the included Li), and about 99.98% of the neutrons can be dumped. The opening and closing of this shutter is remotely controlled using a stepping motor. Figure 2.10 shows a picture of the $^{6}$LiF shutter.

Figure 2.9: Picture of the beam monitor.

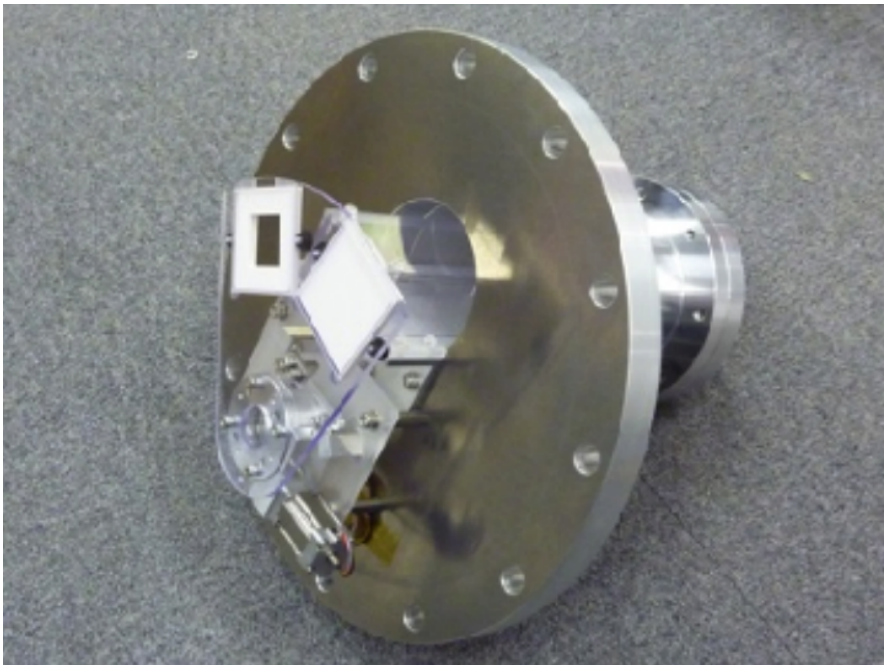

Figure 2.10: Picture of the $^{6}$LiF shutter. The white plate seen in the center of the photograph is a $^{6}$LiF plate.

### 2.4.5 Time Projection Chamber

The TPC is a type of gas detector and consists of a region that drifts electrons, which are ionized along with the passage of charged particles, by using an electric field and a Multi-Wire Proportional Chamber (MWPC) to detect the drifted electrons. The amplifiers to read out the electrical signal are mounted on the MWPC frame. A photograph of our TPC is shown in Figure 2.11. The size of our TPC is 960 mm in the beam axis direction, 300 mm in the vertical and the horizontal directions [30]. The TPC and MWPC frames are made of Poly-Ether-Ether-Ketone (PEEK) [31], which has low radioactive contamination. The wall surfaces of TPC are covered with tiles made of $^{6}$LiF in order to reduce the number of gamma ray background events due to the neutron absorption reaction of the TPC wall as much as possible. These $^{6}$LiF tiles are also covered with Teflon to prevent alpha particle and tritium produced by the neutron absorption reaction of $^{6}$Li from entering the sensitive region of the TPC. There are two slits on one side for the calibration system. The slit positions are shown in Figure 2.12. The details of the calibration system will be described in the next section.

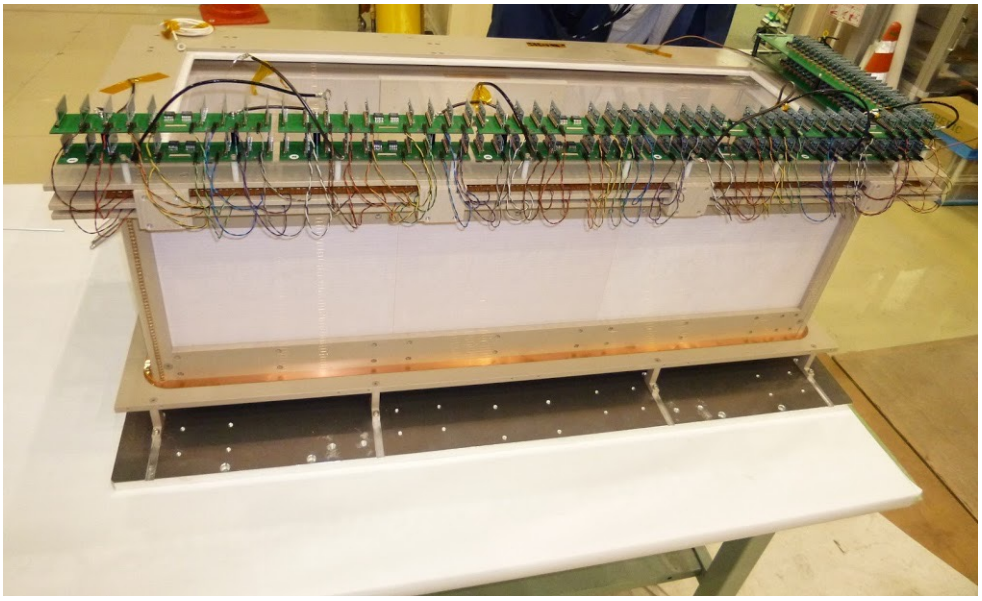

Figure 2.11: Photograph of the TPC. The frames of the TPC and MWPC are made of PEEK, which has low radioactive contamination. The amplifiers to read out the electrical signal are mounted on the MWPC frame. The wall surfaces of the TPC are covered with tiles made of $^{6}$LiF.

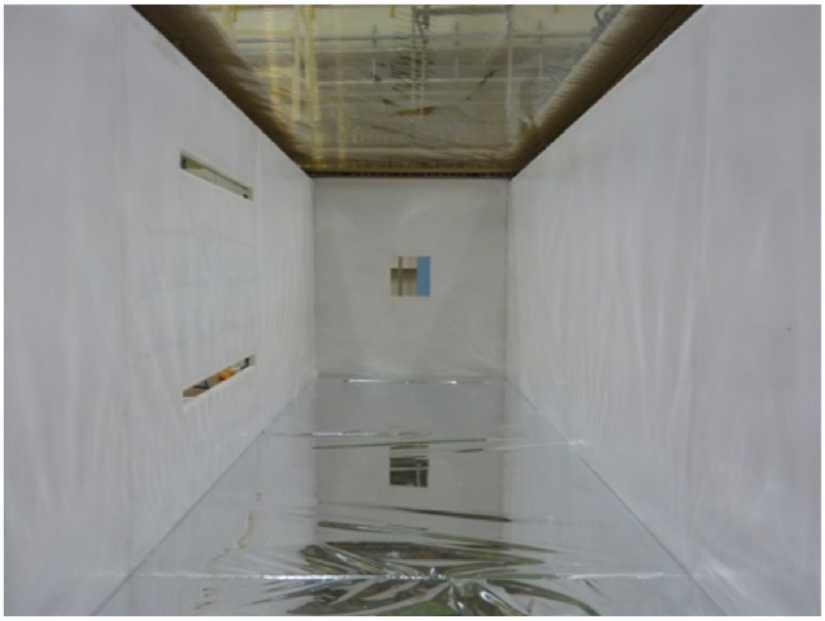

Figure 2.12: Inside photograph of the TPC. There are two slits on one side of the TPC for calibration.

We use $^4$He as the working gas because it has small scattering and absorption cross sections, and we also use $CO_2$ as a quenching gas. The mixing ratio of these gasses is $^4$He:$CO_2$=85:15, and regular operations are carried out at the total pressure of 100 kPa. In the region shown in Figure 2.12, there is an electric field from the bottom to the top of the TPC for transporting ionized electrons. The MWPC has 24 channels of anode wire (applying 1720 V in 100 kPa operation) and 24 channels of field wire (applying 0 V) parallel to the beam axis, and 40 channels of cathode wire (applying 0 V) perpendicular to the beam axis. For the cathode wire, four or five wires merged into a channel. The alignment of each wire is shown in Figure 2.13. The anode wires, field wires, and cathode wires are all sense wires. There are amplifiers on the top of the MWPC to read out the signal coming from drifted electrons and ions. The specifications of the TPC are summarized in Table 2.3.

| | |
|---|---|
| Sensitive region | 300 mm (horizontal)<br>$\times$ 300 mm (vertical)<br>$\times$ 960 mm (beam axis) |
| Anode wire | $\phi$ 20 $\mu$m Gold plated tungsten (AuW) |
| Field wire | $\phi$ 50 $\mu$m Beryllium copper (BeCu) |
| Cathode wire | $\phi$ 50 $\mu$m Beryllium copper (BeCu) |
| Anode channel | 24 channels |
| Field channel | 24 channels |
| Cathode channel | 40 channels |

Table 2.3: Specifications of the TPC

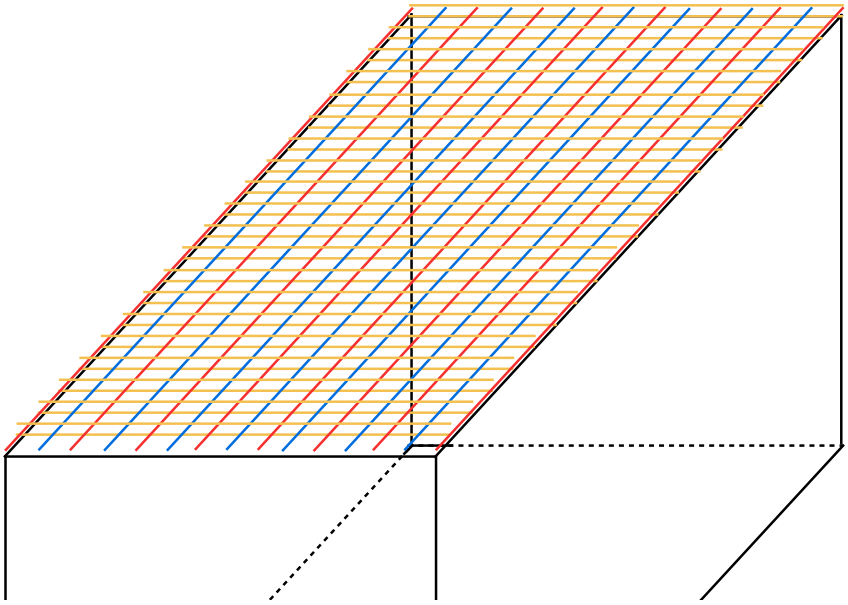

Figure 2.13: Alignment of each wire of the MWPC. Anode wires and field wires are aligned in parallel, and cathode wires are aligned perpendicular to the anode wires. Red lines are anode wires, blue lines are field wires and yellow lines represent cathode wires.

### 2.4.6 Calibration system

In our experiment, X-rays from $^{55}$Fe are used as the calibration source of the TPC. This $^{55}$Fe source is attached to the rotating stage, which is controlled by a stepping motor, and it is possible to irradiate X-rays into the TPC from slits opened at 75 mm and 225 mm from the bottom of the MWPC. The reason for using two slits is to evaluate the effect of attenuation inside the TPC. During data acquisition, the calibration data at the near position (75 mm) and far position (225 mm) are collected once per hour.

### 2.4.7 Cosmic veto system

The cosmic veto system consists of several pairs of plastic scintillators, wave length sifters, and photomultiplier tubes. This system it the most efficient at reducing the cosmic background. This cosmic veto system covers the entire surface, except the bottom of the lead shielding of the vacuum chamber. The bottom surface of the vacuum chamber is supplemented by a plastic scintillator for the cosmic ray trigger, which is placed inside the lead shielding. According to the evaluation of the detection efficiency of this cosmic veto system, the detection efficiency for cosmic rays was more than 99%. The count rate of the cosmic background was reduced from 55 cps to 0.5 cps using this veto system. It is possible to acquire the cosmic events by reversing the veto condition, which is useful in calibrating the drift velocity of electrons in the TPC. At 100 kPa, it was typically 1.1 cm/$\mu$sec.

## 2.5 Data acquisition system

The data acquisition system of this experiment is shown in Figure 2.14. The signals on the wires of each event are recorded by a Flush Analog to Digital Converter (FADC) and Time to Digital Converter (TDC) [32] to obtain the waveform and time information, respectively. To reduce the number of background events from environmental gamma rays, the vacuum chamber that contains the TPC is covered with lead shields. Furthermore, in order reduce the number of background events due to cosmic rays, a cosmic veto system using plastic scintillators is placed around the lead shields. During data acquisition, a coincidence of hit on the anode wire and no hit on the cosmic veto system is used as the trigger.

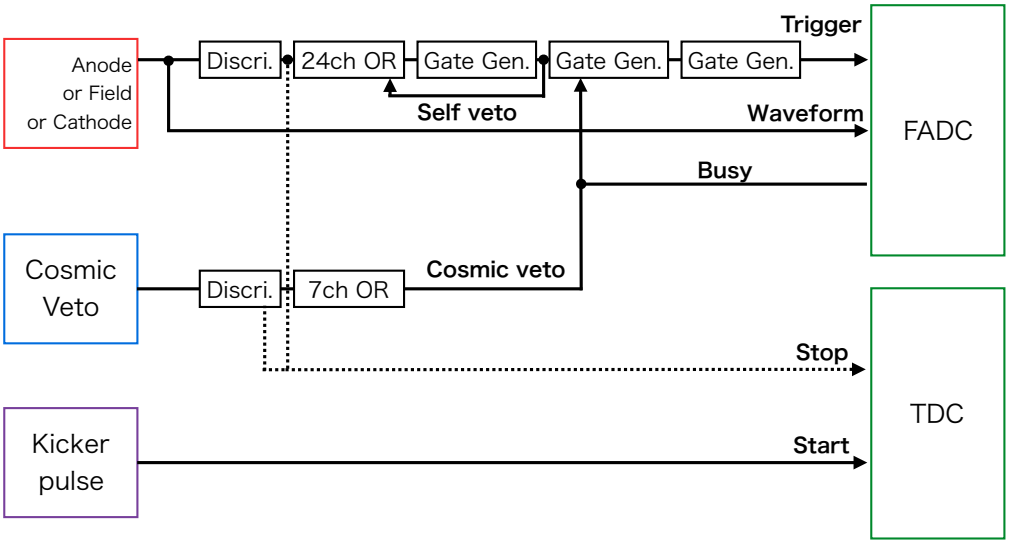


Figure 2.14: Block diagram of the data acquisition system. The trigger signal is generated by a coincidence of hit on the anode wire and no hit on the cosmic veto system. The kicker pulse from J-PARC is used for the TDC start.

Since the FADC is working with 10 MHz sampling, the maximum time range of an event is 100 $\mu$sec, and when a cosmic ray event is observed by the cosmic veto, a dead time of 70 $\mu$sec is set. The time information of the kicker pulse corresponding to the timing of the proton colliding with the mercury target provided by J-PARC is used as the start signal of the TDC.

## 2.6 Simulation

The efficiencies for neutron $\beta$ decay and neutron absorption by $^3$He, as well as the number of background events caused by scattered neutrons, are estimated using a Monte Carlo simulation. The Monte Carlo simulation is carried out in two parts. The first part is a simulation of a particle interaction in the TPC by Geant4. In this part, various kinds of particle interactions are simulated, and their deposit energy, interaction point, and time are recorded. The second part simulates the response of the detector. The waveforms of all wires are simulated with information from Geant4. We take into account diffusion, recombination, and attenuation to convert the results of Geant4 to a waveform. This waveform has the same data format as that of the experimental data, therefore the same analysis code can be applied to the simulated data. A list of Monte Carlo samples is shown in Table 2.4.

| Samples | Types |
|---|---|
| Neutron $\beta$ decay (on axis) | Signal |
| Neutron $\beta$ decay (off axis) | Background |
| $^3$He$(n,p)t$ reaction (on axis) | Signal |
| $^3$He$(n,p)t$ reaction (off axis) | Background |
| $^{55}$Fe source (near) | Calibration |
| $^{55}$Fe source (far) | Calibration |
| Cosmic ray | Calibration |
| $^6$LiF absorption | Background |
| $CO_2$ absorption | Background |

Table 2.4: List of Monte Carlo samples.

### 2.6.1 Simulation of particle interaction

We simulated the entire experimental apparatus. Figure 2.15 shows a snapshot of the simulated apparatus. From the innermost part, the TPC, vacuum chamber, beam duct, lead shields, veto counter, and L-shaped iron shield are shown in Figure 2.15.

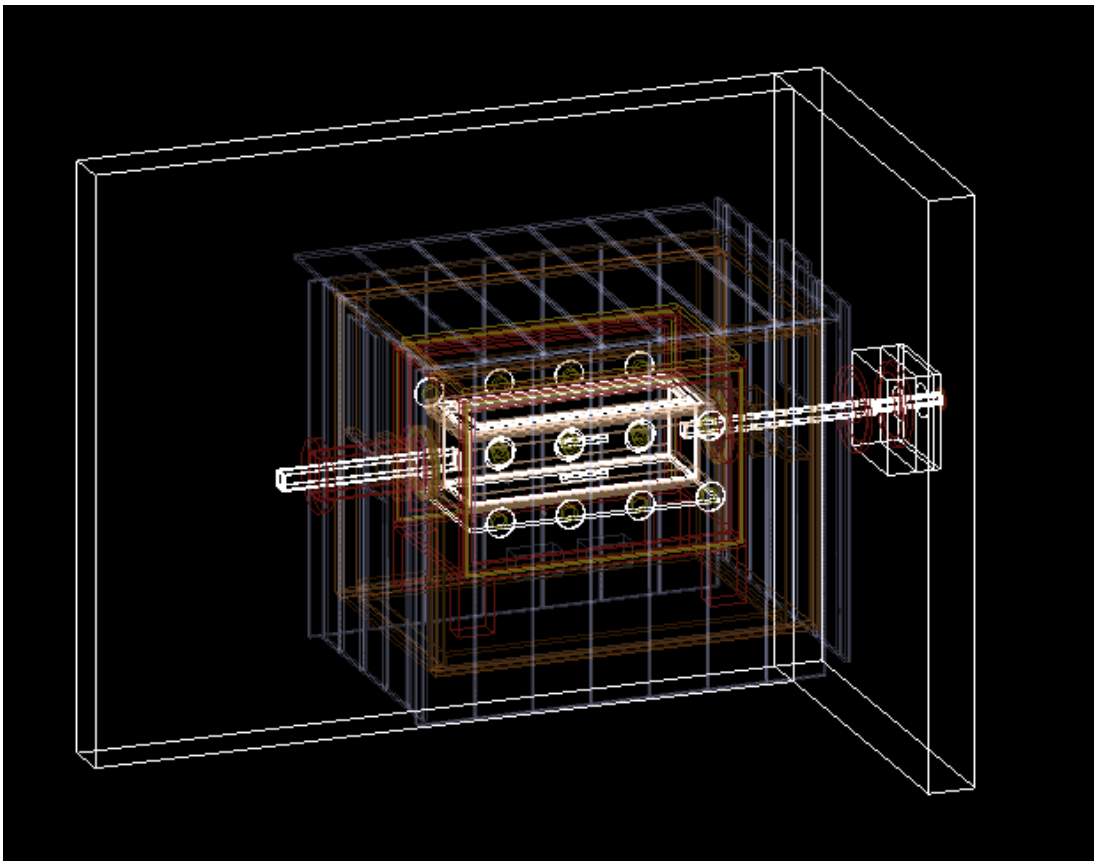

Figure 2.15: Snapshot of the simulated apparatus. From the innermost part, the TPC, vacuum chamber, beam duct, lead shields, veto counter and L-shaped iron shield are shown.

The parameters of particle simulation, such as the measured beam structure, pressure of the operating gas, temperature, and status of the $^6$LiF shutter, are provided to the simulation. This information is necessary to determine the probability of a particle interaction in the TPC. Finally, we can obtain the deposit energy, interaction point, and time of each simulated event.

### 2.6.2 Simulation of the detector response

The detector response is calculated using the deposit energy, interaction point, and time simulated by Geant4. The drift process of an electron in the TPC, and its amplification process near the MWPC are simulated by taking into account diffusion, recombination, and attenuation in the operating gas. Finally, a waveform is generated for each wire with electrical noise and pedestal offset. The gain of each wire and the drift velocity are adjusted to reproduce the experimental values using the calibration data.

## 2.7 Result of 100 kPa operations

We measured the neutron lifetime with 1% statistical uncertainty by the electron counting method during 100 kPa operations of the TPC by 2016. Although the details of the analysis flow will be described in a later chapter, we obtained the first result of $\tau_n = 896 \pm 10(\text{stat.})\ ^{+14}_{-10}(\text{sys.})$ sec as a result of analyzing the data from 100 kPa operations. Figure 2.16 shows our result together with the plots in Figure 1.5. Through analyzing the data for 100 kPa,

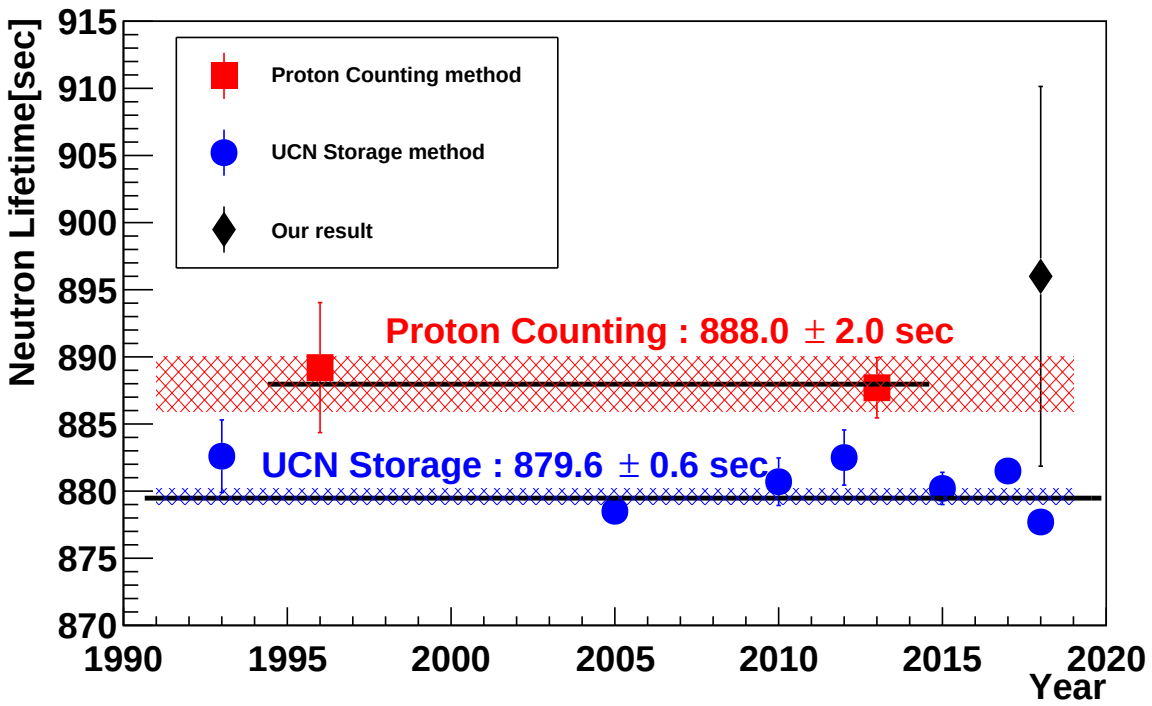


Figure 2.16: Summary of neutron lifetimes for all three methods. The proton counting method is shown with squares and the UCN storage method is shown with circles. The statistical uncertainty of our result is around 1%, as shown in the figure with diamond.

we found that the largest uncertainty is due to the background events caused by neutrons scattered by the operating gasses. These background events are difficult to distinguish from neutron $\beta$ decay events, and the reason will be described in Section 3.1. The background events caused by scattered neutron are an important issue to be solved in order to improve our experimental accuracy.

# Chapter 3

# Studies for low gas pressure operation

In order to reduce the background events from scattered neutrons, we reduced the operating gas pressure of the TPC. In this chapter, we describe the results of the test operation of the TPC at low gas pressures and the development of a new amplifier.

## 3.1 Motivation for low pressure operation

Since various nuclides have scattering cross sections for neutrons, a certain number of neutrons are scattered by the operating gasses in the TPC. These scattered neutrons hit the wall of the TPC or the beam duct, and then gamma rays are generated by the $(n, \gamma)$ reaction with a certain probability. If these gamma rays generate electron by Compton scattering, it can show up as a background event. An illustration of a background event caused by a scattered neutron is shown in Figure 3.1. Analyzing the data at 100 kPa, it was confirmed that the background events due to these scattered neutrons existed in about 5% of the $\beta$ decay events. Thus, in order to realize the measurement with 0.1% accuracy, it is crucial to reduce the number of these background events. Since the operating gas has a certain neutron scattering cross section, it is possible to reduce the amount of scattered neutrons by reducing the absolute number of operating gas molecules. The scattering and absorption cross sections of He and $CO_2$ for neutrons are summarized in Table 3.1. The scattering cross section of $CO_2$ is approximately four times of that of $^4$He. These scattering cross sections are sufficiently small compared to the other various nuclei; however, in order to achieve a measurement with 0.1% accuracy, it is necessary to remove the background caused by scattered neutrons.

| Nuclei | Scattering cross section [barn] | Absorption cross section [barn] |
|---|---|---|
| $^3$He | 6 | 5333 |
| $^4$He | 1.34 | 0 |
| C | 5.551 | 0.0035 |
| O | 4.232 | 0.00019 |
| $CO_2$ | 4.67 | 0.0013 |

Table 3.1: Scattering and absorption cross sections of various nuclei for 2200 m/s neutrons. The values for C and O are calculated using the natural abundance of each nuclei, and the value for $CO_2$ is calculated using the molar ratio [23].

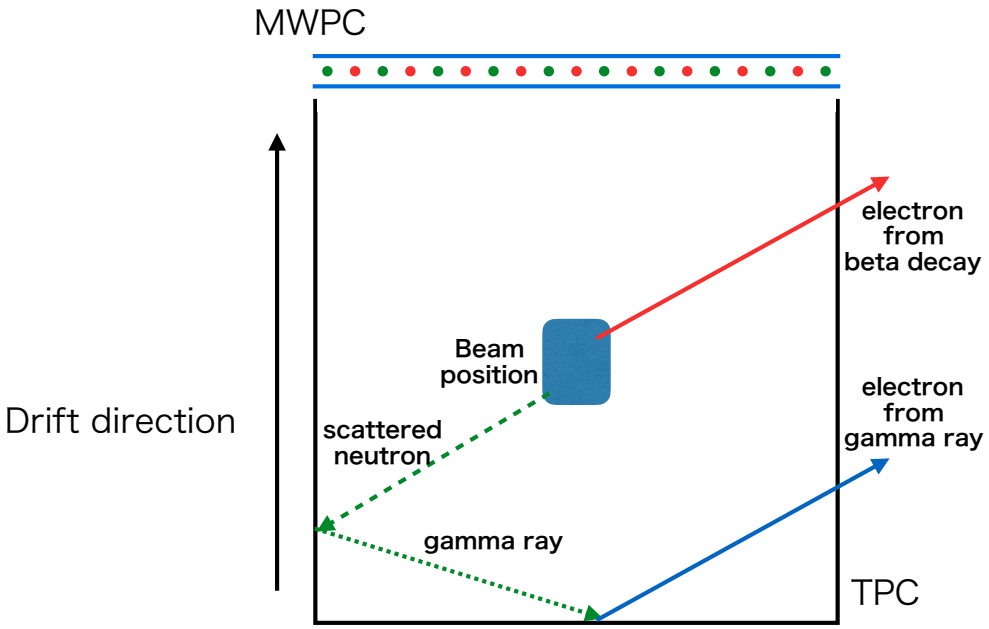


Figure 3.1: Illustration of a background event caused by a scattered neutron. The scattered neutron hits the wall of the TPC and generates gamma rays with a certain probability. If these gamma rays generate electron by Compton scattering, it can show up as a background event. The red dots at the MWPC represent anode wires, the green dots represent field wires, and the blue lines are cathode wires.

## 3.2 Test operation at J-PARC

In September 2016, we carried out a TPC operation test at low gas pressure at J-PARC. In this test, evaluation of the gain of the TPC by a $^{55}$Fe source was performed. At this time, we did not use a neutron beam for the test.

### 3.2.1 Setup

In order to investigate the robustness of our TPC and optimize the data acquisition conditions at low gas pressures, the test was carried out under the conditions of 25 kPa of the mixture of $^4$He and $CO_2$, and 15 kPa, 7.5 kPa, and 3.75 kPa of $CO_2$ gas only. The data acquisition for only $CO_2$ gas is also for testing the feasibility of mono-gas mixture operation. To optimize the data acquisition, the high voltage applied to the anode wire was adjusted. This is because of Paschen's law concerning spark discharge [33]. The Paschen's law is represented using the gas pressure $P$ and distance between electrodes $d$ as

$$V = \frac{C_1 P d}{\ln(C_2 P d) - \ln[\ln(1 + \frac{1}{\gamma_{se}})]} \tag{3.1}$$

where $V$ is the breakdown voltage, $C_1$ and $C_2$ are constants which are determined experimentally, and $\gamma_{se}$ represents the secondary electron emission coefficient. We reduced the voltage applied to the anode wire and adjusted it so that no discharge occurred for each gas pressure. The voltage applied to the anode wire for each gas pressure is shown in the Table 3.2.

| Gas pressure | Voltage on anode wire [V] |
|---|---|
| $^4$He + $CO_2$ 25 kPa | 1180 |
| $CO_2$ 15 kPa | 1720 |
| $CO_2$ 7.5 kPa | 1400 |
| $CO_2$ 3.75 kPa | 1180 |

Table 3.2: Voltage applied to the anode wire for each gas pressure. The lower the gas pressure, the lower the voltage applied to the anode wire for the same gas mixture. The $CO_2$ 15 kPa corresponds to the amount of $CO_2$ gas in 100 kPa of the mixture gas.

### 3.2.2 Gain evaluation

Using the configuration mentioned in the previous subsection, the evaluation of the gain of the TPC at low gas pressures was performed. A comparison of the gains at 100 kPa and 25 kPa is shown in Figures 3.2 and 3.3. The "near position" indicated in the figure means the data was taken with the slit that is the nearest to the MWPC, and "far position" means the data taken with the slit farthest from the MWPC. The transport efficiency represents the ratio of the gains of the near and far positions. It can be confirmed from Figures 3.2 and 3.3 that the gain of the TPC was 1/3 or less due to the decrease in the voltage applied to the anode wire to meet the decrease of the operating gas pressure.

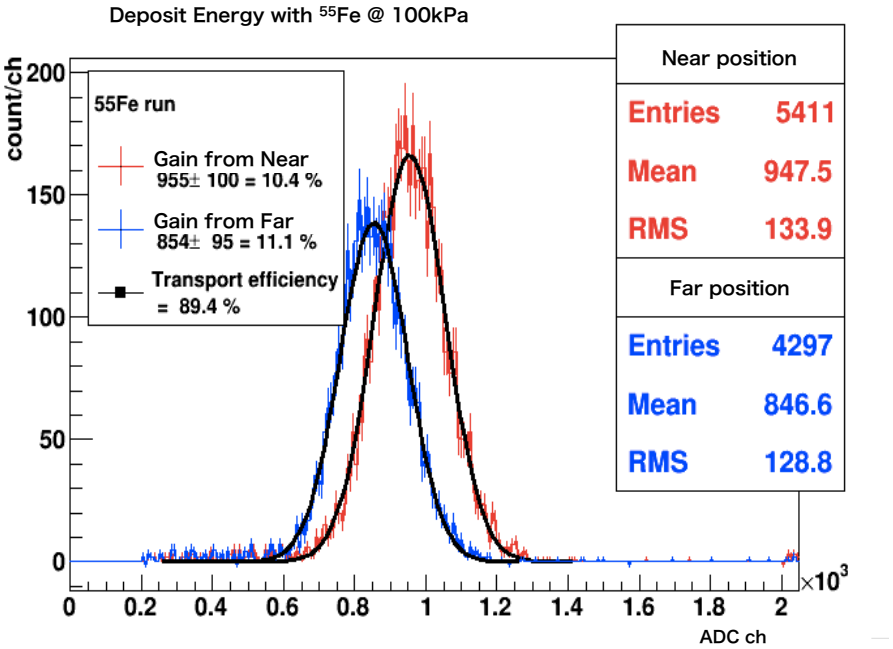


Figure 3.2: Gain at 100 kPa. The calibration source was $^{55}$Fe and the voltage applied to the anode wire was 1720 V. The "near position" indicated in the figure means the data was taken with the slit nearest to the MWPC, and "far position" means the data was taken with the slit farthest from the MWPC. The transport efficiency represents the ratio of the gains of the near and far positions.

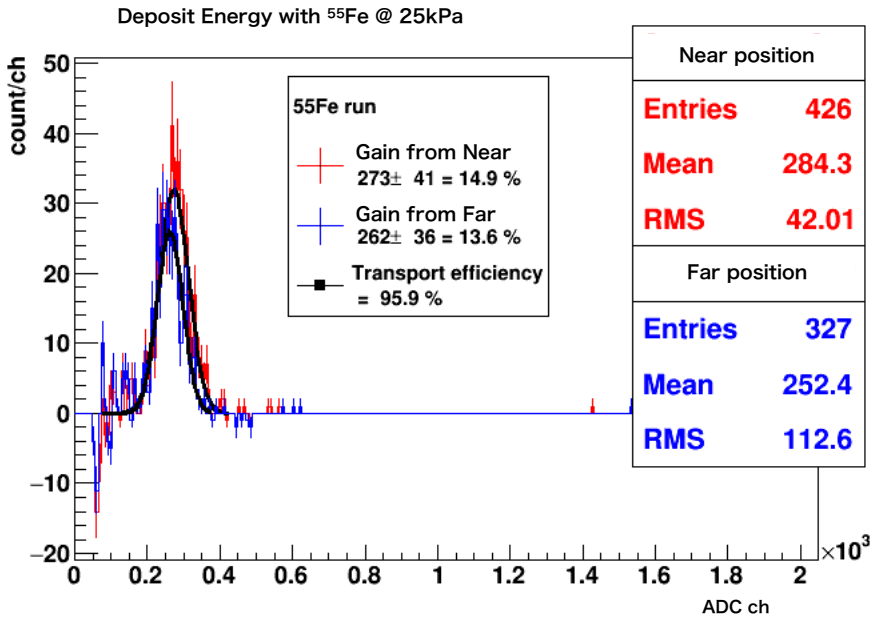


Figure 3.3: Gain at 25 kPa. The calibration source was $^{55}$Fe and the voltage applied to the anode wire was 1180 V. The "near position" indicated in figure means the data was taken with the slit nearest to the MWPC, and "far position" means the data was taken with the slit farthest from the MWPC. The transport efficiency represents the ratio of the gains of near and far positions.

### 3.2.3 Heat generation

Through the low gas pressure operation test, we also confirmed the issue of heat generation by the amplifier in addition to the decrease of gain. This is because the heat exchange between the surface of the amplifier and the operating gas is suppressed by lowering the gas pressure. Figure 3.4 shows the temperature transition inside the TPC due to the gas pressure change, which is monitored during the data acquisition. It can be seen from Figure 3.4 that as the gas pressure decreases, the temperature at the upper side of the TPC rises, and the temperature difference between the upper and lower sides of the TPC increases.

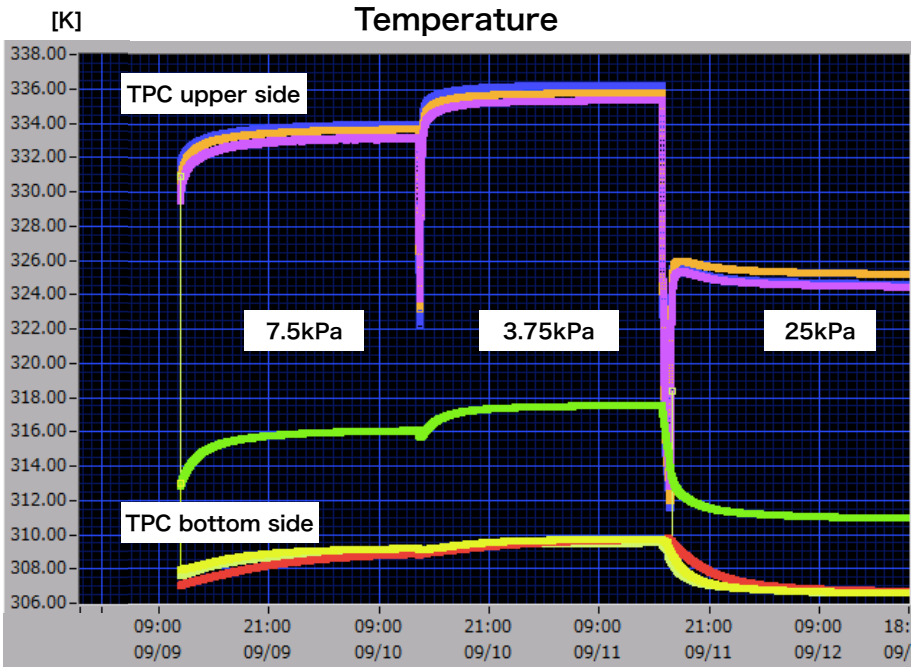


Figure 3.4: Temperature during low gas pressure operation. As the gas pressure decreases, the temperature at the upper side of the TPC rises.

The temperature difference between the upper and lower sides causes the non-uniformity of operating gas in the TPC. If $^3$He is unbalanced in the gas due to this non-uniformity, the density of $^3$He on the beam axis will be different from that assumed at the time of gas introduction, and thus the neutron flux might not be correctly measured. Therefore, it is necessary to suppress this non-uniformity as much as possible, and in order to realize measurement with 0.1% accuracy, it is necessary to reduce the heat generation of the amplifier by at least 1/6.

### 3.2.4 Summary of test operation

After the test operation at low gas pressure, we identified the issues of gain decrease due to the gas pressure decrease and heat generation of the amplifier. Therefore, we developed a new amplifier with low power consumption to solve the heat generation issue. We also developed an additional amplifier to be able to compensate for the TPC gain. Details of these developments will be described in the next section.

## 3.3 Development of new amplifier

The amplifier we currently use is an operational amplifier mounted directly on the board surface, and its power consumption is 500 mW per each channel. Since there are 128 read out channels in total, the total power consumption is 64 W. We have newly developed an amplifier using an ASIC. The ASIC has a feature where the circuit is subdivided and the power consumption is small compared to the surface mounting. Two new amplifiers and one new module were developed. Its circuit and board layout are shown in Appendix A.

### 3.3.1 GTARN amplifier

The NOP and Open-It groups of KEK [34] have developed the GTARN ASIC [35] with a process size of 0.5 $\mu$m. This GTARN has eight channels per chip, and consists of pole zero cancellation circuit, low-pass filter, and analog buffer. Figure 3.5 shows a simplified block diagram. The operating voltage of this ASIC is $\pm$2.5 V, and it is possible to adjust the waveform of the output according to the value of $V_{pre}$. A photograph of the newly developed amplifier using this ASIC is shown in Figure 3.6. This amplifier has 24 channels per board. The input signal comes from the twisted pair cable of the signal and the ground line, and the output signal is fed through the D-sub cable. The signal amplified by the ASIC has a single-ended form. In addition to feeding the output signals, the D-sub cable also feeds the operating voltage of the amplifier, the ground line, and the test pulse for operation confirmation. The blue and yellow boxes in the Figure 3.6 are variable resistors, which allow fine adjustment of the voltage applied to the ASIC. The metal jumper shown in the lower part of the Figure 3.6 is jumper for selecting whether to input the test pulse into the ASIC or not.

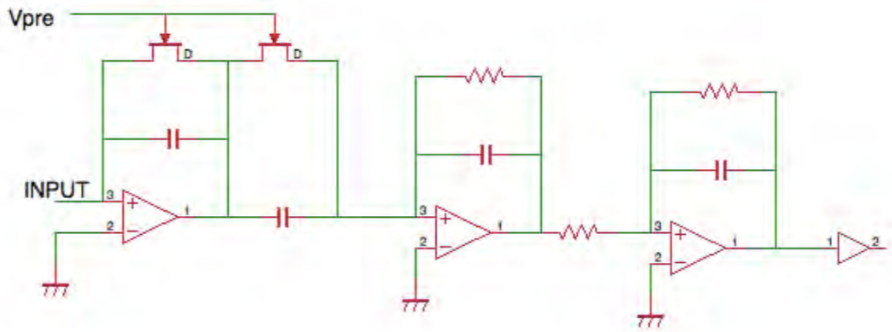


Figure 3.5: Simplified block diagram of the GTARN amplifier. $V_{pre}$ is a bias voltage on the first block, and it can control the waveform of the output [36].

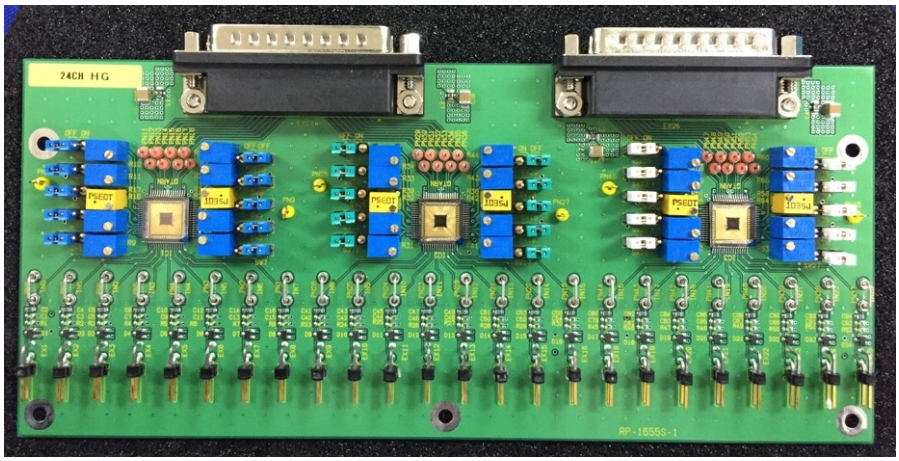

Figure 3.6: Photograph of the GTARN amplifier. It has 24 channels per board. The blue and yellow boxes are variable resistors to adjust the voltage applied to the ASIC. The input connector consists of 24 twist pair cables and output connector consists of two D-subs.

### 3.3.2 Additional amplifier

We have developed an additional amplifier to compensate for the gain of the GTARN amplifier. This additional amplifier is placed outside the vacuum chamber in order not to affect the distribution of the operating gas in the TPC. A photograph of the additional amplifier is shown in Figure 3.7.

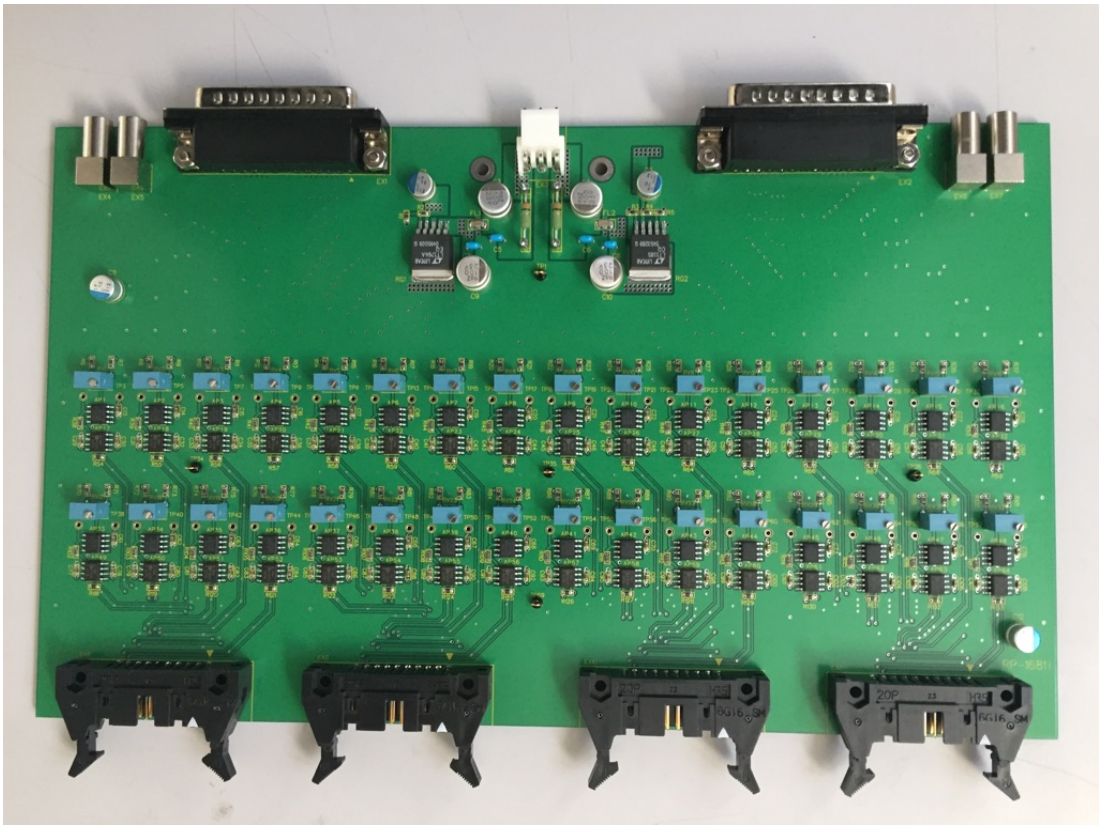

Figure 3.7: Photograph of the additional amplifier. It has 32 channels per board. This amplifier can output a differential signal with a single end as the input.

This additional amplifier has 32 channels of input/output per board, and it converts the single-ended signal input through the D-sub cable into a differential output. The differential signals are fed through the flat cable. In addition to signal amplification and conversion, this additional amplifier is also responsible for supplying power to the GTARN amplifier and test pulses. Furthermore, the offset of the output waveform can be adjusted by changing the values of the variable resistors, and the amplification factor is also adjustable.

### 3.3.3 Read out system for new amplifier

In order to cope with the read out system using the GTARN and additional amplifier, we modified the trigger generation module in the DAQ system. This is necessary because the existing system assumes a single-ended output; therefore, we developed a system that can create a trigger by setting the threshold even for a differential output. Figure 3.8 shows a

picture of the developed module. This module has two outputs; one of them is a system that divides the input differential signals into two outputs. The other is a system that triggers using an internal discriminator.

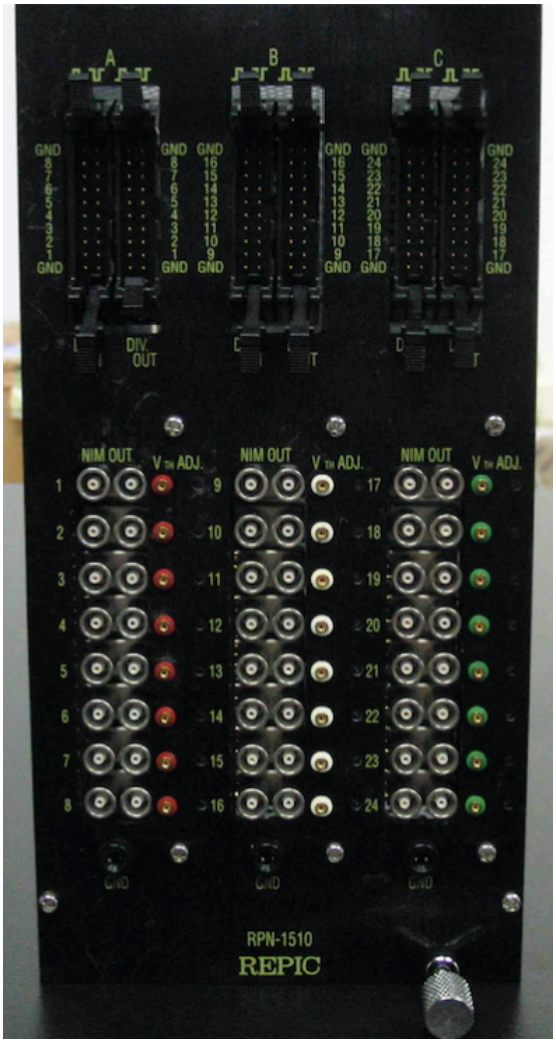


Figure 3.8: Photograph of the module for the developed amplifier. This module has two outputs; one of them is a system that divides the input differential signals into two outputs. The other is a system that triggers using an internal discriminator.

## 3.4 Evaluation of newly developed amplifier

### 3.4.1 Power consumption

The power consumption of the developed amplifier using the ASICs was estimated from the measured current when the voltage was applied from a power supply, and it was 9 mW per channel. This value corresponds to 1/50th that of the currently used amplifier. As mentioned in the previous chapter, our reduction requirement for the power consumption was 1/6th taht of current amplifier; this improvement is sufficient to achieve 0.1% accuracy for the non-uniformity of $^3$He.

### 3.4.2 Gain linearity

The evaluation of the gain of the developed amplifier was carried out using a test pulse. A rectangular wave was input from the function generator to the amplifier as a test pulse, and we observed its output using an oscilloscope. A schematic diagram of the measurement setup is shown in Figure 3.9.

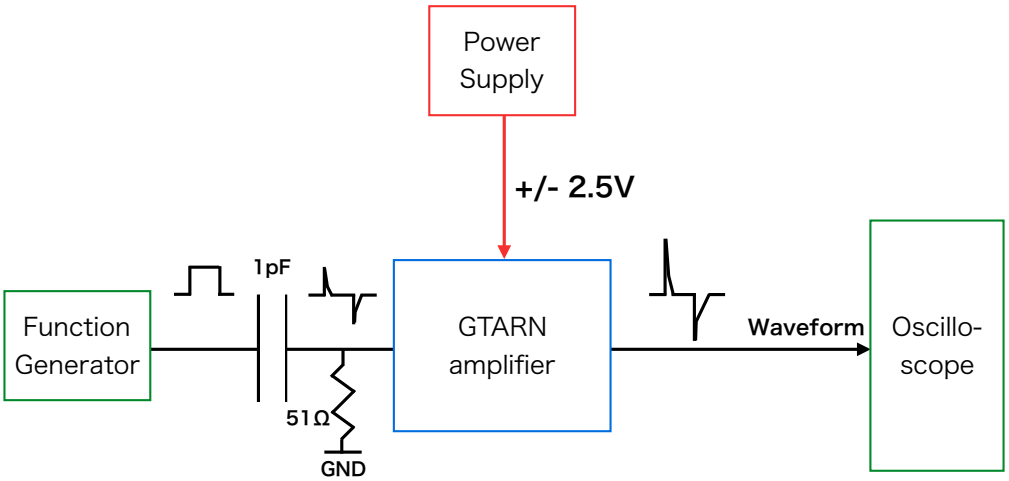


Figure 3.9: Schematic diagram of the measurement for gain evaluation. The input waveform is a rectangular wave by the function generator, and it is converted into a charge using a capacitor. The output waveform is measured using an oscilloscope.

The rectangular wave generated by the function generator is converted into a charge using a differential circuit and input into the amplifier. The signal amplified by the amplifier was transmitted as a single-ended output to the oscilloscope, and we determined the gain as the amplification factor for 1 pC of input charge. The measurement result is shown in Figure 3.10.

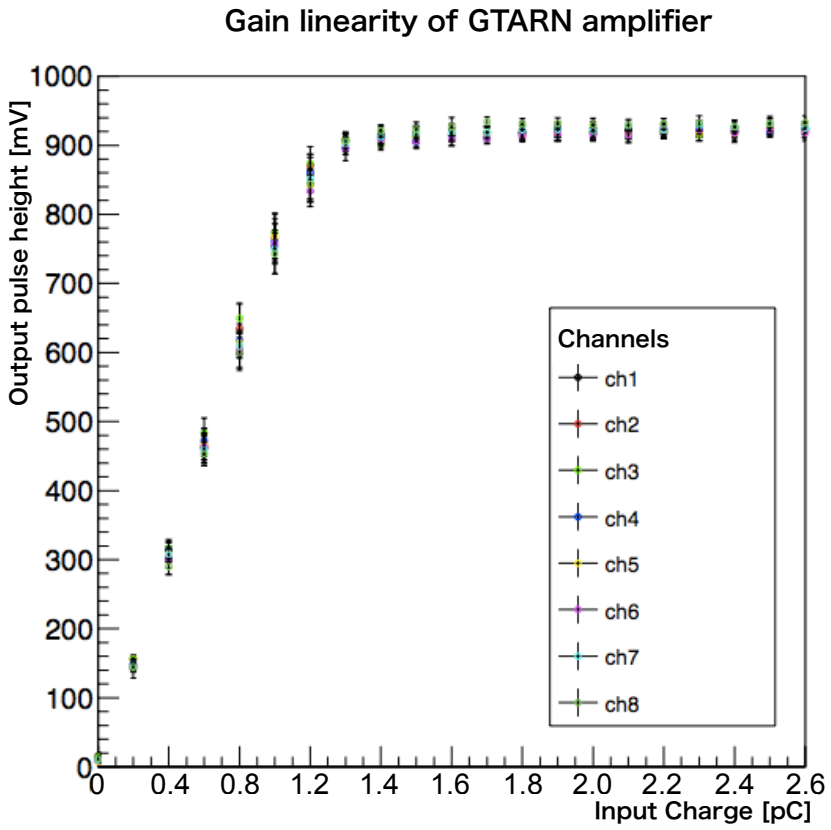


Figure 3.10: Gain linearity of the GTARN amplifier. The linearity is maintained up to the input charge of 1.2 pC. The measured gain is 0.8 V/pC.

As a result of the measurement, it was confirmed that the gain was 0.8 V/pC, and the linearity was maintained up to the input charge of 1.2 pC. In addition, we did not see a significant difference between the channels. The gain of the developed amplifier is 0.8 times smaller than the gain of the currently used amplifier. This is an acceptable amplification using the additional amplifier described in Section 3.3.2.

### 3.4.3 Summary of new amplifier

From the evaluation of the power consumption and gain, the performance of the developed amplifier is summarized in the Table 3.3. The equivalent noise charge (ENC) was evaluated using a test board, and ENC = 4000 for the ASIC alone.

| | value |
|---|---|
| Channels | 24 channels / board |
| Gain | 0.8 V/pC |
| Power consumption | 9 mW / channel |
| Electron noise charge | 4000 |

Table 3.3: Specifications of the newly developed amplifier.

We reduced the power consumption by a factor of 50 compared to the existing amplifier using the newly developed GTARN amplifier. As a result, operations at much low gas pressures can be expected in future data acquisition. In the following chapter, we will discuss neutron lifetime measurement at low gas pressures. In this thesis, however, we did not use this newly developed amplifier in order to maintain consistency with previous physics run.

# Chapter 4

# Neutron lifetime measurement at 50 kPa

In this chapter, the DAQ status and the analysis method are described. From studies at low gas pressures, we expect the feasibility of low gas pressure operation from the viewpoint of hardware requirements. Therefore, in order to confirm that the gas scattering background can be reduced with low gas pressure operation, and that the neutron lifetime can be determined even at low gas pressures, we performed neutron lifetime measurement at 50 kPa.

## 4.1 Collected data

Data collection at low gas pressure was carried out with the operating gas pressure of 50 kPa. The measurement was performed at J-PARC in November 2017, and the acquired data corresponds to around 2% statistical accuracy with a week of measurement time. The operating beam power of J-PARC was 300 kW. The sequence for data acquisition is shown in Table 4.1. The sequence has calibration runs, $^{55}$Fe runs for monitoring the TPC gain, and cosmic ray runs for the calibration of the drift velocity in the TPC. Neutron beams "on" and "off" were measured, as in Table 4.1, in order to cancel the effects of neutron beam presence in the TPC such as electric field distortion due to residual ions.

| DAQ type | DAQ time [sec] |
|---|---|
| Calibration with $^{55}$Fe on near position | 200 |
| Calibration with $^{55}$Fe on far position | 200 |
| Calibration with cosmic ray | 100 |
| Neutron beam on | 1000 |
| Neutron beam off | 1000 |
| Neutron beam off | 1000 |
| Neutron beam on | 1000 |

Table 4.1: Data acquisition sequence. The order of the neutron beam runs was adjusted to cancel the effects of neutron beam presence. The gain of the TPC was monitored using $^{55}$Fe runs and the drift velocity was determined using cosmic ray runs.

We applied a voltage of 1440 V to the anode wire during the data acquisition. We also applied an electric field gradient of 24 V/cm to the drift region. The reason that the operating voltage is lower than for 100 kPa is due to Paschen's discharge law, as described in Section

3.2.1. In addition, the DAQ sequence in which the voltage of the anode wire was lowered to 1000 V was also measured once every two days with the sequence shown in Table 4.2. The measurement with at a low voltage is to evaluate the amount of nitrogen derived from the outgas.

| DAQ type | DAQ time [sec] |
|---|---|
| Neutron beam off | 300 |
| Neutron beam on | 1000 |
| Neutron beam on | 1000 |
| Neutron beam on | 1000 |

Table 4.2: DAQ cycle in low voltage operation.

The neutron absorption reaction by $^{14}$N has a deposit energy that is close to that of the neutron absorption reaction by $^{3}$He in the TPC. The neutron absorption reaction by $^{3}$He and that of by $^{14}$N are saturated and cannot be separated at 1440 V. Therefore, we used a low voltage operation to distinguish these two reaction and estimate the abundance of $^{14}$N in the operating gas. The amount of contaminated $^{14}$N in the operating gas is estimated from the ratio of the number of events of the neutron absorption reaction by $^{3}$He. Furthermore, the measurement of the neutron absorption by $^{17}$O is also carried out using this low voltage DAQ sequence, and the number of contaminated $^{17}$O events to signal events is estimated. For this estimation, we use the pile-up rate of the neutron absorption reaction from $^{3}$He events. The details of this estimation are described in Section 4.6.2.

## 4.2 Scattered neutrons at low gas pressure

In the 50 kPa operation, the number of gas molecules contributing to the neutron scattering will be reduced to half of that at 100 kPa. Therefore, it is expected that the number of scattered neutrons will also decrease along with the gas pressure. This can be confirmed by using the neutron absorption reaction of $^{3}$He with a variable called the Field Center of Energy (FCE). This variable is defined as the center of the deposit energy on the field wires, which is calculated by the formula $\sum_{\mathrm{ch}=0}^{24}(\mathrm{Integral_{ch}} * \mathrm{ch})/\mathrm{F_{sum}}$ with the hit channel (ch), the integral of a certain field wire ($\mathrm{Integral_{ch}}$) and $\mathrm{F_{sum}}$ (energy summation over all field wires). The distribution of the FCE is shown in Figure 4.1. The black dots in Figure 4.1 represent experimental data, the red histogram represents the Monte Carlo simulation of unscattered neutrons, and the blue histogram represents the Monte Carlo simulation of scattered neutrons. The normalization was done using the region containing events only caused by scattered neutrons. In this analysis, FCE from 0 to 4 and from 19 to 23 were used.

The number of scattered neutrons can be estimated by calculating the ratio of the number of events caused by scattered neutrons ($N_{\mathrm{scattered}}$) and those caused by unscattered neutrons ($N_{\mathrm{unstattered}}$). The result of the ratio $R_{50\mathrm{kPa}}$ is calculated to be

$$R_{50\mathrm{kPa}} = \frac{N_{\mathrm{scattered}}}{N_{\mathrm{unscattered}}} = 0.0154 \pm 0.0019. \tag{4.1}$$

Since this ratio at 100 kPa ($R_{100\mathrm{kPa}}$) was $0.0290 \pm 0.0039$, the ratio of scattered neutrons at

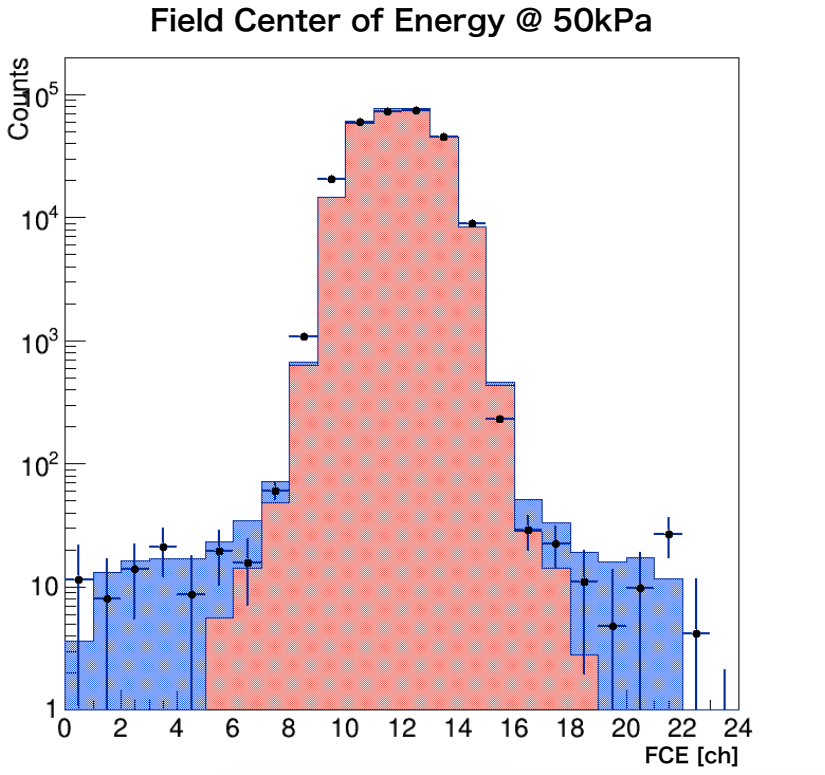


Figure 4.1: Distribution of the FCE. The black dots represents experimental data, the red histogram represents the Monte Carlo simulation of unscattered neutron absorption reaction of $^3$He, and the blue histogram represents the Monte Carlo simulation of the scattered neutron absorption reaction of $^3$He. The normalization was done using the number of events within the FCE from 0 to 4 and from 19 to 23.

50 kPa and 100 kPa, $R_{50kPa}/R_{100kPa}$ is

$$\frac{R_{50kPa}}{R_{100kPa}} = 0.532 \pm 0.043(\text{stat.}). \tag{4.2}$$

From this result, it was confirmed that the number of scattered neutron was decreased by half, as expected by reducing the operating gas pressure by half. This indicates that the attempt to reduce the number of scattered neutron by the lowering the gas pressure is successful, and this is an important result for future low gas pressure operations.

## 4.3 Estimation of the number of signal candidates

As mentioned in Section 2.1, we determine the neutron lifetime with the following formula

$$\tau_n = \frac{1}{\rho\sigma_0 v_0}\frac{N_{^3\mathrm{He}}/\epsilon_{^3\mathrm{He}}}{N_\beta/\epsilon_\beta} \ . \tag{4.3}$$

Therefore we need to estimate $N_{^3\mathrm{He}}$ and $N_\beta$ from the collected data. First, we describe how to reduce the number of background events, and in the following section we will explain

the separation between $N_{^3\mathrm{He}}$ and $N_\beta$. The major background sources of our experiment are as follows:

- Upstream gamma rays coming from the neutron source of the MLF and super mirror in beam transport line, including the SFC. - A
- Environmental radiation, including cosmic rays and gamma rays. - A, B
- Gamma rays produced from neutron absorption by $CO_2$ in the TPC. - B
- Gamma rays produced from neutron absorption by $^6$LiF wall of the TPC. - C
- $\beta$ decay outside the beam axis by scattered neutrons. - C

The background events of Category A are removed by subtracting the events using the time-of-flight (TOF) analysis described in Section 4.3.1. The events in Category B is eliminated by event selection using differences in deposit energy to $\beta$ decay or its event shape. The event selection method is described in Section 4.3.2. We estimate the number of events in Category C using Monte Carlo simulations based on Geant4, and subtract them from the number of signal candidates. The details are described in Section 4.3.3. Among these background events, the events in Category C are the most difficult to estimate. This is because the events of Category C cannot be removed by the subtracting method because these background events occur only when neutrons are present inside the TPC. Furthermore, the event topology of these events is similar to that of $\beta$ decay events; it is therefore difficult to eliminate them by event selection as well.

### 4.3.1 Background study for Category A

Reducing the number of background events in Category A is done by subtracting the events using the distribution of the TOF. The TOF in this experiment is defined as the time difference between the time of the proton colliding to the neutron production target and the time of the trigger generated in the TPC. In order to remove the background events in Category A, we have taken data with the beam on and beam off, as described in Table 4.1. The beam on was operated with the $^6$LiF shutter, which is described in Section 2.4.4, open. With this condition, the neutrons can pass through the TPC, and various reactions occur including neutron $\beta$ decay, neutron absorption reaction by $^3$He, etc. On the other hand, With the beam off condition, data acquisition is carried out with the $^6$LiF shutter closed. As a result, events caused by the neutrons do not occur inside the TPC, and only the time-independent background and background events unrelated to the neutrons are recorded. A schematic view of the "beam on" and "beam off" setups is shown in Figure 4.2. The red line in Figure 4.2 represents the neutron beam. We can eliminate the background events classified as Category A by subtracting the data taken from these two setups. The distribution of the TOF is shown in Figure 4.3.

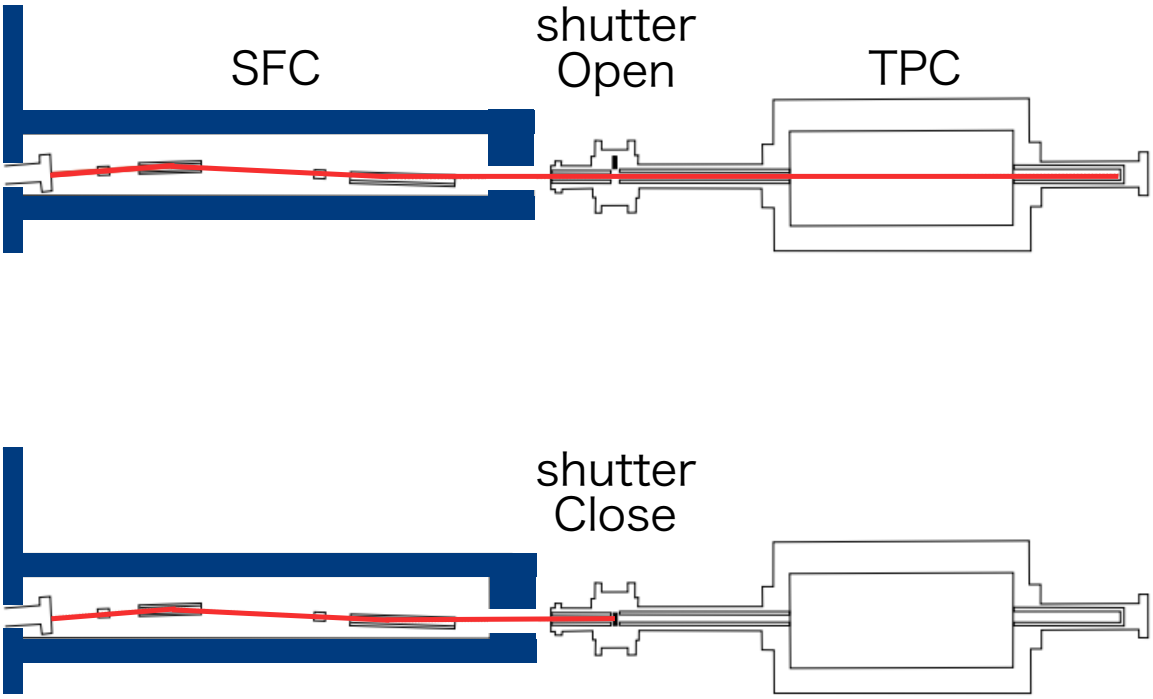


Figure 4.2: Schematic view of "beam on" and "beam off" setups. Neutrons are introduced into the TPC only when the shutter is opened. The red line represents the neutron beam.

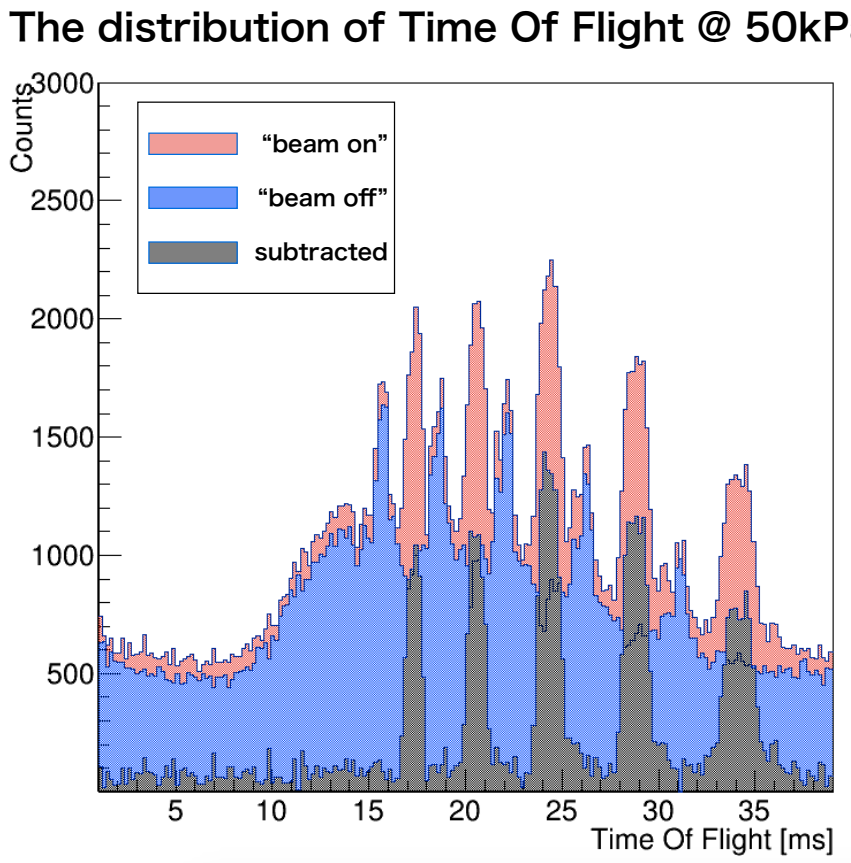


Figure 4.3: Distribution of the TOF. The red histogram is the data taken with the "beam on" setup, and the blue histogram shows the data taken with the "beam off" setup. The black histogram is obtained by subtracting these two histograms. The normalization is done with the number of counts of beam monitor.

In Figure 4.3, the red histogram represents the data taken with the "beam on" setup, the blue histogram is the data taken with the "beam off" setup, and the black histogram represents the result of the subtraction of these two histograms. The number of events is normalized with the number of counts of the beam monitor. As we can see from Figure 4.3, the background events unrelated both the neutrons and time are removed with this subtraction; the peak structure that is seen before subtraction is an event caused by gamma rays coming from the SFC, because neutrons do not pass through the $^{6}$LiF shutter, while gamma rays pass through the $^{6}$LiF shutter. Therefore, this peak structure can be seen whether the $^{6}$LiF shutter is open or not. In addition, in order to reduce the number of background events occurring while neutrons are present in the TPC, we define the sideband region and fiducial region, and subtract these two regions. A conceptual view for determining the fiducial region is shown in Figure 4.4.

As can be seen in Figure 4.4, we defined the fiducial region as when a neutron beam bunch is present between the Z-position of the TPC from $-38$ cm to 38 cm. This is to ensure that the neutron bunches are completely contained in the TPC so that the number of background events due to neutron interactions with the beam duct or other materials can be reduced as much as

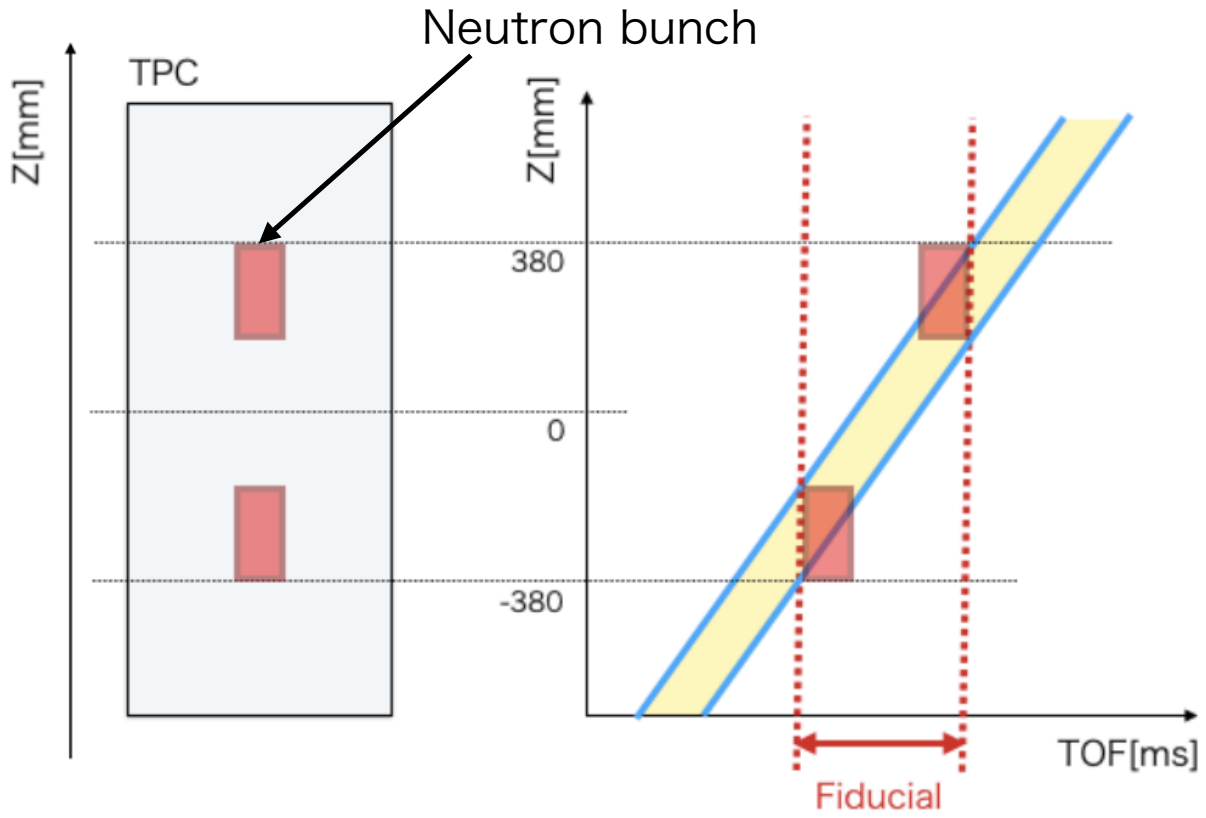


Figure 4.4: Conceptual view for determining the fiducial region. The fiducial region is defined as when neutron beam bunch is present between the Z-position of TPC from −38 cm to 38 cm. This is to ensure that the neutron bunches are completely contained in the TPC.

possible. The Z-position of the TPC was measured from the hit information of the cathode wire, and the fiducial region was determined by combining this position information and the TOF information. The two-dimensional distribution of the TOF and cathode hit information from the acquired data is shown in Figure 4.5. In Figure 4.5, the vertical axis shows the Z-position of the neutron bunch, and the horizontal axis shows its TOF. Clear peak structures are seen along with the neutron bunch passing through the TPC. Since the slope of this two-dimensional distribution depends on the neutron velocity, it changes as it goes to larger TOF regions. Therefore, the last bunch has the longest fiducial region.

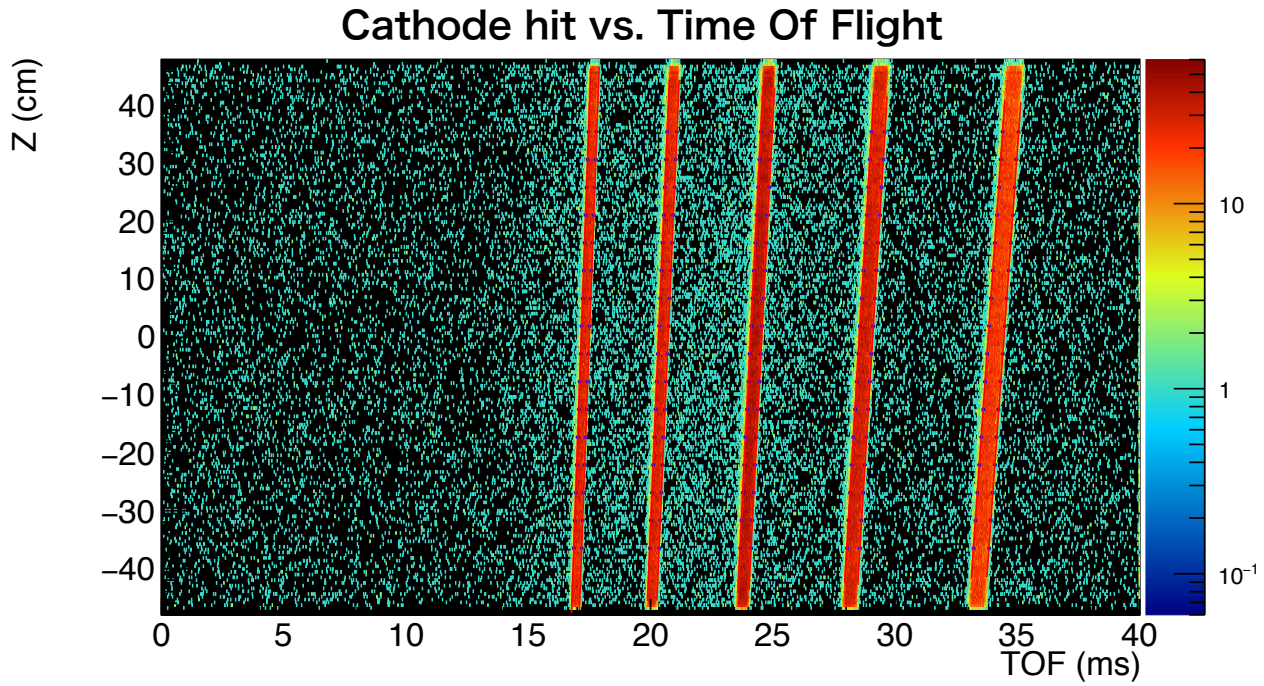


Figure 4.5: Two-dimensional distribution of the TOF and cathode hit information. The vertical axis shows the Z-position of the neutron bunch, and the horizontal axis shows the TOF of the neutron bunch. Clear peak structures are seen as the neutron bunch passes through the TPC.

The sideband region is defined as the region where the neutrons are not present in the TPC. We set the sideband region to be from 4 ms to 10 ms of the TOF. The sideband and fiducial region are shown in Figure 4.6. After determining the fiducial and sideband region, each number of events is normalized according to the ratio of the TOF durations of each region. There are time-independent background events in these two regions, and neutron-induced events can be extracted by subtracting these two regions.

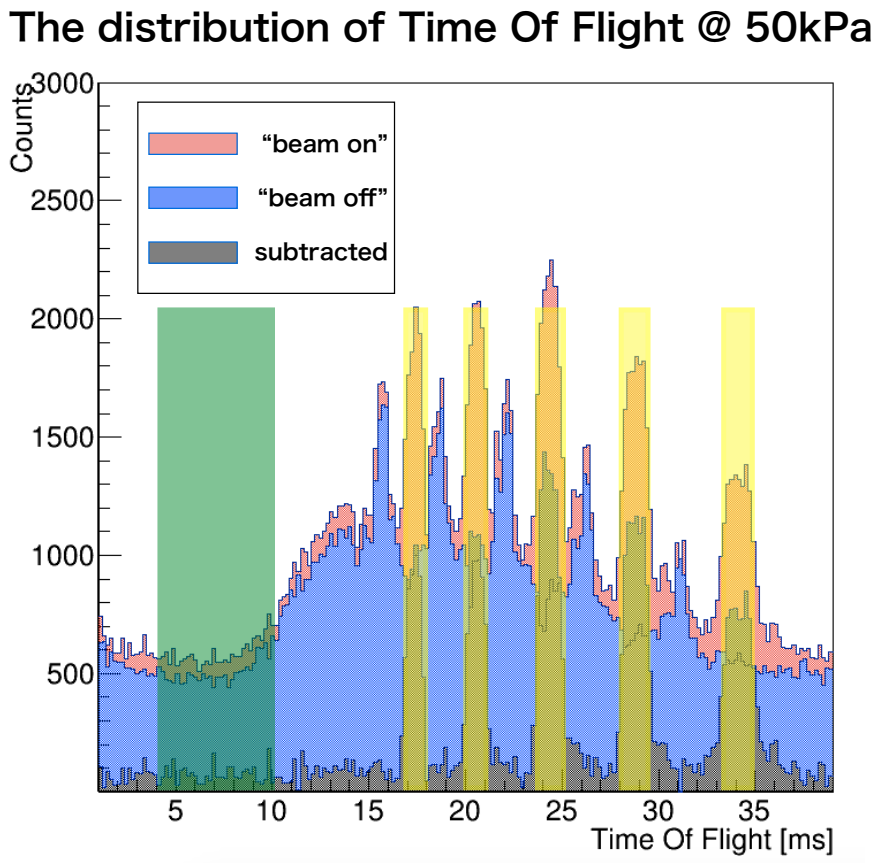


Figure 4.6: TOF distribution with the fiducial and sideband regions shown. The yellow boxes show the fiducial region and the green box shows the sideband region. The normalization is done with the ratio of time durations of each region.

In this way, the background events in Category A, such as the environmental background and gamma rays from upstream material, can be eliminated.

### 4.3.2 Background study for Category B

The background events that cannot be removed by the TOF analysis, classified into Category B, are eliminated by event selection. These events include the background events caused by neutrons and the accidental contamination of cosmic rays. For the event selection, we use information on the drift length in the TPC, information on end point of a track of a charged particle, and information on deposit energy by a charged particle. We will describe the three variables for the event selection.

### Drift length

In order to exclude the events where a charged track penetrates the TPC vertically, such as an event due to cosmic rays, we use the variable called the drift length. This is a variable calculated from the drift velocity and the time difference between the time information of the first trigger and that of the last trigger. This variable corresponds to the track length in the vertical direction of the TPC. An example of the drift lengths of the cosmic ray background and a neutron $\beta$ decay signal is shown in Figure 4.7.

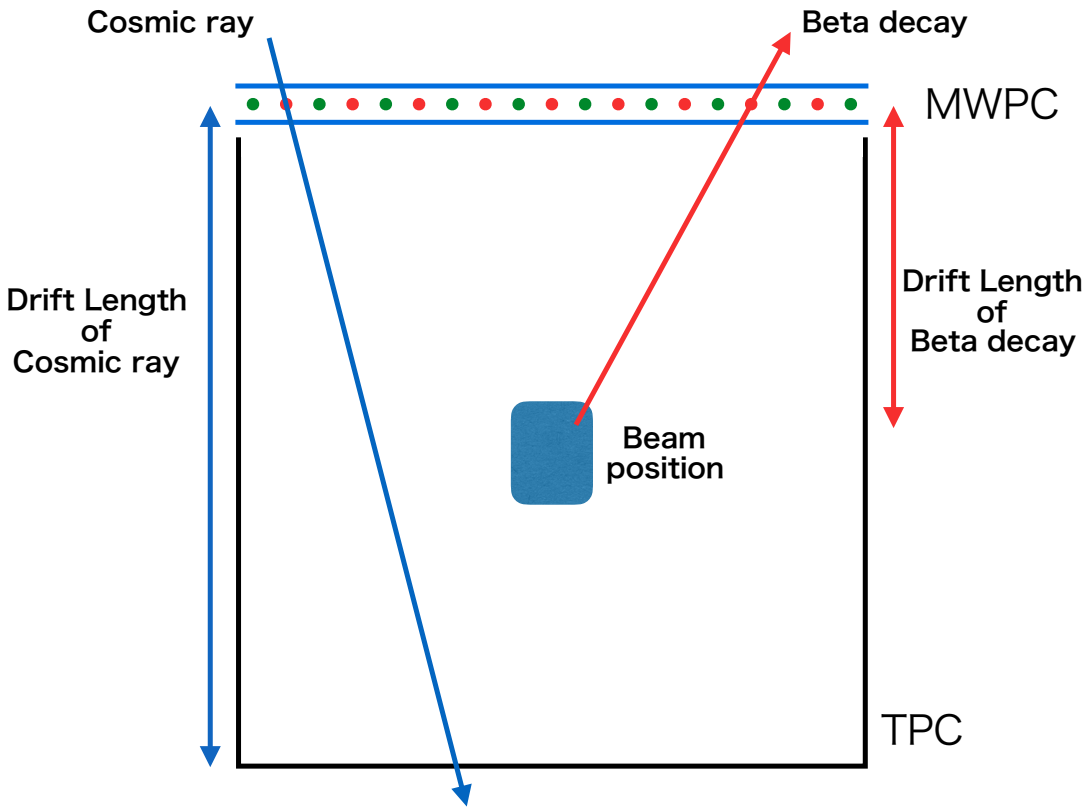


Figure 4.7: Example of the drift lengths of the cosmic ray background and a $\beta$ decay signal. Since the cosmic ray event background event has a long vertical track in the TPC, it can be separated from the $\beta$ decay event by using the track length along the vertical direction.

Since events such as cosmic rays are distributed over large values of the drift length, we excluded events with large drift lengths as background events. Figure 4.8 shows the distribution of the drift length from experimental data and Monte Carlo simulations.

In Figure 4.8, the black dots represent experimental data and the red histogram represents the results of Monte Carlo simulations. The peak structure around the drift length of 13 cm is because of the events due to neutron $\beta$ decay that have the endpoints on the beam axis. The drift length therefore corresponds to the distance from the beam axis to the MWPC. Events

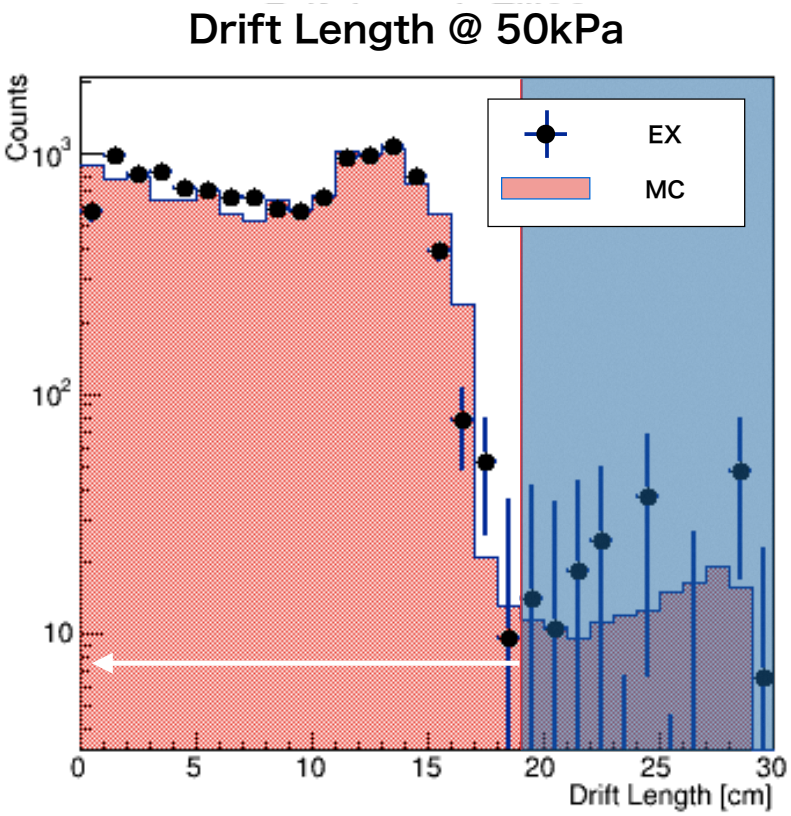


Figure 4.8: Distribution of the drift length. The black dots are experimental data, and the red histogram is the result of Monte Carlo simulations. The number of events is normalized with the statistics of the experimental data. We excluded events with a drift length larger than 19 cm as background events.

whose drift lengths are shorter than 13 cm are the events where the track passes through the TPC at a shallow angle. In this analysis, we excluded events with drift lengths larger than 19 cm as background events.

### Distance from Center

The other variable for eliminating the background events is called the Distance from Center (DC). This variable is calculated with the endpoint of a charged track that is the closest to the center of the beam axis. A conceptual picture of the DC is shown in Figure 4.9. The $\beta$ decay event has an end point on the beam axis; however, the background event caused by the scattered neutron has an endpoint outside of the beam axis.

The gamma rays caused by the scattered neutron mainly produce a background event due to Compton scattering on the TPC wall. Therefore, we defined a DC value in order to exclude this kind of background event.

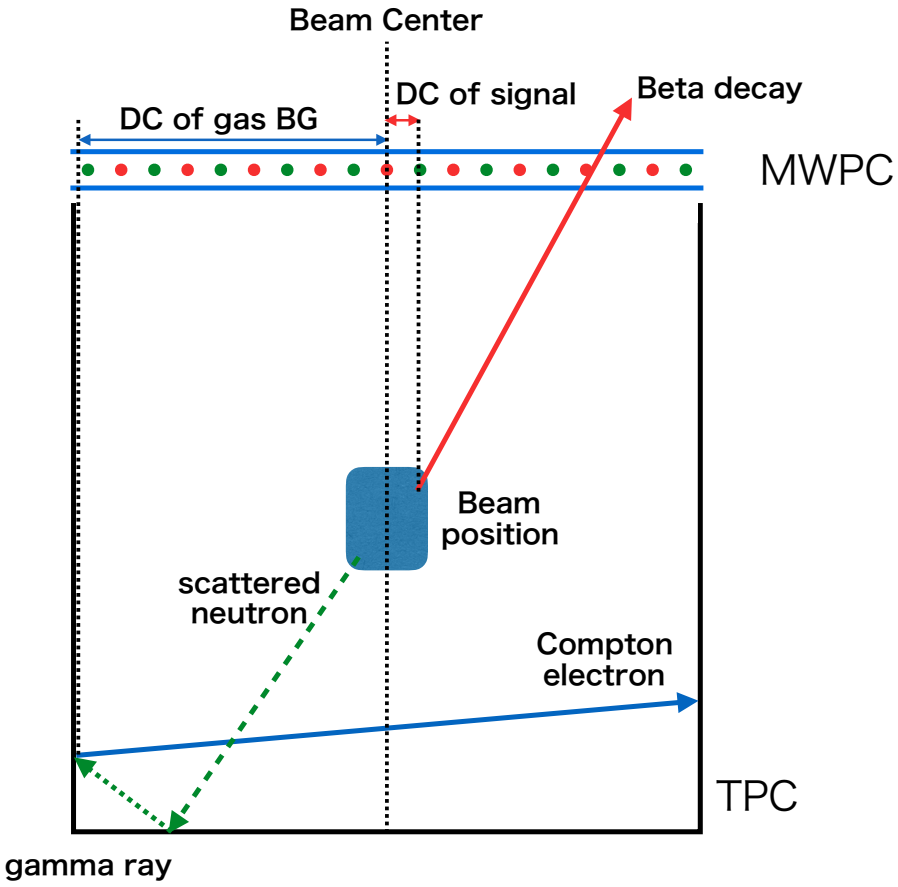


Figure 4.9: Conceptual picture of the DC. The DC is determined by the position of the endpoint that is the nearest to the beam center. The neutron $\beta$ decay event has an end point on the beam axis; however, the background event caused by the scattered neutron has an endpoint away from the beam axis.

In Figure 4.10, the black dots represent experimental data, the red histogram shows the Monte Carlo simulation of the neutron $\beta$ decay, the green histogram shows the Monte Carlo simulation of background events caused by scattered neutrons, and the blue histogram represents the Monte Carlo simulation of off-axis neutron $\beta$ decay. As shown in Figure 4.10, the events due to $\beta$ decay are localized within a small value of the DC; however, the events caused by scattered neutrons are uniformly distributed in the DC. Therefore, we set the cutoff position to DC=4 to improve the signal-to-noise ratio. The estimation of the number of background events remaining after this cut is described in Section 4.3.3.

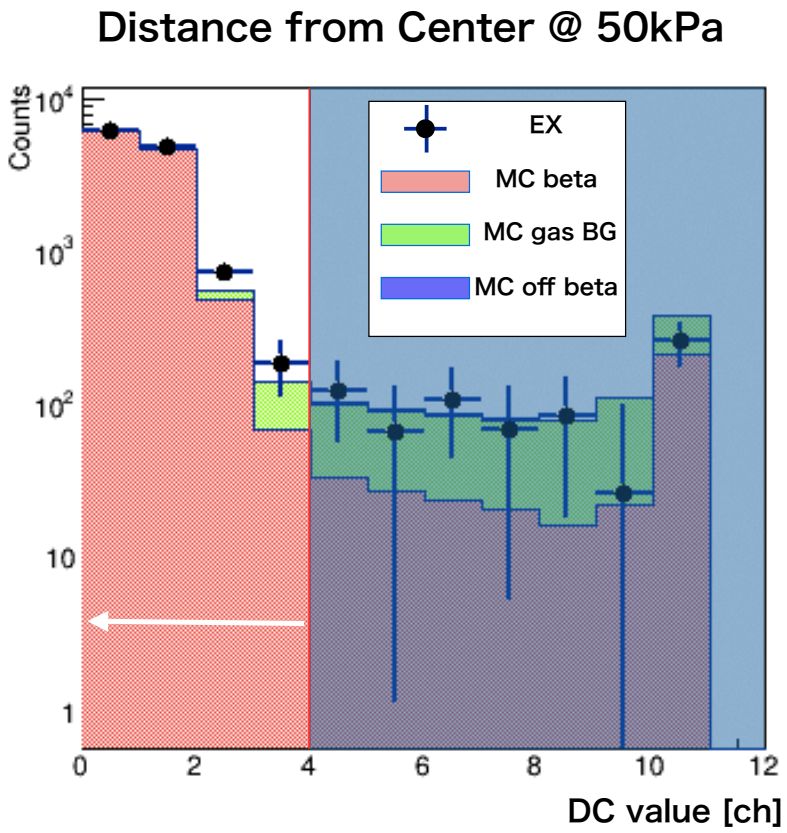


Figure 4.10: Distribution of the DC. tThe black dots represent experimental data, the red histogram represents the Monte Carlo simulation of the neutron $\beta$ decay, the green histogram represents the Monte Carlo simulation of background events caused by scattered neutrons, and the blue histogram represents the Monte Carlo simulation of off-axis neutron $\beta$ decay.

### Deposit energy

In order to further reduce the number of background events, we use deposit energy in the TPC in addition to the position information from the drift length and the DC. This event selection is effective especially for the Category B background events because their deposit energies in the TPC are significantly different from to those of neutron $\beta$ decay. The typical deposit energy of background events caused by neutron absorption by $CO_2$ gas is about 1 keV. The distribution of the deposit energy is shown in Figure 4.11.

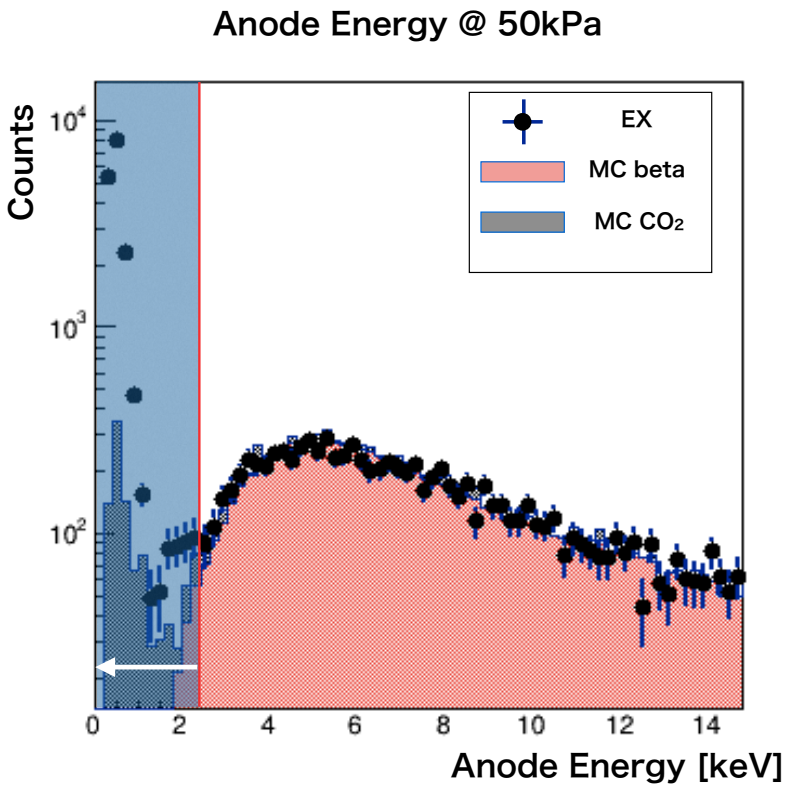


Figure 4.11: Distribution of the deposit energy in the TPC. The black dots represent experimental data, the red histogram represents the Monte Carlo simulation of neutron $\beta$ decay, and the gray histogram represents the Monte Carlo simulation of background events caused by neutron absorption by $CO_2$.

In Figure 4.11, the black dots represent experimental data, the red histogram shows the Monte Carlo simulation of neutron $\beta$ decay, and the gray histogram shows the Monte Carlo simulation of background events caused by neutron absorption by $CO_2$. We set the cutoff position to 2.5 keV. There is a disagreement between the data and simulations in the low energy region. This is caused by background events other than $CO_2$ absorption such as electrical noise, which is not considered in our simulation; however, since the cutoff position is set to be sufficiently larger ($8\sigma$ away from the background peak) than these events, leakage of these background events into the signal region is considered to be negligible.

### 4.3.3 Background study for Category C

After the TOF analysis and event selection described in Section 4.3.1 and Section 4.3.2, the number of remaining background events was estimated using Monte Carlo simulations, and was subtracted from the number of signal candidates. The normalization of the data and Monte Carlo simulations was carried out using a control region where only background events exist. In order to perform this normalization, we introduced a variable called the $x$-value. A conceptual picture of the $x$-value is shown in Figure 4.12. In this variable, the nearest wire from the beam center represents the $x$-value. The $x$-value is determined by the position closest to the beam axis among the anode hits in the TPC. Since a neutron $\beta$ decay event has a track that comes from the beam axis, events from neutron $\beta$ decay are distributed in the small $x$-value region. The distribution of the $x$-value is shown in Figure 4.13. The black dots represent experimental data, the red histogram represents the Monte Carlo simulation of neutron $\beta$ decay, the green histogram represents the Monte Carlo simulation of background events caused by scattered neutrons, and the blue histogram represents the Monte Carlo simulation of off-axis neutron $\beta$ decay. $x$-values larger than 4 are defined as the control region for the normalization.

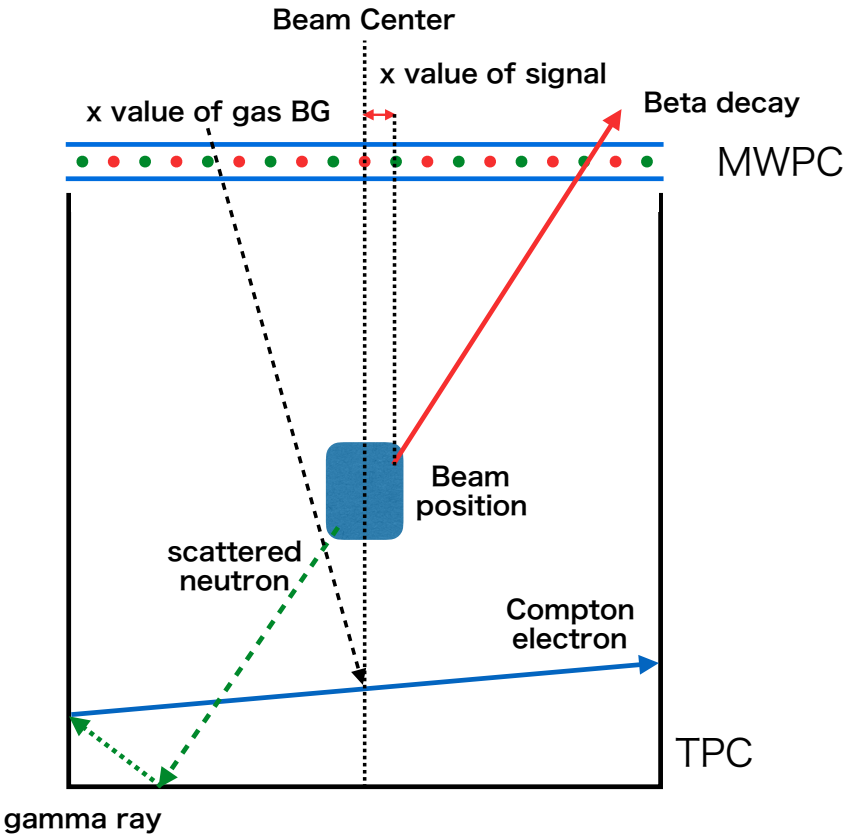


Figure 4.12: Conceptual picture of the $x$-value. The nearest wire to the beam center represents the $x$-value.

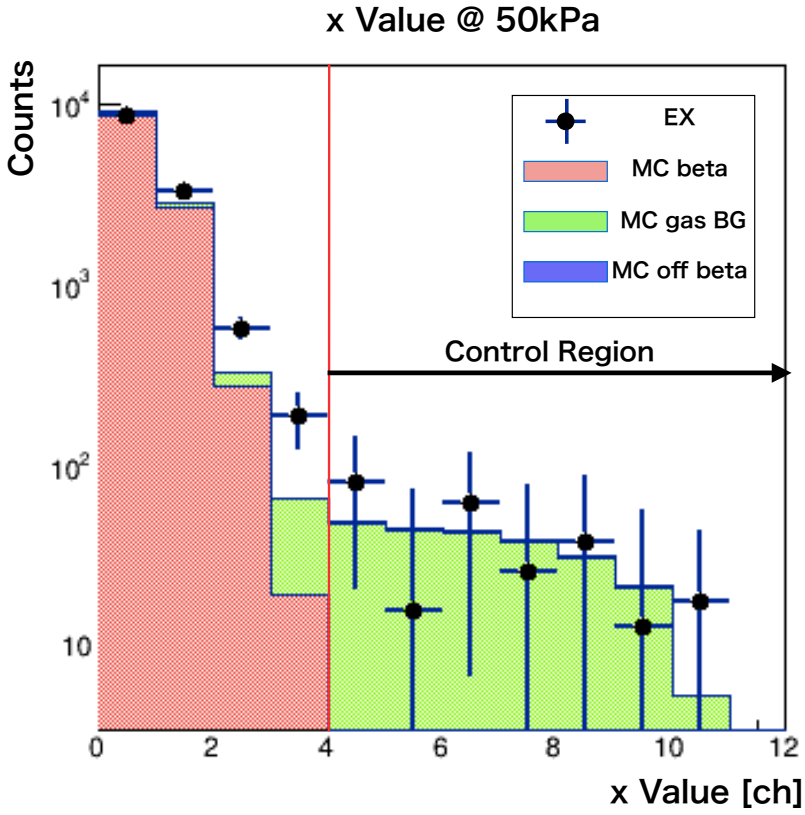


Figure 4.13: Distribution of $x$-values. The black dots represent experimental data, the red histogram represents the Monte Carlo simulation of neutron $\beta$ decay, the green histogram represents the Monte Carlo simulation of background events caused by scattered neutrons, and the blue histogram represents the Monte Carlo simulation of off-axis neutron $\beta$ decay. $x$-values larger than 4 are the control region for normalization.

As we can see in Figure 4.13, there are only background events in regions with large $x$-values. Therefore, we normalized the number of data and the number of Monte Carlo simulations in this control region. The number of remaining background events in DC<4 was estimated with Monte Carlo simulations using this normalization factor. The estimated number of events is summarized in Table 4.3.

### 4.3.4 Signal estimation

After all the background reduction, we separated the neutron $\beta$ decay candidates from neutron absorption by $^3$He candidates in order to determine the numbers of both candidates. The separation of these two events was carried out using the deposit energy in the TPC. The deposit energy of neutron absorption by $^3$He is large and causes saturation when it is detected. Therefore, in order to distinguish the neutron $\beta$ decay from the neutron absorption by $^3$He, the deposit energy onto the field wires is used instead of that onto the anode wires. The distribution of the deposit energy on the field wire is shown in Figure 4.14. After event separation and

| Source of background | Number of events |
|---|---|
| Gamma rays by scattered neutrons | 262 events |
| Off-axis $\beta$ decay | 14 events |

Table 4.3: Number of background events estimated by Monte Carlo simulations.

background reduction, we finally obtained the numbers of each type of candidate, as shown in Table 4.4.

| | Number of events |
|---|---|
| $N_\beta$ | 11851 events |
| $N_{^3\mathrm{He}}$ | 279781 events |

Table 4.4: Numbers of signal candidates.

In Figure 4.14, the black dots represent experimental data, the red histogram represents the Monte Carlo simulation of neutron $\beta$ decay, and the blue histogram represents the Monte Carlo simulation of neutron absorption by $^3$He. We set a cutoff position at 20 keV of deposit energy onto the field wire. The peak around 30 keV is due to the fact that the simulation of neutron absorption by $^3$He is not fully optimized yet. However, since the number of contaminating $^3$He events in the $\beta$ decay region was less than $10^{-3}$ events, and the contamination of $\beta$ candidates in the $^3$He region is also less than 0.1% of the number of $^3$He candidates, this peak between 20 keV and 40 keV is negligible.

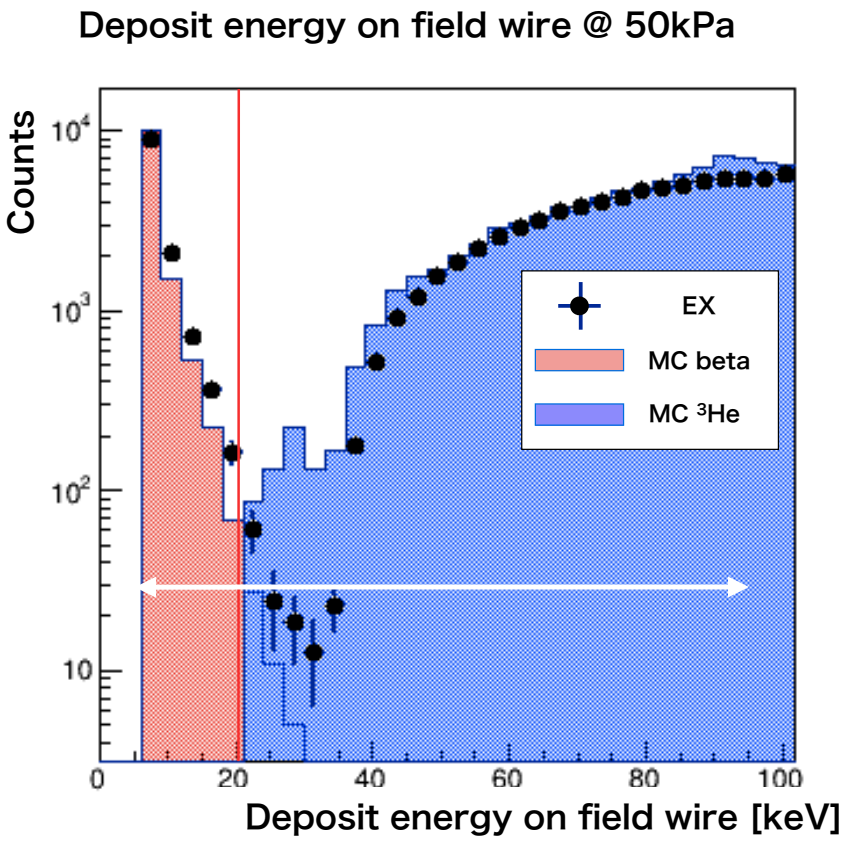


Figure 4.14: Distribution of the deposit energy onto the field wire. The black dots represent experimental data, the red histogram represents the Monte Carlo simulation of neutron $\beta$ decay, and the blue histogram represents the Monte Carlo simulation of neutron absorption by $^3$He.

## 4.4 Efficiency

The efficiencies for calculating the neutron lifetime were determined using Monte Carlo simulations.

### 4.4.1 Efficiency for neutron $\beta$ decay

The efficiency for neutron $\beta$ decay for each cut is shown in Table 4.5.

| Cut | Efficiency |
|---|---|
| Drift length | 98.9 % |
| DC | 96.9 % |
| Deposit energy (anode) | 98.5 % |
| Deposit energy (field) | 99.5 % |
| All cut | 92.9 % |

Table 4.5: Efficiencies for neutron $\beta$ decay for each cut.

The cut from the DC has the worst efficiency in this analysis, and the loss of events due to this cut is about 3%. The efficiency of the neutron $\beta$ decay after applying all the cuts was 92.9%.

### 4.4.2 Efficiency for the neutron absorption by $^3$He

The efficiency for neutron absorption by $^3$He was determined by the field wire deposit energy, since it is the only variable to select for neutron absorption by $^3$He. The efficiency for the cut is shown in Table 4.6.

| Cut | Efficiency |
|---|---|
| Deposit energy (field) | 99.9 % |

Table 4.6: Efficiencies for neutron absorption by $^3$He.

## 4.5 Determination of the number density of $^3$He

As described in Section 2.2, we used the volume expansion method to determine the number density of $^3$He. Since we used $^4$He as the operating gas of the TPC, the contamination of $^3$He in the G1 Helium bottle is unavoidable. Therefore, correction for $^3$He from the G1 Helium is necessary. This correction value was estimated using a mass spectrometer. The measurement using mass spectrometer was carried out at the Komaba Campus of the University of Tokyo. A photograph of the mass spectrometer is shown in Figure 4.15. The mass spectrometer has a double collector system, and it can determine the ratio of $^3$He/$^4$He with a precision of $\pm$10%. Using this system, we measured the ratio of $^3$He/$^4$He in the operating gas, and corrected it with the result from the mass spectrometer.

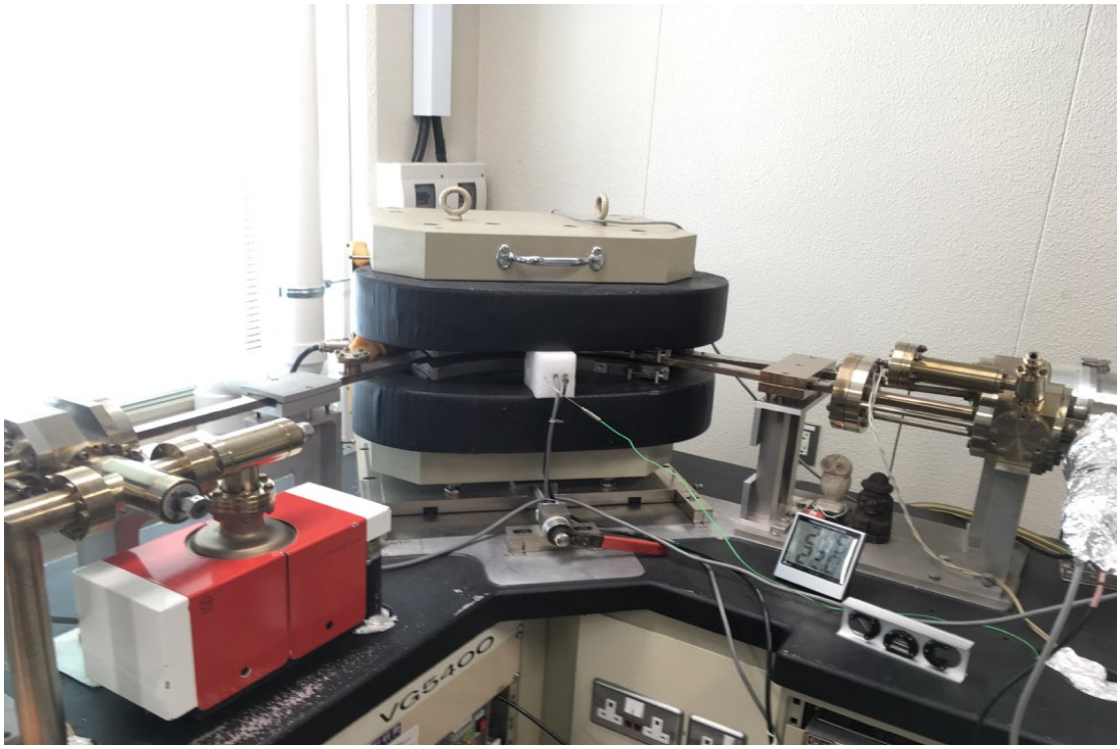


Figure 4.15: Photograph of the mass spectrometer at the Komaba Campus of the University of Tokyo [37].

After correction, we finally obtained the number of density of $^3$He to be

$$(2.039 \pm 0.018) \times 10^{19} \text{ atom/m}^3.$$

## 4.6 Uncertainty

Before the calculation of the neutron lifetime, we will discuss the estimation of uncertainties in this section.

### 4.6.1 Statistical uncertainty

First of all, we consider the statistical uncertainty. Statistical uncertainties for the numbers of candidates of the neutron $\beta$ decay and the neutron absorption by $^3$He were determined by the statistics of the experimental data, and the statistical uncertainty of the efficiency was derived from the statistics of the Monte Carlo simulations and the uncertainty of the scale factor between the experimental data and Monte Carlo simulations. The statistical uncertainties were 1.8% for $N_\beta$, 0.19% for $N_{^3\text{He}}$, and the statistical uncertainties on efficiencies were 0.09% and 0.01% for the efficiencies for neutron $\beta$ decay and neutron absorption by $^3$He, respectively.

### 4.6.2 Systematic uncertainty

Systematic uncertainties on the neutron lifetime were estimated for the following items.

(a) Subtraction of the background caused by scattered neutrons.

(b) Contrast of beam on/off for the SFC.

(c) Pile-up events.

(d) Contamination of $^{14}$N and $^{17}$O.

(e) Efficiency determination.

(f) Chamber deformation by pressure and temperature.

(g) Heat generation from the amplifier.

Uncertainties from (a) to (c) and (e) were estimated with Monte Carlo simulations, the uncertainty from (d) was estimated by the data from low voltage operations. The uncertainty from (f) was measured by using a vacuum chamber and that from (g) was calculated with the temperature difference between the upper and lower sides of the TPC.

#### (a) Subtraction of the background caused by scattered neutrons

Uncertainty due to the subtraction of background events is mainly due to the scale factor between the experimental data and Monte Carlo simulations. For neutron absorption reaction events by $^3$He, we defined the foreground and background regions with the FCE variable as

$$\begin{aligned} \text{Foreground} &: 5 \leq \text{FCE} \leq 18 \\ \text{Background} &: \text{FCE} < 5 \text{ or } 18 < \text{FCE}. \end{aligned}$$

If we express these regions by using subscripts of f and b, respectively, the number of events after subtraction, $N_{\text{sub(f+b)}}$, is represented as follows using the number of events of the experimental data $N_{\text{ex(f+b)}}$, of the Monte Carlo simulations $N_{\text{MC(f+b)}}$, and their statistical uncertainties $\delta N_{\text{ex(f+b)}}$, $\delta N_{\text{MC(f+b)}}$,

$$N_{\text{sub(f+b)}} = (N_{\text{ex(f+b)}} \pm \delta N_{\text{ex(f+b)}}) - C(N_{\text{MC(f+b)}} \pm \delta N_{\text{MC(f+b)}}) \tag{4.4}$$

where $C$ is the scale factor between the experimental data and the Monte Carlo simulations. Here, the uncertainty due to the scale factor $\delta C$ can be written as

$$C \equiv \frac{N_{\text{ex(b)}}}{N_{\text{MC(b)}}} \tag{4.5}$$

$$\begin{aligned} (\delta C)^2 &= (\frac{\partial C}{\partial N_{\text{ex(b)}}})^2 (\delta N_{\text{ex(b)}})^2 + (\frac{\partial C}{\partial N_{\text{MC(b)}}})^2 (\delta N_{\text{MC(b)}})^2 \\ &= \{(\frac{\delta N_{\text{ex(b)}}}{N_{\text{MC(b)}}})^2 + (\frac{-N_{\text{ex(b)}} \times \delta N_{\text{MC(b)}}}{N_{\text{MC(b)}}^2})^2\} \\ &= \frac{1}{N_{\text{MC(b)}}^2}\{(\delta N_{\text{ex(b)}})^2 + C^2 (\delta N_{\text{MC(b)}})^2\} \end{aligned} \tag{4.6}$$

Thus, the uncertainty on the subtracted events $\delta N_{\rm sub}$ is obtained to be

$$
\begin{aligned}
(\delta N_{\rm sub(f+b)})^2 &= (\frac{\partial N_{\rm sub(f+b)}}{\partial N_{\rm ex(f)}})^2(\delta N_{\rm ex(f)})^2 + (\frac{\partial N_{\rm sub(f+b)}}{\partial N_{\rm MC(f)}})^2(\delta N_{MC(f)})^2 \qquad (4.7)\\
&\quad +(\frac{\partial N_{\rm sub(f+b)}}{\partial N_{\rm ex(b)}})^2(\delta N_{\rm ex(b)})^2 + (\frac{\partial N_{\rm sub(f+b)}}{N_{\rm MC(b)}})^2(\delta N_{\rm MC(b)})^2 \\
&= (\delta N_{\rm ex(f)})^2 + C^2(\delta N_{\rm MC(f)})^2 + N^2_{\rm MC(f)}(\delta C)^2. \qquad (4.8)
\end{aligned}
$$

As shown in Equation (4.8), the uncertainty due to the scale factor plays an important role in the uncertainty in the number of events after subtraction. This uncertainty was 0.01% for $N_{^3\rm He}$ candidates. For the events of neutron $\beta$ decay, we defined three regions with the variables DC and $x$,

$$
\begin{aligned}
1. &: x \leq 3 \ \&\& \ {\rm DC} \leq 3\\
2. &: x \leq 3 \ \&\& \ {\rm DC} > 3\\
3. &: x > 3
\end{aligned}
$$

If we express these regions using subscripts 1, 2, and 3, respectively, the uncertainty in the number of events after subtraction $N_{\beta\rm sub}$ is represented as follows using the number of events of the experimental data $N_{\rm ex}$, Monte Carlo simulations of off-axis beta decay $N_{\rm MCoff}$, Monte Carlo simulations of gamma rays caused by scattered neutrons $N_{{\rm MC}\gamma}$, and their statistical uncertainties $\delta N_{\rm ex}$, $\delta N_{\rm MCoff}$ and $\delta N_{{\rm MC}\gamma}$:

$$
\begin{aligned}
(\delta N_{\beta\rm sub})^2 &= \sum_{i=1,2,3}(\frac{\partial N_{\beta\rm sub}}{\partial N_{\rm ex}})^2(\delta N_{\rm ex})^2 \\
&\quad + \sum_{i=1,2,3}(\frac{\partial N_{\beta\rm sub}}{\partial N_{\rm MCoff}})^2(\delta N_{\rm MCoff})^2 + \sum_{i=1,2,3}(\frac{\partial N_{\beta\rm sub}}{\partial N_{{\rm MC}\gamma}})^2(\delta N_{{\rm MC}\gamma})^2. \qquad (4.9)
\end{aligned}
$$

Following this formula, we obtained a 0.15% systematic uncertainty on the $N_\beta$ candidates.

### (b) Contrast of beam on/off of the SFC

There is a possibility that neutron capture by a $^3$He event near the entrance of the TPC leaks into the neutron $\beta$ decay candidates. In order to estimate this effect, we simulated neutron absorption by $^3$He near the TPC entrance, and estimated the number of events. In this estimation, we assumed $\pm$ 50 mm from the TPC edge region as an entrance of the TPC, and the length of the neutron bunch as 400 mm. Thus, we can estimate the ratio of the neutron absorption by $^3$He, $R_{^3\rm He}$, as

$$
R_{^3\rm He} = 200 \times \frac{1}{400} \times \frac{1}{400} \times \epsilon_{\rm leak}. \qquad (4.10)
$$

The $\epsilon_{\rm leak}$ represents the detection efficiency of neutron absorption reactions by $^3$He near the TPC entrance. The total estimated number of events was added as a systematic uncertainty on the $N_\beta$ and $N_{^3\rm He}$ candidates. The effect of this uncertainty was determined to be 0.29%.

### (c) Pile-up events

Since the time window of a single event is 100 $\mu$sec, sometimes we obtain multiple events within a single trigger. Depending on the type of events that make up trigger, the pile-up events are classified into five categories:

1. Triggered by a neutron $\beta$ decay and followed by a high energy event, including neutron absorption by $^3$He.

2. Triggered by a low energy background and followed by a low energy event, including neutron $\beta$ decay.

3. Triggered by a high energy background and followed by a high energy event, including neutron absorption by $^3$He.

4. Triggered by a high energy background and followed by a low energy event, including neutron $\beta$ decay.

5. Triggered by a low energy event including neutron $\beta$ decay and followed by a high energy event, including neutron absorption by $^3$He.

The correction of Type 1 pile-up reduces $N_\beta$ candidates, and that of Type 2 increases $N_\beta$ candidates. The pile-ups of Type 3 to 5 reduce $N_{^3\mathrm{He}}$. The effect of the pile-up events was calculated by rate of each event, the time window after the trigger (70 $\mu$sec), and the fiducial region, which is calculated by TOF analysis, and it was estimated to be 0.20% for $N_\beta$ and 0.05% for $N_{^3\mathrm{He}}$.

### (d) Contamination of $^{14}$N and $^{17}$O

Contamination of $^{14}$N and $^{17}$O affects the $N_{^3\mathrm{He}}$ candidates. In order to estimate this effect, we used the low voltage operation described in Section 4.1. The distribution of the deposit energy of each event in the TPC is shown in Figure 4.16. A neutron absorption reaction caused by $^{14}$N has a deposit energy of 626 keV in the TPC. Since this deposit energy is quite close to that caused by $^3$He (764 keV), the number of events caused by $^{14}$N is calculated by fitting the histogram of deposit energy with double-Gaussian, as shown in Figure 4.16. Neutron absorption reaction by $^{17}$O has a deposit energy of 1844 keV, and this is about twice that caused by $^3$He. Therefore, the right-side histogram shown in Figure 4.16 contains the neutron absorption reaction by $^{17}$O and pile-up of two neutron absorption reactions by $^3$He. Thus, we calculated the contamination of $^{17}$O using the natural abundance of $^{17}$O in $CO_2$ and its neutron absorption cross section (0.236 barn). The calculated values are summarized in Table 4.7.

| Nucleus | Number of contaminations | Uncertainty |
|---|---|---|
| $^{14}$N | 941 events | 0.07% |
| $^{17}$O | 768 events | 0.02% |

Table 4.7: Contamination of $^{14}$N and $^{17}$O.

As shown in Table 4.7, the uncertainty in $N_{^3\mathrm{He}}$ was 0.07% and 0.02%, respectively.

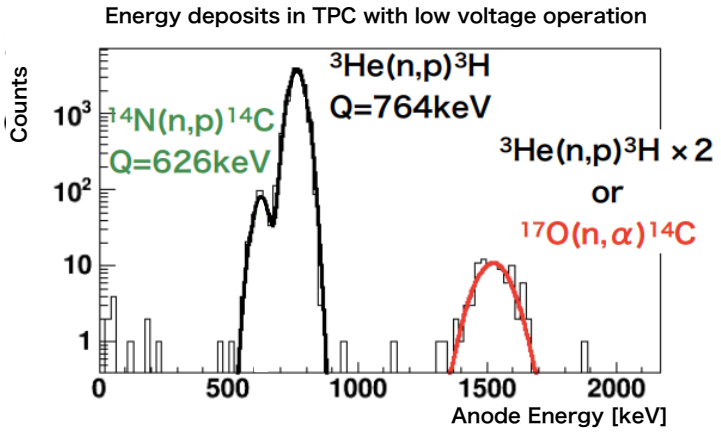


Figure 4.16: Distribution of the deposit energy in the low voltage operation. The number of events caused by $^{17}$O was estimated from the ratio to the $^{3}$He pile-up events.

### (e) Efficiency determination

Uncertainty due to the efficiency determination was calculated using Monte Carlo simulations. For all cuts except for the DC value, we used the ambiguity in the energy calibration of the Monte Carlo simulations to calculate the uncertainty from each cut. By comparing the deposit energy of cosmic rays with simulations and experimental data, we calculated the uncertainty in the efficiency by changing the cut position by as much as the energy difference. We changed the cut position by 16.8%. The uncertainty in the DC value was estimated by changing the beam position of the Monte Carlo simulations by ±2 cm. The uncertainties in the efficiency estimated by changing the energy and beam position are summarized in Table 4.8 and Table 4.9.

| Cut | Uncertainty |
|---|---|
| Drift length | 0.1% |
| Deposit energy (anode) | 1.4% |
| Deposit energy (field) | 0.9% |
| DC | 0.6% |
| All cuts | 1.8% |

Table 4.8: Uncertainties in the cut efficiencies for neutron $\beta$ decay candidates.

For neutron $\beta$ decay candidates, we considered the uncertainties for all of the cut variables. However, for neutron absorption reactions by $^{3}$He, since the deposit energy onto the field wire is the only variable to affect its efficiency, we only took into account this effect. The uncertainty in the efficiency is 1.8% for the neutron $\beta$ decay candidates, and 0.02% for neutron absorption reaction by $^{3}$He.

| Cut | Uncertainty |
|---|---|
| Deposit energy (field) | 0.02% |

Table 4.9: Uncertainty in the cut efficiency for neutron absorption by $^3$He candidates.

### (f) Chamber deformation by pressure and temperature

Uncertainty due to chamber deformation was calculated by measuring the pressure and temperature before and after the experiment. This uncertainty affects the number density of $^3$He, and it was estimated to be 0.80%.

### (g) Heat generation from the amplifier

Heat generation from the amplifier causes non-uniformity of the $^3$He gas and it affects the stability of the count rate for the events from neutron absorption by $^3$He. This effect was estimated using the temperature difference between the upper and lower sides of the TPC. If there is a temperature difference between the upper and lower sides of the TPC, the operating gas, which is warmed near the upper side of the TPC, is moved to the lower side of the TPC. This difference was 14 K in the experiment at 50 kPa. The uncertainty due to this effect was calculated to be $5.5 \times 10^{-3}$. Therefore, we set this uncertainty to be 0.06% for the number density of $^3$He.

| | $N_\beta$ | $N_{^3\mathrm{He}}$ | $\epsilon_\beta$ | $\epsilon_{^3\mathrm{He}}$ | $\rho$ |
|---|---|---|---|---|---|
| (a)Subtraction of background | 0.15% | 0.01% | — | — | — |
| (b)Contrast of beam on/off of the SFC | 0.29% | 0.29% | — | — | — |
| (c)Pile-up events | 0.20% | 0.05% | — | — | — |
| (d)Contamination of $^{14}$N and $^{17}$O | — | 0.07% | — | — | — |
| (e)Efficiency determination | — | — | 1.8% | 0.02% | — |
| (f)Chamber deformation | — | — | — | — | 0.80% |
| (g)Heat generation from the amplifier | — | — | — | — | 0.06% |

Table 4.10: Summary of uncertainties.

A summary of systematic uncertainties is shown in Table 4.10. Currently, the largest uncertainty is due to the detection efficiency. The numbers of events obtained through each analysis procedure are shown in Table 4.11 and Table 4.12

| | Value | Correction | Uncertainty |
|---|---|---|---|
| $S_\beta$ before correction | 12162 | 0 | $\pm$ 194(stat.) |
| Background from gamma rays | 11900 | $-262$ | $\pm$ 16 |
| Background from off-axis $\beta$ decay | 11886 | $-14$ | $\pm$ 4 |
| Spectrum of gamma rays from LiF | 11886 | 0 | $\pm$ 7 |
| Gamma rays from upstream | 11886 | 0 | $\pm$ 85(stat.) |
| SFC contrast | 11851 | $-35$ | +35 / 0 |
| $CO_2$ recoil | 11851 | 0 | +0 / $-17$ |
| $^3$He event contamination | 11851 | 0 | $\pm$ 0 |
| Pile-up | 11869 | +18 | +6 / $-24$ |
| $S_\beta$ corrected ($N_\beta$) | 11869 | | $\pm$ 212(stat.) $^{+40}_{-35}$(sys.) |

Table 4.11: Corrections and uncertainties for each analysis procedure for $\beta$ decay events.

| | Value | Correction | Uncertainty |
|---|---|---|---|
| $S_{^3He}$ before correction | 282206 | 0 | $\pm$ 534(stat.) |
| Background from off-axis neutron capture | 281704 | $-502$ | $\pm$ 23 |
| $\beta$ decay event contamination | 281704 | 0 | $\pm$ 0 |
| Nitrogen contamination | 280763 | $-941$ | $\pm$ 200 |
| Oxygen contamination | 279931 | $-833$ | $\pm$ 42 |
| Pile-up | 279781 | $-150$ | +150 / 0 |
| $S_{^3He}$ corrected ($N_{^3He}$) | 279781 | | $\pm$ 534(stat.) $^{+254}_{-205}$(sys.) |

Table 4.12: Corrections and uncertainties for each analysis procedure for $^3$He events.

## 4.7 Calculation of neutron lifetime

We have finally obtained the number of events, the number density of $^3$He, the detection efficiency of each event, and their uncertainties. A summary of these values is in Table 4.13.

| | | |
|---|---|---|
| $N_\beta$ | 11869 events | Section 4.3.4 |
| $N_{^3He}$ | 279781 events | Section 4.3.4 |
| $\epsilon_\beta$ | 92.92 % | Section 4.4.1 |
| $\epsilon_{^3He}$ | 99.85 % | Section 4.4.1 |
| $\rho$ | 2.039 $\times 10^{19}$ atom/m$^3$ | Section 4.5 |
| Statistical uncertainty | 1.8 % | Section 4.6.1 |
| Systematic uncertainty | 2.1 % | Section 4.6.2 |

Table 4.13: Summary of the analysis.

By using these numbers, we calculated the neutron lifetime to be

$$\tau_n = 917 \pm 16(\text{stat.}) \pm 19(\text{sys.}) \text{ sec.} \tag{4.11}$$

This is the first result in the world from a 50 kPa operation of the electron counting method. This value is consistent with our present result from 100 kPa,

$$\tau_n = 896 \pm 10(\text{stat.})^{+14}_{-10}(\text{sys.}) \text{ sec,} \tag{4.12}$$

within the uncertainties. A summary of the neutron lifetimes from all three methods is shown in Figure 4.17. The proton counting method is shown with squares, the UCN storage method is shown with circles, and our method is shown with diamonds in Figure 4.17.

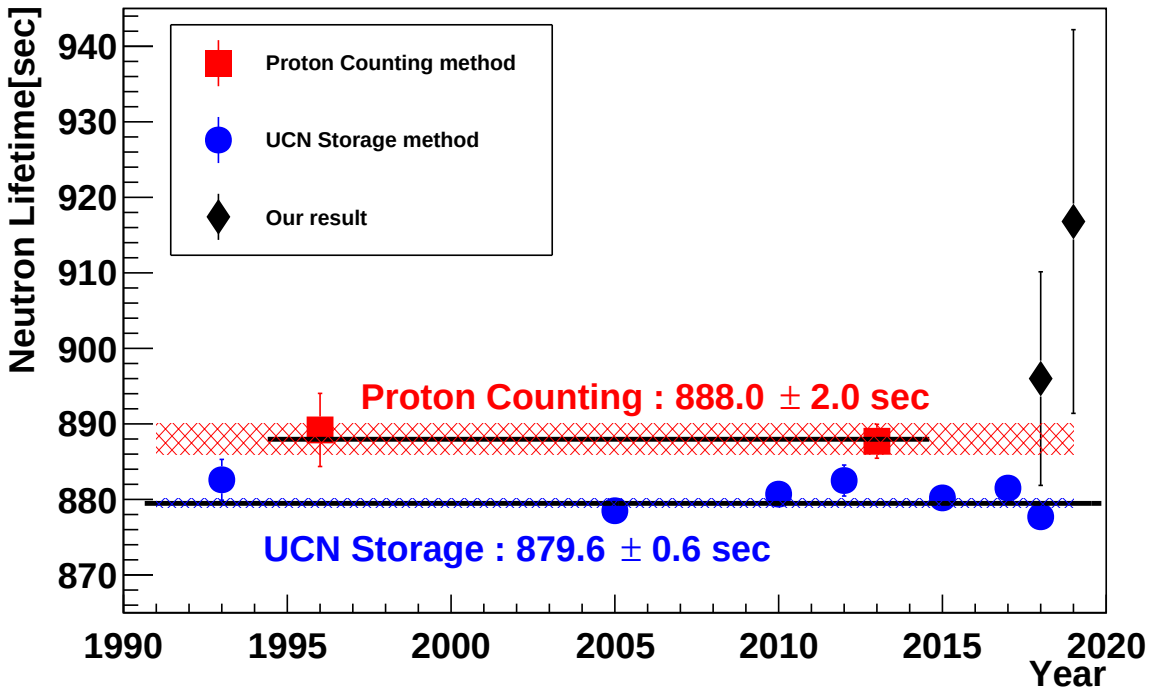


Figure 4.17: Summary of neutron lifetimes from all three methods. The proton counting method is shown with squares, and the UCN storage method is shown with circles. The statistical uncertainty for the 50 kPa operation is 1.8%, as shown with diamonds. The result from the 50 kPa operation is consistent with our present result for 100 kPa within the uncertainties.

# Chapter 5

# Conclusion and future prospects

Measurement of the neutron lifetime at 100 kPa has been conducted at J-PARC, and we have found that the background caused by scattered neutrons is considerable, which limits the accuracy of our measurement. Therefore, we considered reducing the operating gas pressure to reduce the number of background events caused by the scattered neutrons. In the operation at a low gas pressure, we found two problems; the decrease in gain of the TPC and heat generation from the amplifier. To solve these issues, we developed a new amplifier that uses ASICs and the performance from the test evaluation looks promising. The heat generation of the newly developed amplifier is less than 10 mW/ch, which corresponds to 1/50th that of the amplifier we currently use. The problem of gain decrease is overcome with additional amplifiers placed outside the vacuum chamber so as not to affect the experimental environment. Since we anticipate low gas pressure operations using this new amplifier, we carried out a physical measurement at 50 kPa. In this operation, we confirmed the number of scattered neutrons was reduced by a factor of two, as expected. This result shows that our attempt is successful, and we can therefore reduce the number of background events caused by the scattered neutrons in linear proportion to the pressure of the operating gas. For the physical measurement, we obtained the data with 1.8% statistical uncertainty with a week of data acquisition of 300 kW operation of J-PARC, and we finally obtained the neutron lifetime at 50 kPa to be

$$\tau_n = 917 \pm 16(\text{stat.}) \pm 19(\text{sys.}) \text{ sec.}$$

This is the first result in the world from a 50 kPa operation of the electron counting method. This value is consistent with our present result for 100 kPa, $\tau_n = 896 \pm 10(\text{stat.})^{+14}_{-10}(\text{sys.})$ sec, within statistical uncertainty.

We are planning several upgrades in order to improve the accuracy of our measurement. First of all, in order to improve the statistics, we plan to enlarge the neutron beam size from 3 $\times$ 3 cm$^2$ to 3 $\times$ 10 cm$^2$. We can expect a 24-times higher neutron flux from simulation. This means that we can attain 0.1% statistical uncertainty within five days of 500 kW operation of J-PARC. The second upgrade is the lower gas pressure operation of the TPC. As presented in this thesis, the operation at 50 kPa was successfully carried out and we can ensure the feasibility of low gas pressure operations with the development of the new amplifier. We can thus significantly reduce the gas pressure in future experiments. If the measurement is carried out at 10 kPa, the number of background events caused by the scattered neutron can be reduced to 1/10 that at 100 kPa. The largest uncertainty was due to the determination of the detection efficiency because our Monte Carlo simulations do not reproduce the deposit energy

well compared with the experimental data. However, we can solve this issue by improving the consistency of the simulations in the future. Of course, consistency between the simulations depends on the data statistics; our first step toward 0.1% accuracy for the neutron lifetime is improving the statistical uncertainty of our measurement. By measuring the neutron lifetime with 0.1% accuracy, we are aiming to finally verify the discrepancy between the proton counting method and the UCN storage method.

# Appendix A

# Developed amplifier

In this study, three new devices were developed. One of them is a low heat generation amplifier with GTARN ASIC. Another one is an additional amplifier which converts single ended signal to differential. It also can compensate the gain of the GTARN amplifier. The other is the module to divide and discriminate differential signal. This appendix explains the circuit of each device.

## A.1 Circuit of GTARN amplifier

GTARN amplifier is a kind of charge sensitive amplifier. GTARN ASIC has 8 equal channels, which consist of charge sensitive amplifier, pole-zero cancellation network, two low pass filter circuits, and analog buffer. Outside of GTARN ASIC, there are test pulse input, adjusters of operating voltage, and charge divide system to adjust input charge for avoiding the saturation of amplification. There is differentiating circuit on the line of test pulse input. Adjusting operating voltage is managed by using potentiometers. Charge dividing system is realized by using two capacitors and resistor. Circuit of GTARN amplifier is shown in Figure A.1. For our experiment, three GTARN amplifiers are mounted on a board. Therefore, a GTARN amplifier board has 24 channels. Board layout is shown in Figure A.2. Input signal comes from the twisted pair cable of the signal and the ground line, and the output signal is fed through the D-sub cable. The signal amplified by the ASIC is a single ended form. In addition to feeding the output signals, the D-sub cable also feeds the operating voltage of the amplifier, the ground line, and the test pulse for operation confirmation.

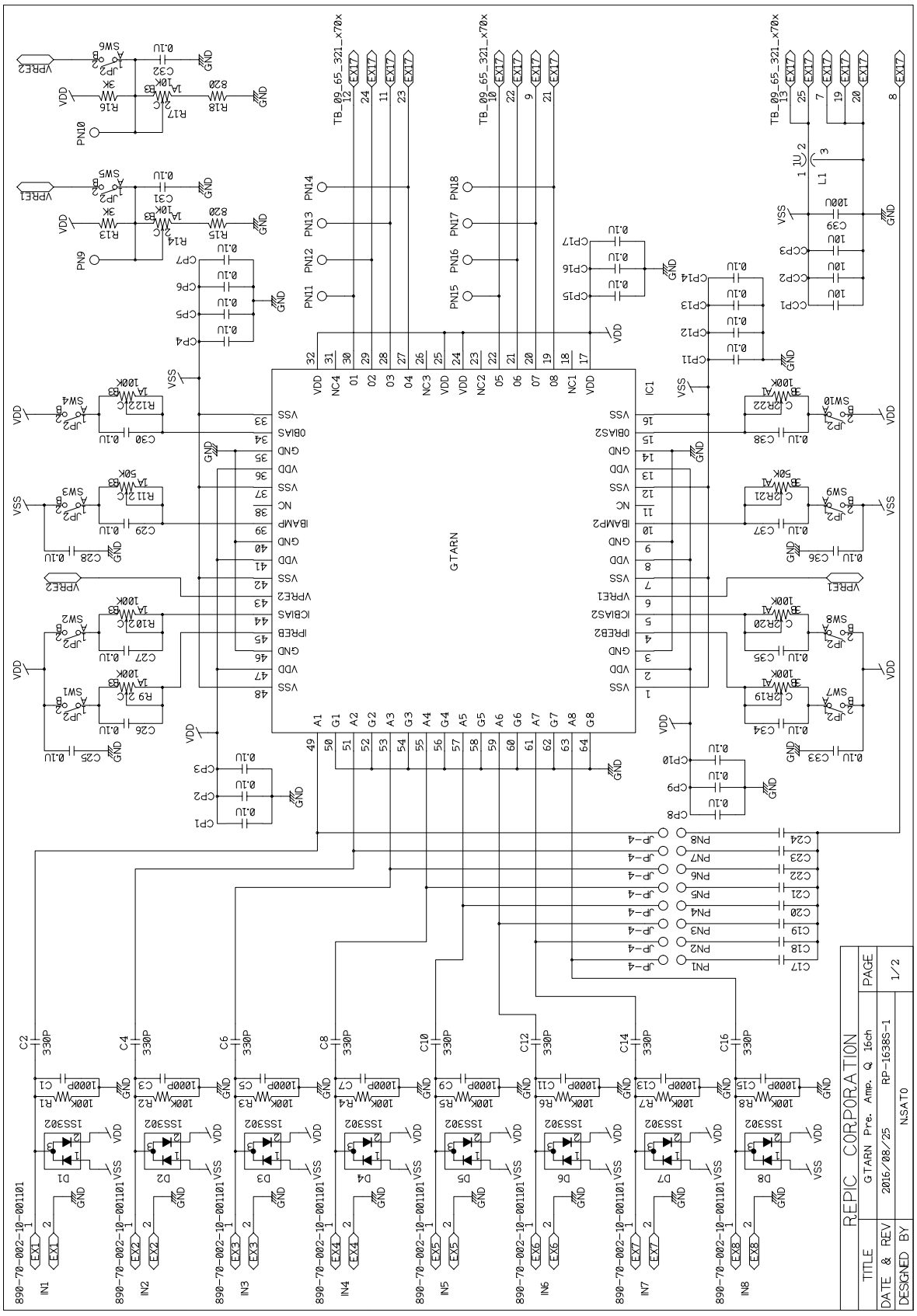


Figure A.1: Circuit of GTARN amplifier.

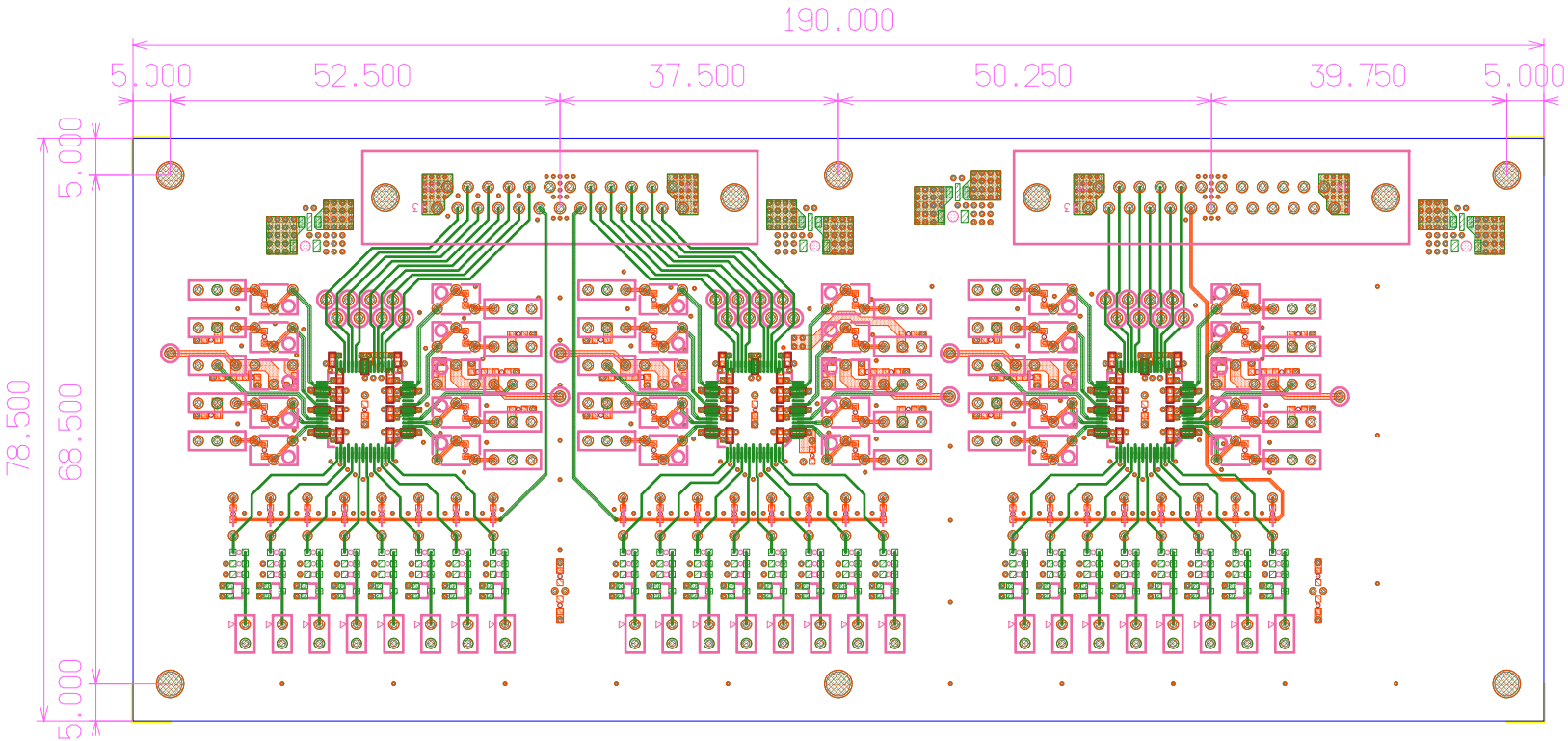


Figure A.2: Board layout with three GTARN amplifiers.

## A.2 Circuit of additional amplifier

Additional amplifier takes a role of converting single ended signal to differential, compensating the amplification, supplying power and test pulse for GTARN amplifier. There are 32 channels on a board. Board layout is shown in Figure A.3. Circuit of additional amplifier is shown in Figure A.4. Input signal comes from D-sub cable as a single ended form signal, and amplified through OP27 which is manufactured by ANALOG DEVICES. Single ended signal is converted to differential from by using AD8138 which also manufactured by ANALOG DEVICES. Differential signals are fed through the flat cable.

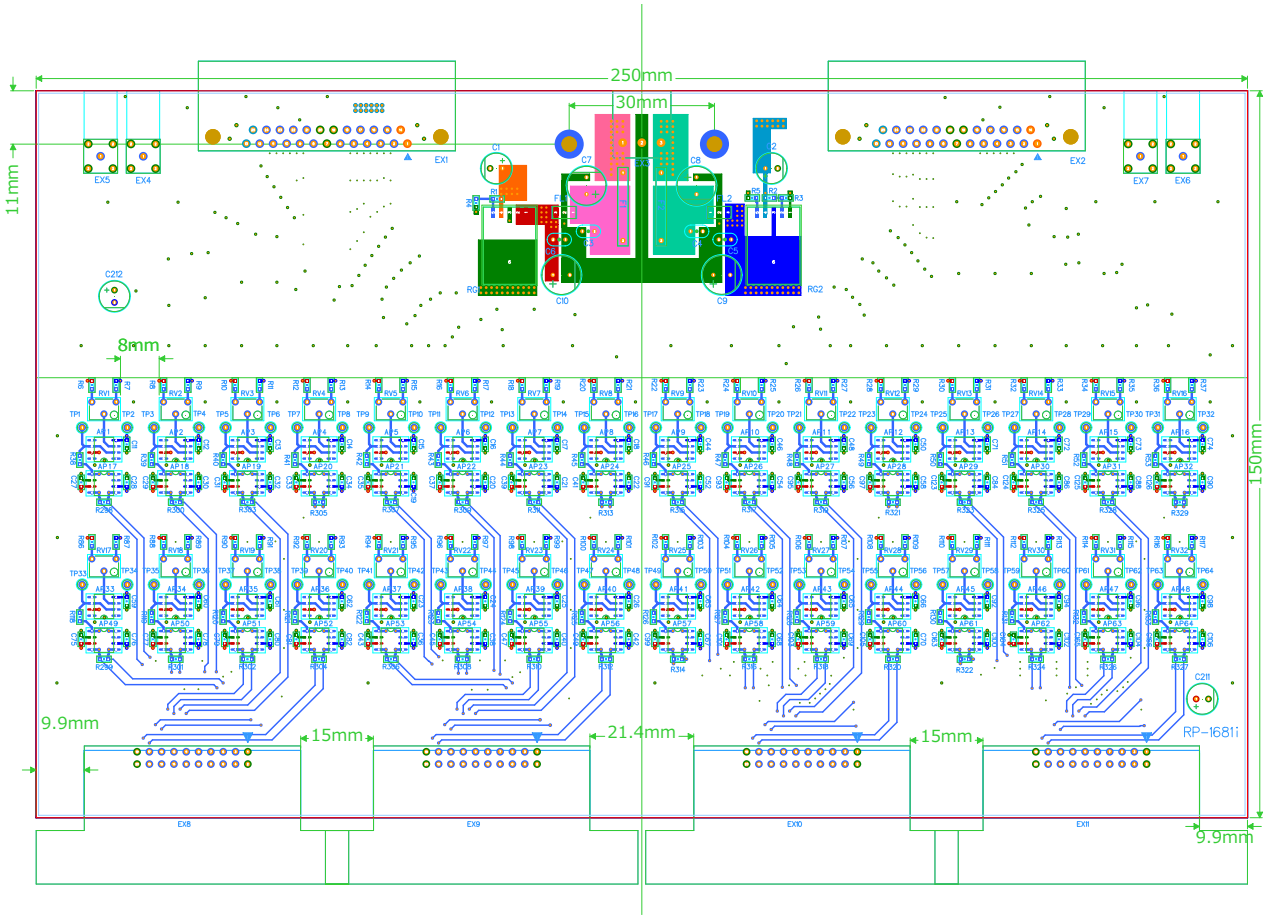


Figure A.3: Board layout of additional amplifier.

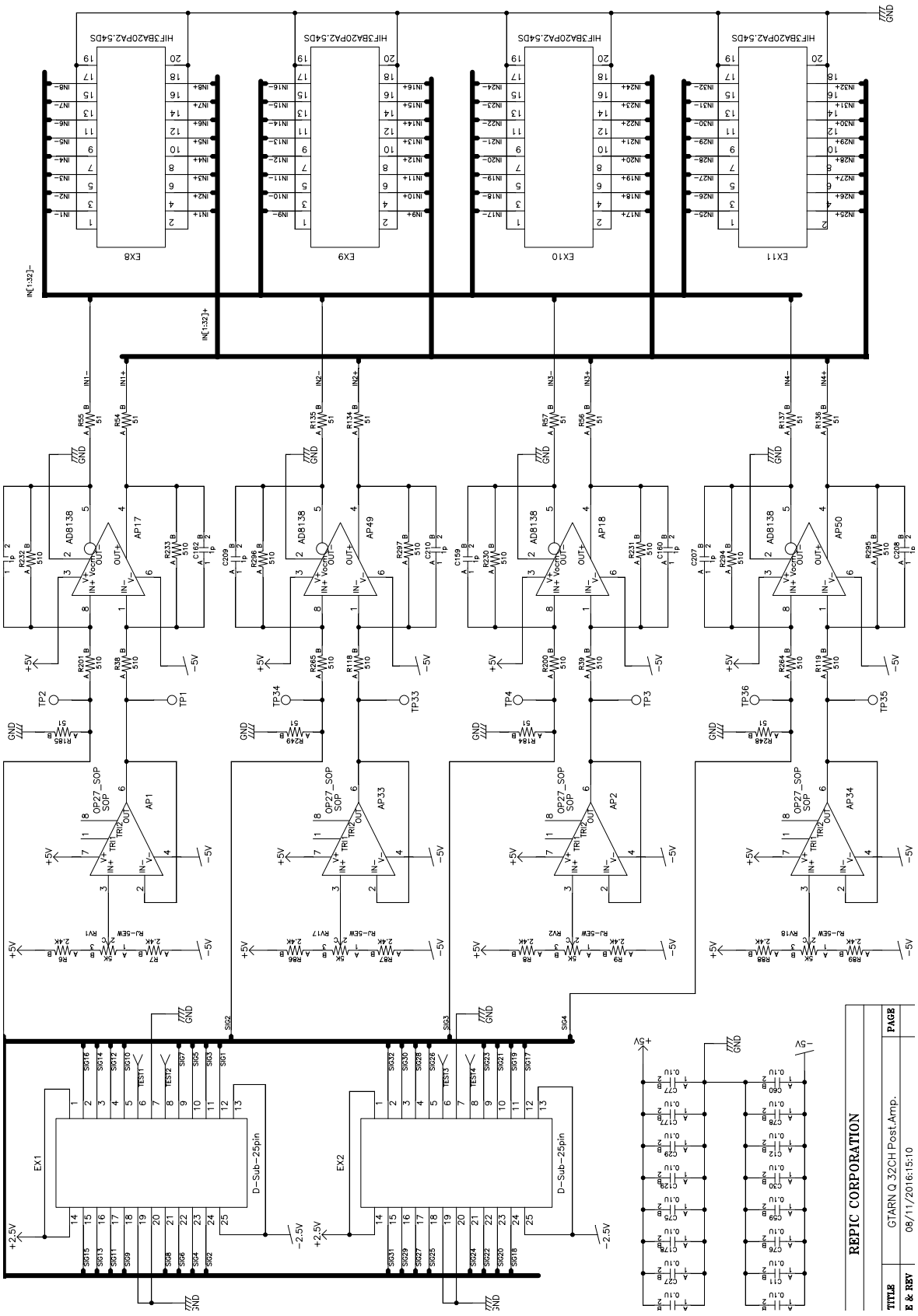


Figure A.4: Circuit of additional amplifier.

## A.3 Circuit of read out module

Developed read out module copes with differential signals from additional amplifier. This module has two outputs, one of them is a system that divides input differential signals into two outputs. The other is a system that makes trigger using an internal discriminator. Board layout of module is shown in Figure A.5 and circuit of module is shown in Figure A.6.

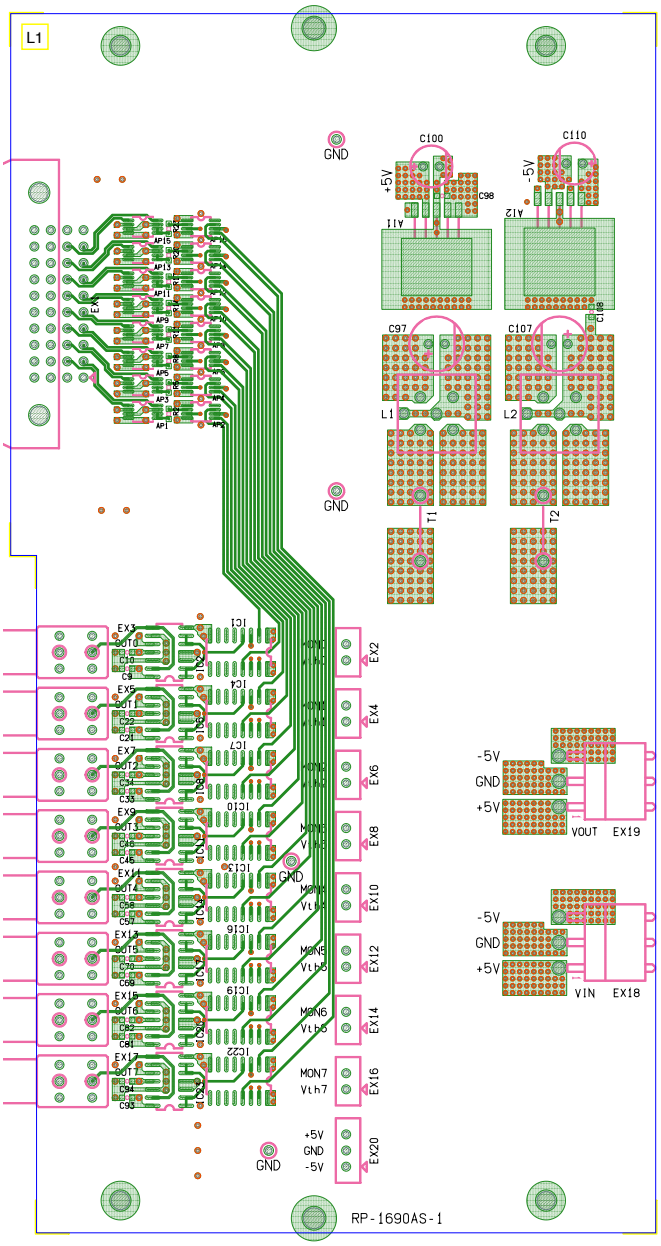


Figure A.5: Board layout of read out module.

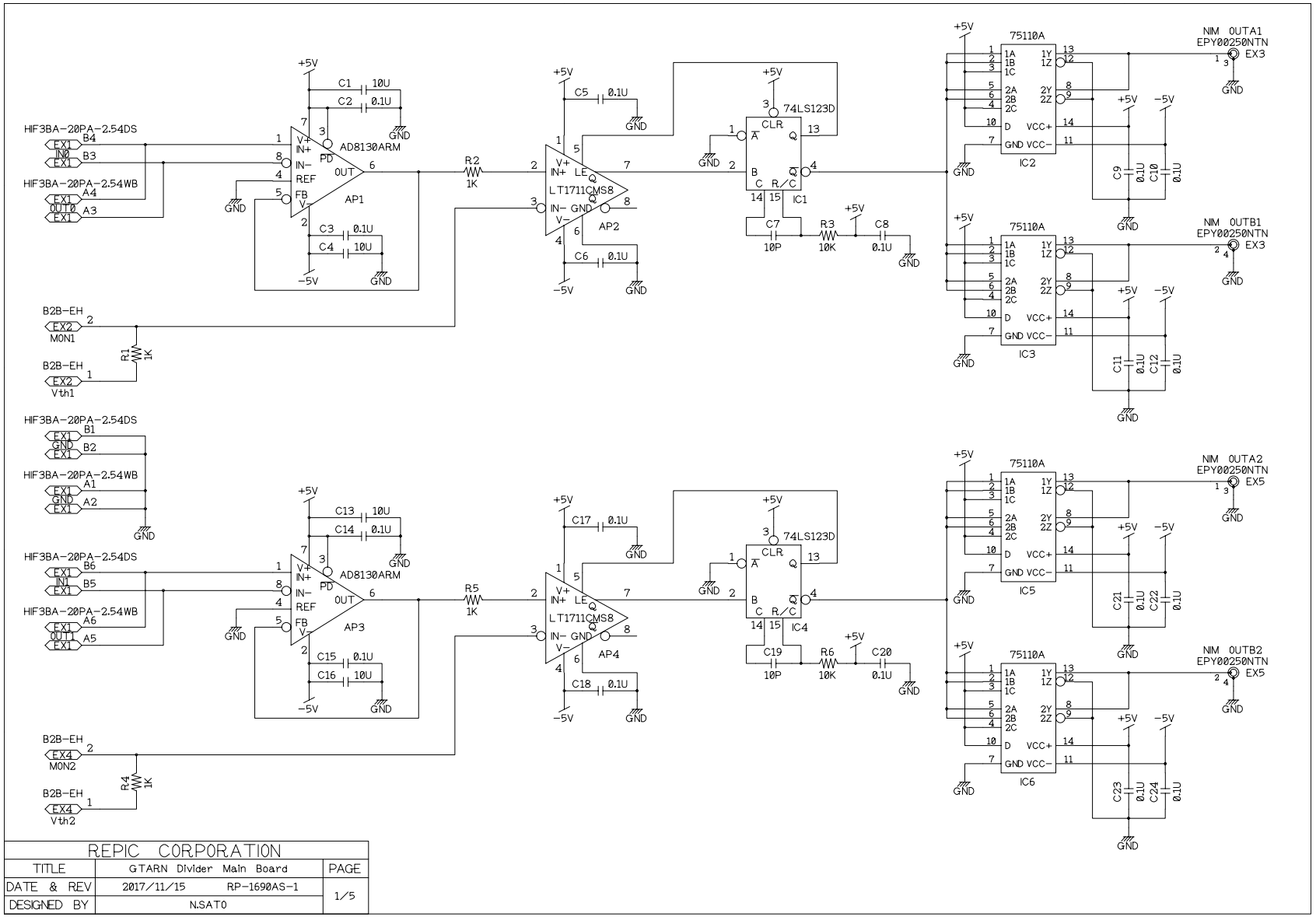


Figure A.6: Circuit of read out module.

# Acknowledgements

First of all, I am sincerely thankful to my supervisor, Dr. Kiyotomo Kawagoe, who always looked after me with kindness. I felt that I was able to grow greatly by being given the opportunities to go overseas to the experiment and international conference from the time of my master's degree. I also would like to deeply grateful to Dr. Tamaki Yoshioka. He gave me a lot of knowledge not only particle physics and taught me the pleasure of research. He has guided me to the world of researchers since I was entered to the laboratory of experimental particle physics. I occasionally said rude things and made him disappointed, however he accepted it with a generous heart and gave me adequate advice. I could not have written this doctor thesis without his support. I am really grateful to him for taking care of until completion of this thesis. I will continue to do my best in different field, so I hope to receive your support.

I would like to thank all the collaborators of this experiment. Especially, Dr. Kenji Mishima, who has worked together for neutron lifetime measurement, is one of the most contributed persons to carry out the measurement. He taught me how to carry out the measurement and it became a great support to me. I also sincere thank Dr. Masaaki Kitaguchi. He managed our collaboration and led us to the best way. I also would like to express my sincere gratitude to Dr. Hirohiko M. Shimizu, Dr. Katsuya Hirota, Dr. Yoshihisa Iwashita, Dr. Tatsusi Shima, Dr. Takashi Ino, Dr. Daiichiro Sekiba, Dr. Hirochika Sumino, Dr. Kaoru Taketani, Dr. Yoshichika Seki, Dr. Hidetoshi Otono and all those who have supported for NOP experiment.

I am grateful to Mr. Takahito Yamada and Mr. Ryunosuke Kitahara. Mr. Takahito taught me a lot of knowledge for computing and network operation. In addition his great skill of cooking was always satisfied collaborators' stomach. Mr. Ryunosuke gave me knowledges of gas, SFC and their analysis methods. Ms. Sei Ieki also taught me many ideas to carry out the measurement and analysis. Mr. Naoyuki Sumi, Mr. Naoki Nagakura, Ms. Aya Morishit, Mr. Jun Koga, Mr. Hideaki Uehara, who operated neutron lifetime measurement together, always gave me a lot of critical questions and constructive opinion. I would like to thank them for helping my study.

Not only collaborators, I would like to thank sincerely to my great colleagues Mr. Yuki Nakai, Mr. Genki Tanaka, Mr. Shohei Shirabe, and Mr. Shinji Koura. I also thank the member of laboratory of experimental particle physics including Mr. Hiraku Ueno, Mr. Kou Oishi, Mr. Satoru Matsumoto, Mr. Yohei Miyazaki, Mr. Shusuke Takada and Mr. Takumi Ito. I also thank to the staff of laboratory including Dr. Junji Tojo, Dr. Susumu Oda, Dr. Taikan Suehara. I also really thank all of those whose names are not written but supported my study and life. I would like to take this opportunity to appreciate the song of Nana Mizuki and her positive attitude. It is always a strong support of my mind.

Finally, I deeply grateful my parents. They gave me many encouragements throughout my life. They kindly accepted and helped me even when I decided to move on a different career path. There is nothing that makes me happy. I appreciate your kind of continued support.

# Bibliography


[1] E. Rutherford. Proceedings of the Royal Society of London Series A 97, 324 (1920).

[2] Bothe, Becker, Zeitschrift für Physik, 66, 289 (1930).

[3] I. Curie, F. Joliot, Comptes Rendus, 194, 273 (1932).

[4] J. Chadwick, Proc. Roy. Soc. A, 136, 692-708 (1932).

[5] Particle Data Group summary.

[6] K. A. Olive and Particle Data Group, Review of Particle Physics, Chinese Physics C 38, 090001 (2014).

[7] H. Abele, Nuclear Physics A 721, C182 (2003).

[8] M. Pospelov and J. Pradler, Annual Review of Nuclear and Particle Science 60, 539 (2010).

[9] C. Patrignani, P. D. Group, *et al.*, Chinese physics C 40, 100001 (2016).

[10] W. Mampe et al., JETP Lett., Vol. 57, No. 2, 82-87 (1993).

[11] J. Byrne et al., Europhysics Letters, Vol. 33, No. 3, (1996).

[12] A. Serebrov et al., Phys. Lett. B 605, 72 (2005).

[13] A. T. Yue et al., Phys. Rev. Lett. 111, 222501 (2013).

[14] A. Pichlmaier et al., Phys. Lett. B 693, 221 (2010).

[15] A. Steyerl et al., Phys. Rev. C 85, 065503 (2012).

[16] S. Arzumanov et al., Phys. Lett. B 745, 79-89 (2015).

[17] C. J. Christensen *et al.*, Phys. Rev. D 5, 1628 (1972).

[18] J. S. Nico *et al.*, Phys. Rev. C 71, 055502 (2005).

[19] A. T. Yue *et al.*, Physical Review Letters, 111, 222501 (2013).

[20] A. P. Serebrov *et al.*, Phys. Rev. C 78, 035505 (2008).

[21] R. W. Pattie *et al.*, Science Vol. 360, Issue 6389, pp. 627-632 (2018).

[22] R. Kossakowski *et al*, NIM A 284, 120 (1989).

[23] NIST, Neutron scattering lengths and cross sections.

[24] S. Agostinelli et al., Nucl. Instr. and Meth. A 506 250-303 (2003) .

[25] J-PARC official web site.

[26] Materials and Life science Facility official web site.

[27] Y. Arimoto *et al.*, Prog. Theor. Exp. Phys., (2012) 02B007

[28] T. Ino *et al.*, Physica B 406 (2011) 2424-2428

[29] K. Taketani et al., Proceedings of the International Workshop on Neutron Optics (2010).

[30] H. Otono, University of Tokyo, 2011, Ph.D. thesis.

[31] Yasojima Proceed Co., Ltd., Properties of PEEK.

[32] GNomes Design co.,ltd.

[33] Friedrich Paschen, Annalen der Physik. 273 (5) 69-75 (1889).

[34] Open-it official web site.

[35] GTARN explanation. http://openit.kek.jp/project/gtarn

[36] H. Yokoyama *et al.*, Nuclear Science Symposium and Medical Imaging Conference, IEEE, 1-2 (2013).

[37] H. Sumino, K. Nagao, and K. Notsuji. Journal of the Mass Spectrometry Society of Japan, Vol. 49, No. 2, pp.61-68 (2001).